Large-eddy Simulation of Physiological Pulsatile Flow Through A Constricted Channel

by

Afzal Hossain

A Thesis submitted to the Faculty of Graduate Studies of

The University of Manitoba

in partial fulfilment of the requirements of the degree of

MASTER OF SCIENCE

Department of Mechanical and Manufacturing Engineering

University of Manitoba

Winnipeg

Abstract

In this thesis, large-eddy simulation (LES) is used to simulate both Newtonian and non-Newtonian physiological pulsatile flows in constricted channels to gain insights into the physical phenomenon of laminar-turbulent flow transition due to the presence of an artificial arterial stenosis. The advanced dynamic nonlinear subgrid-scale stress (SGS) model of Wang and Bergstrom (DNM) [1] was utilized to conduct numerical simulations and its predictive performance was examined in comparison with that of the conventional dynamic model (DM) of Lilly [2].

An in-house LES code has been modified to conduct the unsteady numerical simulations, and the results obtained have been validated against available experimental and direct numerical simulation (DNS) results. The physical characteristics of the flow field have been thoroughly studied in terms of the resolved mean velocity, turbulence kinetic energy, viscous wall shear stress, and turbulence energy spectra along the central streamline of the domain.

Acknowledgements

I would like to express my great appreciation to my supervisor, Professor Bing-Chen Wang, for his support and insightful guidance in my research, and also for his generous help in the non-academic area which greatly encouraged me during my study in Canada. I would also like to express my appreciation to Dr. David C. S. Kuhn for his help in preparation of my technical papers. My sincere thanks also go to Professor M. F. Tachie and Professor S. J. Ormiston for their advice and help on my course studies. Specially, I would like to thank Dr. Mamun Molla for his support and help during my study.

I would also like to thank Abul Khair, Zhang Ye, QianQiu Xun, Mohammad Saeedi and Iman Fatemi for all the academic discussions and happy time working with them. I am grateful to all the friends I have made in Winnipeg for bringing me so many joyful moments and encouragement.

Finally, I would like to express my deep love and appreciation to my parents, wife, brother, sister-in-law, for their consistent and unconditional love and support.

Table of Contents

List of Figures

Nomenclature

English Symbols

A	Amplitude of the pulsatile oscillations
$\mathbf{A}$, A_{kj}	Cofactor matrix and tensor
C_S, C_W, C_N	SGS stress model coefficients
D	Computational domain
D_h	Hydraulic diameter
E	Energy spectrum
f, g	Arbitrary function
f_c	Parameter for controlling the height of the stenosis
f_s	Time frequency of eddy motions
G	Filter function
h, δ	Height of the channel (h is a constant and $\delta = \delta(x)$ is a variable)
i	Imaginary unit: $\sqrt{-1}$
$\mathbf{I}$	Identity matrix
$\mathbf{J}$	Jacobian of the cofactor matrix
k	Turbulence kinetic energy
k_c	Cut-off wave number
L_z	Width of the channel
$\mathcal{L}_{ij}$	Leonard type stress tensor
M	Total number of pulsatile cycle
m	Model constant
M_n	Coefficient

M_{ij}, W_{ij}, N_{ij}	Differential tensors
n, N	Number of the pulsatile cycles
N_x, N_y N_z	Number of control volumes along
	x, y and z axis, repectively
p	Pressure
P_r	SGS TKE production rate
Re	Reynolds number
S_r	Strouhal number
S_{ij}	Strain rate tensor
$\|\bar{S}\|$	Norm of $\bar{S}_{ij}$: $(2\bar{S}_{ij}\bar{S}_{ij})^{1/2}$
t	Time
T	Time period of a pulsatile cycle
u_i	Velocity components
u, v, w	Velocity components (corresponding
	to u_1, u_2, u_3, respectively)
$\bar{U}$	Bulk velocity
x, y, z	Coordinates of a Cartesian frame

Greek Symbols

α	Womersley number
α_{ij}, λ_{ij}, ζ_{ij}	Test-grid level base tensors
β_{ij}, γ_{ij}, η_{ij}	Grid level base tensors
δ_{ij}	Kronecker delta
$\bar{\Delta}$	Grid level filter width
ΔS	Control surface
ΔV	Control volume
$\tilde{\bar{\Delta}}$	Test-grid level filter width

ϕ_n	Phase angle
μ	Molecular dynamic viscosity of the fluid
μ_e	Effective dynamic viscosity of the fluid
μ_{sgs}	SGS dynamic eddy viscosity of the fluid
ν	Molecular kinematic viscosity of the fluid
ν_{sgs}	SGS kinematic eddy viscosity
ω	Frequency: $2\pi/T$
Ω_{ij}	Rotation rate tensor
ρ	Fluid density
τ_w	Wall shear stress
σ	Pressure smoothing term
τ_{ij}	SGS stress tensor
ξ_k	Curvilinear coordinates

Subscripts and Superscripts

$\bar{(\,)}$	A grid level filtered quantity
$\tilde{(\,)}$	A test-grid level filtered quantity
$(\,)^+$	Forward scatter
$(\,)^-$	Backward scatter
$(\,)_{reatt}$	Point of reattachment
$(\,)_{sep}$	Point of separation
$\langle\,\rangle_p$	Phase averaged quantities
$\langle\,\rangle_s$	Spanwise averaged quantities
$\langle\,\rangle$	Time- and spanwise-averaged quantity

Abbreviations

2D	2-Dimensional
3D	3-Dimensional
CV	Control Volume
DM	Dynamic Smagorinsky Model
DNM	Dynamic Nonlinear SGS Stress Model
DNS	Direct Numerical Simulation
FFT	Fast Fourier Transform
LDV	Laser Doppler Velocimetry
LES	Large-Eddy Simulation
RANS	Reynolds-Averaged Navier-Stokes
RMS	Root-Mean-Square
SGS	Subgrid-Scale
SM	Smagorinsky Model
TKE	Turbulence Kinetic Energy
WSS	Wall Shear Stress

Chapter 1

Introduction

1.1 Background and Motivation

Human blood flow through arteries is inherently unsteady and pulsatile due to the cyclic nature of the heart pump, and the flow pattern can be laminar, turbulent or transitional depending upon the location and geometry of the blood vessels. The transition of the flow pattern in a blood vessel is often induced by sudden expansion (aneurysm) and sudden contraction (stenosis) of the cross-sectional area of a vessel, however, this physical mechanism is further complicated by unsteady pulsations, unsteadiness, recirculation and curvilinear effects. Moreover, owing to the presence of a moderate or severe stenosis in the artery, the flow can transit from laminar to turbulent patterns. Therefore, it is very important to understand the fundamental physics of these types of pulsatile stenotic transition flows, as they are essential for further understanding of the physiology of arterial diseases.

1.1.1 Flow Through A Stenotic Channel

Investigation of fluid flow through stenosed (constricted) geometry represents an interesting and challenging topic for its significance in biomechanics from theoretical, experimental and clinical point of view. Generally blood flow in arteries is unsteady and pulsatile due to the cyclic nature of the heart pump. The Reynolds number (based on the channel height and bulk velocity) of blood flow can vary from 1 to 4000 in

different types of human arteries [5]. Although blood flow is mostly pulsatile laminar without any obstruction in an artery, it can undergo laminar-turbulent transition in presence of a constriction. Furthermore, flow pulsatility also plays an important role on transition to turbulence in arteries [5]. As a result, due to the presence of a stenosis and flow pulsatility, turbulence can generate even at a Reynolds number (based on the hydraulic diameter and bulk velocity) as low as a few hundred [6]. This behaviour is in sharp contrast to that of the well-known pipe flows, for which the critical Reynolds number for transition is approximately 2300.

1.1.2 Experimental Studies

In literature, extensive experimental studies have been reported which provide insights into the physical mechanism underlying transition-to-turbulent flows through arterial stenoses. Most of the experimental studies of blood flows through stenosis models have focused on the effects of blood vessel geometries and shear stresses on the inner arterial wall. Clark [7,8] studied the fluid mechanics of a nozzle shaped stenosis based on both pulsatile (or, unsteady in some literature) and non-pulsatile (or, steady) flows using the laser Doppler velocimetry (LDV) technique. He reported the statistics of a highly disturbed flow after the stenosis and the influence of the Reynolds number on the velocity fluctuations. In their study, Cassanova and Giddens [9] focused on the flow disturbances as a result of the stenoses and pulsations. The Reynolds number in Cassanova and Giddens [9] ranged from 318 to 2540. They concluded that the more abrupt and sharp-edged the stenosis, the greater the flow disturbance at a given Reynolds number. For the non-pulsatile flow case, their visualization studies and measurements indicated that if the stenosis is smoothly contoured, a serious degree of stenosis with 50% contraction in the cross-sectional area of the tube is required to cause substantial flow disturbances at the Reynolds number studied. However, for their pulsatile flow case, the flow disturbances are generated with a mild stenosis of 25% contraction. Based on these observations, Cassanova and Giddens [9] concluded that the flow transition in the post-stenotic region is strongly dependent upon the

flow pulsatility.

Young and Tsai [10] investigated steady flow through axisymmetric and non-symmetric plastic model of arterial stenoses for Reynolds numbers ranging from 100 to 5000. Their experimental results show strong influence of the size and shape of stenosis on flow characteristics such as pressure losses, separation, turbulence phenomena and critical Reynolds number etc. Young and Tsai [11] also investigated oscillating flow using the similar axisymmetric and nonsymmetric stenosis model. They reported that the oscillating flow is more stable than the corresponding steady flow for mild constrictions, whereas flow is slightly less stable for constricted models. Youngchareon and Young [12] also studied both steady and pulsatile flows through three severely constricted stenosis models. They reported that the critical Reynolds number for transition-to-turbulence in a pulsatile flow through the stenosis not only depends on the shape and size of the stenosis but also on the characteristics of the inlet-flow waveform (of the pulsation), which is a similar result to that of Young and Tsai [10, 11].

Ahmed and Giddens [3, 13] studied flow disturbances through an axisymmetric stenosis with a maximum of 75% area reduction at the moderate Reynolds number ranging from 500 to 2000 using the LDV technique. They reported detailed measurement results on both the velocity and velocity fluctuations in the post-stenotic region. Later on, Ahmed and Giddens [14] studied pulsatile post-stenotic flows through the same geometry using the same methodology with a sinusoidal centerline velocity profile at Reynolds number of 600. Ahmed [15] again conducted experiments on pulsatile flow through a similar type of smooth arterial stenosis at Reynolds number ranging from 200 to 1000 using LDV and studied propagation of post-stenotic flow disturbances.

1.1.3 Computational Studies

Beyond the leading experimental investigations mentioned above, the method of computational fluid dynamics (CFD) has been significantly developed to simulate

these types of pulsatile stenotic transition flows over the past decade. Major CFD studies on laminar-turbulent transition flow in idealized stenoses include the Reynolds-averaged Navier-Stokes (RANS) method, direct numerical simulation (DNS) and large-eddy simulation (LES).

Tan *et al.* [16], Ghalichi *et al.* [17] and Lee *et al.* [18, 19] studied 2-dimensional (2D) laminar-turbulent transitional flows in an arterial stenosis using RANS models (particularly, the $k-\epsilon$ model). Ryval *et al.* [20] also examined both steady and sinusoidally pulsatile flows through 75 and 90 percent constricted channel at Reynolds numbers 500 and 1000 using both standard and transitional versions of the $k-\epsilon$ models. They concluded that the transitional $k-\epsilon$ model gives a better agreement with the experimental result of Ahmed and Giddens [3, 13, 14], whereas the standard $k-\epsilon$ model gives a better prediction of the variation of the recirculation zone length with the Reynolds number. Paul *et al.* [21] investigated the effects of the spiral blood flow in a model of 3D arterial stenosis with a 75 percent cross-sectional area reduction at the centre using the standard $k-\epsilon$ model for Reynolds numbers 500 and 1000. They concluded that the spiral effect reduces the turbulence kinetic energy (TKE) and produces oscillating wall shear stress in the post-stenotic region which may damage the inner side of the blood vessel. They simplified the work by assuming that the walls of the vessel are rigid.

Saffman and Wilcox [22] indicated that the RANS approach often fails to show good results for the Reynolds shear stress, turbulence kinetic energy and dissipation rate. Later on, Wilcox [23] mentioned that RANS turbulence models are primarily designed for simulating well-developed, high Reynolds number turbulent flows and are not suitable for predicting arterial flows. Scotti and Piomelli [24] later clarified that there are inherent limitations with the conventional RANS turbulence models when they are applied to the study of pulsatile flows (which are intrinsically unsteady). The RANS modelling approach does not represent an ideal tool for simulating the pulsatile transitional flows, as the governing equations in a RANS approach is ensemble-averaged.

With the advancement of the computational power, several DNS studies on post-stenotic laminar-turbulent transition flows have been conducted. Sherwin and Blackburn [25, 26] studied transition to turbulence of steady and pulsatile axisymmetric stenotic pipe flows using DNS technique. For the pulsatile case, they took a simple sinusoidal profile at the inlet with Reynolds number ranging from 250 to 800. Varghese *et al.* [27, 28] investigated both non-pulsatile and pulsatile flows through a modeled axisymmetrical stenosis using the DNS approach and reported detailed turbulence statistics at low Reynolds numbers in the downstream region of the stenosis. Later on, they extended their study by comparing the DNS results with the corresponding LES and RANS simulation and concluded that LES is a more promising method for modelling transitional stenotic flows [29]. Recently, Bhaganagar [30] performed high-order DNS for four canonical types with identical degree (25%) of stenosis of modelled blocked vessels. Their analysis indicates that turbulence statistics are dependent not only on morphology but also the shape of the stenosis.

From the point of view of numerical simulation, DNS is extremely demanding on computing resources as all the spatial and temporal scales of turbulence need to be accurately resolved (including the smallest turbulent eddy motions at the Kolmogorov scales). On the other hand, the RANS approach only resolves the turbulent eddy motions at the largest integral scales, and are not suitable for unsteady simulation of pulsatile flows in a stenotic channel. Owing to the limitations of the RANS and the DNS approaches mentioned above, the method of LES embodies a superior numerical tool for this type of research. In LES, a filter is used to differentiate large (filtered) and small (subgrid) scales of motion. Unlike the DNS approach, only the filtered scales are resolved while the smaller or subgrid-scales (SGS) are modeled in a LES approach. As a consequence, the computational expenses associated with a LES approach can be significantly reduced. Moreover, LES is capable of providing time-accurate information about a wide range of dynamically important scales with a better physical insights into the flow.

The application of the technique of LES to the study of flow in a modeled arterial

stenosis has been reported by several researchers. Mittal *et al.* [4,31] studied pulsatile transition flows in a planar channel with a semi-circular constriction using LES. The maximum Reynolds number (based on width of the channel and bulk velocity) in their studies was 2000. Paul *et al.* [32] used LES to study pulsatile blood flows through a simple 3D channel with a biological type stenosis formed on the top wall. They investigated the laminar-turbulent transition phenomena of a non-additive pulsatile flow at a fixed Reynolds number of 1200 using the dynamic subgrid model of Piomelli and Liu [33]. Molla *et al.* [34,35] investigated with the same type of model stenosis for both additive and non-additive pulsatile flows for a maximum Reynolds number of 2000 using the dynamic model of Lilly (DM) [2].

Barber and Simmons [36] conducted LES of an incompressible homogeneous Newtonian flow using a commercial code, FLUENT 6.3, for a rigid, symmetric artery with fifty percent vessel constriction. They imposed a physiological pulsatile profile at the inlet of the model stenosis and the SGS stresses were modeled using the DM of Lilly [2]. Gardhagen *et al.* [37] performed LES for flow in a 75 percent stenosed (based on cross sectional area) pipe with a fully-developed Poiseuille flow prescribed at the inlet. They used ANSYS GAMBIT 204 for mesh generation and FLUENT for computing the wall shear stress (WSS). They divided the post-stenotic region into three parts based on WSS characteristics along with the decomposition of the WSS into a time-averaged and a fluctuating components. Very recently, Tan *et al.* [38] used both LES and RANS to predict transitional flow in 75 percent stenosed arterial vessels caused by symmetrical and slightly eccentric stenoses. They reported that the LES model shows a better agreement with the experimental data than the RANS model, though RANS is also capable of capturing important flow features such as flow separation and reattachment.

1.2 Subgrid-scale Models in LES

LES is an approach that can be considered to lie between DNS and RANS. Unlike DNS, where all spatial and temporal scales are resolved; in LES, only the energy-containing scales (corresponding to 'large eddies') of the turbulence are resolved spatially and temporally; the smaller scales (or, subgrid scales (SGS)), need to be modeled [39].

The first SGS stress model is the so-called Smagorinsky model (SM), originally introduced by Smagorinsky in 1963 [40]. This model correlates the SGS stress tensor τ_{ij} with the resolved strain rate tensor, $\bar{S}_{ij}$ (defined as $\bar{S}_{ij} \stackrel{\text{def}}{=} \frac{1}{2}\left(\frac{\partial \bar{u}_i}{\partial x_j} + \frac{\partial \bar{u}_j}{\partial x_i}\right)$) through a model coefficient (which is referred to as the Smagorinsky model coefficient). A groundbreaking advancement in SGS stress modelling was the introduction of the dynamic model (DM) in 1991 by Germano *et al.* [41]. In comparison with the original SM, the DM is free from any empirical pre-determined model constants. Both the model coefficient and the near-wall SGS length-scale can be dynamically calibrated using the updated flow field in the DM SGS modelling approach.

Following the introduction of the DM by Germano *et al.* [41] and Lilly [2] in the early 1990's, a further advancement in SGS modelling is represented by the dynamic nonlinear model (DNM) of Wang and Bergstrom [1], which includes the DM of Germano *et al.* [41] as the first-order approximation. In comparison with the DM, the DNM proposed by Wang and Bergstrom [1] admits more degrees of freedom for nonlinear representation of the SGS stress tensor.

The conventional DM of Germano *et al.* [41] and Lilly [2] is still the most popular in literature for LES of turbulent flows. It is well-known for its advantages such as self-calibration, numerical robustness, and being free from any empirical constants and need for any *ad hoc* wall damping functions near the solid surface. However, the Smagorinsky constitutive relation [40] for the DM is based on the classical linear Boussinesq hypothesis which assumes the principal axes of the negative SGS stress tensor to be exactly aligned with those of the resolved strain rate tensor.

This inevitably leads to an inadequate geometrical representation of the SGS stress components [1,42]. On one hand, if the model coefficient is restricted to be positive, it can lead to an unrealistic SGS dissipation effect. On the other hand, if the coefficient is allowed to be negative, numerical instability arises due to excessive backscatter of the SGS kinetic energy (KE). In comparison with the DM, the DNM exhibits significant flexibility in self-calibration of the model coefficients and avoid excessive backscatter of SGS KE and potential modelling singularity problems. The DNM also admits various tensorial representation of the SGS stress tensor and reflects both forward and backward inertial inviscid KE scattering process between the resolved and unresolved scales of motions. In contrast with the DM, the DNM is a localization model, which exhibits instantaneous local stability without restoring to any plane averaging technique or any arbitrary bounds for restricting the model coefficients.

1.3 LES of Non-Newtonian Flows in A Stenotic Channel

In the current literature on LES of stenotic flows, simulations have been performed based on primarily the dynamic SGS stress model (DM) of Germano *et al.* [41] and Lilly [2]. It should be pointed out that this type of numerical approach, i.e. LES of non-Newtonian blood flows based on the conventional DM, is conceptually inconsistent. This is because the constitutive relationship of the DM is based on the overly simplified linear Boussinesq assumption (Smagorinsky), and correspondingly, the SGS viscosity of the DM is a linear function of the resolved strain rate tensor. In contrast, it is widely observed that the molecular viscosity of a non-Newtonian fluid is typically a nonlinear function of the strain rate tensor.

In order to ensure both the molecular and SGS viscosities are conceptually consistent in LES of a non-Newtonian flow, the advanced dynamic nonlinear SGS stress model (DNM) of Wang and Bergstrom [1] is implemented in the numerical procedure. For this proposed consistent modelling approach, the Cross model [43] is

used to evaluate the non-Newtonian molecular viscosity at the filtered (or, resolved) scale and the DNM is used to reflect the non-Newtonian characteristics of the SGS viscosity at the SGS (or, unresolved) scale.

1.4 Objective of the Thesis

This research includes three major objectives:

- The physics of pulsatile Newtonian flow confined within a 3D channel with both-sided constriction will be studied. This analysis includes the resolved mean velocity, turbulence kinetic energy, mean pressure, viscous wall shear stress, resolved and subgrid-scale turbulent shear stresses, model coefficients, SGS TKE production rate, and turbulence energy spectra. This research further aims at examining the predictive performance of the DNM in comparison with the conventional DM.

- A new consistent modelling approach is proposed to resolve the current conceptual inconsistency in modelling the molecular and SGS viscosities for LES of non-Newtonian flows. In this study, as the first attempt to resolve the current inconsistence in shear stress modelling for LES, the attention will be focused on the combination of the Cross model and the DNM of Wang and Bergstorm [1].

- This research also aims at validating the current LES result with the experiment results of Ahmed and Giddens [3], the LES results of Mittal *et al.* [4] and the DNS results of our research group (by courtesy of Md. Abul Khair) in order to examine the predictive accuracy of the numerical algorithm.

1.5 Outline of the Thesis

The thesis is organized as follows. In chapter 2, the methodology of LES will be introduced, including, e.g., the filtering operation and filtered governing equations for LES, the algorithm along with the boundary conditions for solving the filtered governing equations, and SGS stress models to be used for closure of the filtered momentum equation.

In chapter 3, the LES technique will be applied to investigate the physics of pulsatile Newtonian flows through a both-sided constricted channel. The numerical results obtained from the LES will be thoroughly validated against experimental measurements and the available numerical data. Furthermore, the effect of the Reynolds number on flow characteristics will be analyzed by varying the Reynolds number from 750 to 1800.

In chapter 4, the LES technique associated with the DNM will be applied to simulation of physiological pulsatile non-Newtonian flows through a one-sided cosine-shaped constricted channel. The predictive performance of the DNM will be thoroughly analyzed. The Reynolds number tested for this case is set to 1200.

In chapter 5, a summary of the major conclusions of this thesis and a discussion of the directions for possible future explorations will be presented.

Chapter 2

Numerical Methods

2.1 Governing Equations

Human blood flow can be treated as a Newtonian fluid in large arteries, however, in smaller arteries and veins, it behaves typically as a non-Newtonian incompressible viscoelastic fluid [44]. For both Newtonian and non-Newtonian flows, the Navier-Stokes equations are suitable for predicting the flow physics of blood through the arterial stenosis. We assume that the fluid is homogeneous and incompressible. The continuity and momentum equations for a homogeneous incompressible flow take the following forms in the general Cartesian curvilinear coordinate system

$$\frac{A_{kj}}{|\mathbf{J}|}\frac{\partial u_j}{\partial \xi_k} = 0 \tag{2.1}$$

$$\frac{\partial u_i}{\partial t} + \frac{A_{kj}}{|\mathbf{J}|}\frac{\partial u_i u_j}{\partial \xi_k} = -\frac{A_{kj}}{\rho|\mathbf{J}|}\frac{\partial p}{\partial \xi_k} + \frac{\mu}{\rho}\frac{A_{kj}A_{lj}}{|\mathbf{J}|^2}\frac{\partial^2 u_i}{\partial \xi_k \partial \xi_l} \tag{2.2}$$

In the above equations, A_{kj} are the elements of the cofactor matrix, $\mathbf{A}$, of the Jacobian $|\mathbf{J}|$.

2.2 The Filtering Operation

To obtain the LES equations, the governing Eqs. 2.1-2.2 are filtered using a low-pass spatial filter which separates the large scale (resolved scale) from the small scale (subgrid scale). If $f(x_j, t)$ represent a generic instantaneous variable at at location x_j and time t, the corresponding filtered variable, known as the resolvable $\bar{f}(x_j, t)$, is defined as the convolution of $f(x_j, t)$ [45]:

$$\bar{f}(x_j, t) = \int_D f(x'_j, t) G(x_j - x'_j, \Delta(x_j)) dx'_j \tag{2.3}$$

where G is a filter kernel function, D is the computational domain; $\Delta(x_j)$ is the filter width, which in LES practice is typically defined based on the 3D mesh sizes as $\Delta(x_j) = \sqrt[3]{\Delta x \Delta y \Delta z}$. The filter function G is usually defined as the product of three one-dimensional filters,

$$G(x_j - x'_j, \Delta(x_j)) = \prod_{j=1}^{3} g(x_j - x'_j, \Delta(x_j)) \tag{2.4}$$

where g is an arbitrary function, the filter function G must satisfy the normalisation condition,

$$\int_D G(x_j - x'_j, \Delta(x_j)) dx'_j = 1 \tag{2.5}$$

Defining the Fourier transform $\hat{f}(k_j, t)$ of $f(x_j, t)$ as

$$\hat{f}(k_j, t) = \int_D f(x'_j, t) e^{-ik_j x_j} dx_j \tag{2.6}$$

It can be seen from the definition of the spatial filter (Eq. 2.3) that $\bar{f}(x_j, t)$ is a simple convolution of the generic variable $f(x'_j, t)$ and filter function G, which implies that its Fourier transform is

$$\hat{\bar{f}}(k_j, t) = \hat{G} \hat{f}(k_j, t) \tag{2.7}$$

where $\hat{G} = \prod_{j=1}^{3} \hat{g}(k_j, \Delta(x_j))$ is the Fourier transform of the filter function. It is important to note that this filter function determines the size and structure of the smallest resolvable eddies. Various distributions of the filter function are available in

the literature, for example, see Leonard [45], Germano [41], and Ghosal and Moin [46]. The most commonly used filter functions and their Fourier transforms are given below. The top hat filter,

$$G(x_j - x'_j, \Delta(x_j)) = \begin{cases} \frac{1}{\Delta(x_j)} & \text{if} \quad \left|x_j - x'_j\right| \leq \frac{\Delta(x_j)}{2} \\ 0 & \text{otherwise} \end{cases} \tag{2.8}$$

and the Fourier transform of the top hat filter is

$$\hat{g}\left(k_j, \Delta(x_j)\right) = \frac{sin\left(k_j \frac{\Delta(x_j)}{2}\right)}{k_j \frac{\Delta(x_j)}{2}} \tag{2.9}$$

The Gaussian filter,

$$G(x_j - x'_j, \Delta(x_j)) = \left(\sqrt{\frac{6}{\pi}} \frac{1}{\Delta(x_j)^2}\right) exp\left[-\frac{6(x_j - x'_j)^2}{\Delta(x_j)}\right] \tag{2.10}$$

and its Fourier transform is

$$\hat{g}(k_j, \Delta(x_j)) = exp\frac{-(k_j \Delta(x_j))}{24} \tag{2.11}$$

and the Fourier cut-off filter,

$$G\left(x_j - x'_j, \Delta(x_j)\right) = \frac{sin(k_c(x_j - x'_j))}{\pi(x_j - x'_j)} \tag{2.12}$$

where $k_c = \frac{\pi}{\Delta(x_j)}$ and the corresponding Fourier transform is

$$\hat{g}(k_j, \Delta(x_j)) = \begin{cases} 1 & \text{if} \quad |k| \leq k_c \\ 0 & \text{otherwise} \end{cases} \tag{2.13}$$

From its definition equation, it is clear that for the Fourier cut-off filter, if $\hat{g}$ is zero for $k^2 = k_j k_j > k_c^2$ (where k_c is a cut-off wave number defining the limit of wave resolution) then $\bar{f}$ will contain no contribution from wave numbers greater than k_c. This implies that, wave numbers greater than a cut-off value are completely removed from the flow field leaving the smallest wave numbers unaffected. In contrast, both

the top hat and Gaussian filter functions affect all wave numbers without removing completely any particular part of the spectrum. In the simulation, the top hat filter given in Eq. 2.8 is used following the suggestion of Germano [41] who indicated that the top hat filter fits naturally into a finite volume formulation. It should be further indicated that for the current LES approach, the filtering process is applied to the dynamic procedure at the test-grid level only.

2.3 Filtered Governing Equations

After applying the filtering process to the governing Eqs. 2.1 and 2.2, the filtered continuity and momentum equations for LES of a homogeneous incompressible flow take the following forms in the general Cartesian curvilinear coordinate system

$$\frac{A_{kj}}{|\mathbf{J}|}\frac{\partial \bar{u}_j}{\partial \xi_k} = 0 \tag{2.14}$$

$$\frac{\partial \bar{u}_i}{\partial t} + \frac{A_{kj}}{|\mathbf{J}|}\frac{\partial \bar{u}_i \bar{u}_j}{\partial \xi_k} = -\frac{A_{kj}}{\rho|\mathbf{J}|}\frac{\partial \bar{p}}{\partial \xi_k} - \frac{A_{kj}}{|\mathbf{J}|}\frac{\partial \tau_{ij}}{\partial \xi_k} + \frac{\partial}{\partial \xi_k}\left[\frac{A_{kj}}{\rho|\mathbf{J}|}\mu\left(\frac{A_{lj}}{|\mathbf{J}|}\frac{\partial \bar{u}_i}{\partial \xi_l} + \frac{A_{li}}{|\mathbf{J}|}\frac{\partial \bar{u}_j}{\partial \xi_l}\right)\right] \tag{2.15}$$

As a direct consequence of the filtering process, the SGS stress term, $\tau_{ij} \stackrel{\text{def}}{=} \overline{u_i u_j} - \bar{u}_i \bar{u}_j$, appears in the filtered momentum equation, which needs to be modeled in order to close the above set of governing equations.

2.4 SGS Stress Models

Two SGS stress models are used for the closure of the filtered momentum equations in this thesis: namely, the conventional dynamic Smagorinsky model (DM) of Lilly [2] and the advanced dynamic nonlinear SGS stress model (DNM) of Wang and Bergstrom [1]. The formulations for these two dynamic linear and nonlinear models are briefly described as follows.

2.4.1 Dynamic Smagorinsky Model (DM)

The conventional DM introduced by Lilly [2] has been widely used in the LES community due to its simplicity and robustness. The constitutive relation for the DM is based on a linear tensorial function of the resolved strain rate tensor $\bar{S}_{ij}$, i.e.

$$\tau^*_{ij} = -2C_S\bar{\Delta}^2|\bar{S}|\bar{S}_{ij} \tag{2.16}$$

where $\bar{\Delta} \stackrel{\text{def}}{=} (\Delta x\Delta y\Delta z)^{1/3}$ is the grid level filter size, $\bar{S}_{ij} \stackrel{\text{def}}{=} \frac{1}{2}\big(\frac{\partial \bar{u}_i}{\partial x_j} + \frac{\partial \bar{u}_j}{\partial x_i}\big)$ is the resolved strain rate tensor and $|\bar{S}| \stackrel{\text{def}}{=} (2\bar{S}_{ij}\bar{S}_{ij})^{1/2}$ is the norm of $\bar{S}_{ij}$. In the above equation, an asterisk represents a trace-free tensor, i.e. $(\cdot)^*_{ij} \stackrel{\text{def}}{=} (\cdot)_{ij} - (\cdot)_{kk}\delta_{ij}/3$ and δ_{ij} is the Kronecker delta. In the DM, the model coefficient C_S is computed dynamically during the simulation, rather than input *a priori* as in the Smagorinsky SGS stress model.

The optimal dynamic coefficient C_S can be obtained using the least squares method to give

$$C_S = -\frac{M_{ij}\mathscr{L}^*_{ij}}{M_{ij}M_{ij}} \tag{2.17}$$

where $\mathscr{L}_{ij}$ is the resolved Leonard type stress defined as $\mathscr{L}_{ij} \stackrel{\text{def}}{=} \widetilde{\bar{u}_i\bar{u}_j} - \tilde{\bar{u}}_i\tilde{\bar{u}}_j$, and $M_{ij} \stackrel{def}{=} \alpha_{ij} - \bar{\beta}_{ij}$ is a differential tensor. Here, $\alpha_{ij} \stackrel{\text{def}}{=} 2\tilde{\bar{\Delta}}^2|\tilde{\bar{S}}|\tilde{\bar{S}}_{ij}$ and $\beta_{ij} \stackrel{\text{def}}{=} 2\bar{\Delta}^2|\bar{S}|\bar{S}_{ij}$ are two base stress tensors at the grid and test-grid levels, respectively. In the above equations, the filtered quantities at the grid level are denoted using an over bar, while the filtered quantities at the test-grid level for the dynamic procedure are denoted using a tilde. In order to perform the dynamic procedure, the ratio between the filter sizes at the test-grid and grid levels is set to $\tilde{\bar{\Delta}}/\bar{\Delta} = 2$.

The DM has been applied to many flows [33, 41, 47–49], generally with good results. However, the DM has a few drawbacks due to the Smagorinsky constitutive relation adopted in its constitutive relation: (i) similar to the original Smagorinsky model, it assumes equilibrium between dissipation and production of the SGS KE and requires the principal axes of the SGS stress tensor τ_{ij} to be aligned with those of the resolved strain rate tensor $\bar{S}_{ij}$, which then gives an inadequate representation of the SGS stress components [1, 42, 50]; (ii) the model can result in an unrealistic

SGS dissipative effect if the model coefficient is restricted to be positive; (iii) a potential numerical instability can arise due to excessive backscatter of the SGS KE if the model coefficient is allowed to be negative [33, 49]; and (iv) the DM modelling formulation is not bounded and admits a possible singularity when the denominator of the formulation ($M_{ij}M_{ij}$) becomes very small [49]. A plane averaging technique has often been adopted (when a homogeneous plane exists) for the DM to avoid numerical instability due to either excessive backscatter or potential singular situation of the modelling formulation [33, 41, 47, 49].

2.4.2 Dynamic Nonlinear Model (DNM)

In order to overcome the drawbacks of the DM mentioned above, Wang and Bergstrom [1] recently proposed a dynamic nonlinear model (DNM) for evaluating the SGS stress tensor. The constitutive relation for the DNM is based on an explicit nonlinear quadratic tensorial polynomial constitutive relation originally proposed by Speziale [51] (see also Gatski and Speziale [52]) for modelling of the Reynolds stress tensor in a RANS approach. In the context of LES, the SGS stress is modeled as

$$\tau_{ij}^{*} = -C_S\beta_{ij} - C_W\gamma_{ij} - C_N\eta_{ij} \tag{2.18}$$

In the above equation, the base tensors at grid level are defined as $\beta_{ij} \stackrel{\text{def}}{=} 2\bar{\Delta}^2|\bar{S}|\bar{S}_{ij}$, $\gamma_{ij} \stackrel{\text{def}}{=} 4\bar{\Delta}^2(\bar{S}_{ik}\bar{\Omega}_{kj} + \bar{S}_{jk}\bar{\Omega}_{ki})$ and $\eta_{ij} \stackrel{\text{def}}{=} 4\bar{\Delta}^2(\bar{S}_{ik}\bar{S}_{kj} - \bar{S}_{mn}\bar{S}_{nm}\delta_{ij}/3)$. Here, δ_{ij} is the Kronecker delta; $\bar{\Omega}_{ij} \stackrel{\text{def}}{=} \frac{1}{2}\big(\frac{\partial\bar{u}_i}{\partial x_j} - \frac{\partial\bar{u}_j}{\partial x_i}\big)$ is the resolved rotation rate tensor. According to Wang and Bergstrom [1], the values of the three model coefficients C_S, C_W and C_N can be determined by minimizing the residual of the Germano identity following the dynamic procedure of Lilly [2] as

$$\begin{bmatrix} M_{ij}M_{ij} & M_{ij}W_{ij} & M_{ij}N_{ij} \\ W_{ij}M_{ij} & W_{ij}W_{ij} & W_{ij}N_{ij} \\ N_{ij}M_{ij} & N_{ij}W_{ij} & N_{ij}N_{ij} \end{bmatrix} \cdot \begin{bmatrix} C_S \\ C_W \\ C_N \end{bmatrix} = - \begin{bmatrix} \mathscr{L}_{ij}^{*}M_{ij} \\ \mathscr{L}_{ij}^{*}W_{ij} \\ \mathscr{L}_{ij}^{*}N_{ij} \end{bmatrix} \tag{2.19}$$

where $W_{ij} \overset{\text{def}}{=} \lambda_{ij} - \tilde{\gamma}_{ij}$ and $N_{ij} \overset{\text{def}}{=} \zeta_{ij} - \tilde{\eta}_{ij}$ are differential tensors; and $\lambda_{ij} \overset{\text{def}}{=} 4\tilde{\bar{\Delta}}^2(\tilde{\bar{S}}_{ik}\tilde{\bar{\Omega}}_{kj} + \tilde{\bar{S}}_{jk}\tilde{\bar{\Omega}}_{ki})$ and $\zeta_{ij} \overset{\text{def}}{=} 4\tilde{\bar{\Delta}}^2(\tilde{\bar{S}}_{ik}\tilde{\bar{S}}_{kj} - \tilde{\bar{S}}_{mn}\tilde{\bar{S}}_{nm}\delta_{ij}/3)$ are base tensors at the test-grid level.

The design of the constitutive relation of Eq. 2.18, in terms of the choice of the three constituent tensorial base components, β_{ij}, γ_{ij} and η_{ij}, is not arbitrary: (i) the first term β_{ij} is the well-known Smagorinsky component which primarily relates to the SGS dissipation and forward scatter of turbulent kinetic energy (TKE) from the resolved to SGS motions; (ii) the second term γ_{ij} does not make any contribution to the TKE transfer between the resolved and subgrid scales, however, it significantly improves the correlation between the exact τ_{ij} extracted from a direct numerical simulation (DNS) database and that predicted by the nonlinear model in the *a priori* LES approaches; and (iii) the third term η_{ij} contributes significantly to the backscatter of TKE from the subgrid to the resolved scales [1]. The three features mentioned above, namely, an adequate SGS dissipation level, a high correlation coefficient between the model and exact SGS stresses in *a priori* LES test, and a realistic representation of the TKE backscatter, are among the most important criteria for evaluation of a successful SGS stress model. The Speziale constitutive relation on which the DNM is based, offers an effective representation for modelling these three important physical features separately using three independent tensorial terms. Further investigation and application of the DNM can be found in, in Wang *et al.* [53, 54] on numerical simulation of turbulent channel flows with and without heat transfer, in Xun *et al.* [55] on numerical study of Poiseuille type plane channel flows with and without system rotations, in Wang *et al.* [56] on investigation of the topological features of wall-bounded turbulent flows, and in Wang *et al.* [50] on study of the geometrical properties of the SGS stress tensor.

2.5 Numerical Algorithm

A finite volume method was used to discretise the governing equations to yield a system of linear algebraic equations in the context of a 3D curvilinear coordinate system. To discretise the diffusion term in the filtered momentum equations, a second-order accurate central difference scheme was used. For the convective term, an energy conserving discretisation scheme was used following the approach of Morinishi *et al.* [57]. The transient term was discretised using a three-point backward difference scheme with a constant time step $\Delta t = 1.5 \times 10^{-3}$ seconds. A pressure correction algorithm was applied to the coupled pressure and velocity components stored at the centre of a control volume in accordance with the collocated grid arrangement. At each time step, the pressure field was updated by solving a Poisson type pressure correction equation using an incomplete Cholesky-Conjugate gradient (ICCG) [58] method. The checkerboard effect in the pressure field arising from the pressure-velocity decoupling on a collocated grid system was removed using a nonlinear momentum interpolation scheme [59] for the evaluation of cell-face velocities from the nodal values. Overall the in-house code is second-order accurate with respect to both temporal and spatial resolutions. In order to make the thesis concise, a detailed numerical procedure for the finite volume approach is documented separately in Appendix A.

2.6 Boundary Conditions

The inlet boundary condition is very important for studying pulsatile laminar-turbulent transition flows. The physiological pulsatile laminar velocity profile used for generating the time-dependent pulsatile boundary condition at the inlet of the channel, was obtained through an analytical solution to the Navier-Stokes equation in the context of a fully-developed laminar channel flow when the pressure gradient is approximated as a temporal Fourier series, $\frac{\partial \bar{p}}{\partial x} = \frac{2}{3}A_0 + A\sum_{n=1}^{N} M_n e^{i(n\omega t+\phi_n)}$ (see, Womersley [60]). The solution takes the following form

$$u(y,t) = \bar{U}[1 - 4\frac{y^2}{h^2}] + \sum_{n=1}^{N} \frac{M_n A h^2}{in\mu\alpha^2}[1 - \frac{\cosh(\sqrt{in}\alpha\frac{y}{h})}{\cosh(\sqrt{in}\alpha\frac{1}{2})}]e^{i(n\omega t+\phi_n)} \tag{2.20}$$

In the above equation, constants A_0 and A correspond to the steady and oscillatory parts of the pressure gradient; M_n and ϕ_n represent coefficients and the phase angle, N is the number of harmonics of the flow set to 4 (considering only the first four harmonics of the pressure pulse, which are necessary for modelling realistic arterial blood waveforms); $\omega \stackrel{\text{def}}{=} \frac{2\pi}{T}$ is the frequency of the pulsations, T is the time period of a pulsation cycle and $i = \sqrt{-1}$ is the unit imaginary number. In order to make the thesis concise, detailed mathematical derivation of the inlet boundary condition is documented separately in Appendix B.

At the outlet of the channel, the convective boundary condition is used, viz.

$$\frac{\partial \bar{u}_i}{\partial t} + \bar{U}_c \frac{A_{kj}}{|\mathbf{J}|}\frac{\partial \bar{u}_j}{\partial \xi_k} = 0 \tag{2.21}$$

where $\bar{U}_c$ is the mean convective velocity at the outlet. In the spanwise direction, a periodic boundary condition is applied. Thus the field at two spanwise boundaries Γ_1 and Γ_2 is set to be identical, i.e.

$$\bar{u}_j(x;t)|_{\Gamma_1} = \bar{u}_j(x;t)|_{\Gamma_2} \tag{2.22}$$

$$\bar{p}_p(x;t)|_{\Gamma_1} = \bar{p}_p(x;t)|_{\Gamma_2} \tag{2.23}$$

No slip and no penetration boundary condition is applied to all solid surfaces.

2.7 Data Processing and Flow Statistics

Owing to the presence of pulsations, it requires that the calculation of statistics be carefully dealt with. Three averaging techniques are involved, including phase averaging between different pulsation cycles, time-averaging, and spatial-averaging along the homogeneous (spanwise) direction. Furthermore, these three averaging

methods need to be properly coupled in the calculations in order to reveal properly the statistical properties of the pulsatile flow field. In general, the statistical method adopted here is similar to those used in Mittal *et al.* [31] and Varghese *et al.* [27]. In the following context, it is beneficial to clarify these basic averaging techniques.

For a filtered generic flow variable in LES, $\bar{f}$, time-averaging over the period of time T_f is defined as

$$\left\langle \bar{f} \right\rangle (x,y,z) = \frac{1}{T_f} \int_{t_0}^{t_0+T_f} \bar{f}(x,y,z,t)dt \tag{2.24}$$

where t_0 is the initial time, $T_f = MT$ and M is the total number of pulsatile cycles. Following the convention, turbulent fluctuations of the filtered flow variable $\bar{f}$ with respect to time-averaging can be determined through the following decomposition

$$f^{'}(x,y,z,t) = \bar{f}(x,y,z,t) - \left\langle \bar{f} \right\rangle (x,y,z) \tag{2.25}$$

In the spanwise direction, the flow field is statistically homogeneous. Spatial-averaging along the spanwise direction can be performed as

$$\left\langle \bar{f} \right\rangle_s (x,y,t) = \frac{1}{L_z} \int_0^{L_z} \bar{f}(x,y,z,t)dz \tag{2.26}$$

where $L_z = 3h$ is the width of the channel. In order to separate small turbulent fluctuations from the large pulsatile fluctuations, a phase-averaging technique is needed (Hussain and Reynolds [61] and Mittal *et al.* [31]). Phase-averaging over T_f (for M pulsatile cycles) is defined as

$$\left\langle \bar{f} \right\rangle_p (x,y,t) = \frac{1}{M} \sum_{m=0}^{M-1} \left\langle \bar{f} \right\rangle_s (x,y,t+mT) \tag{2.27}$$

In order to determine the root mean square (RMS) value of a flow variable, all three averaging techniques mentioned here are needed. First, both phase-averaging and spatial-averaging (spanwise) are applied to all pulsatile cycles; and second, an instantaneous field (of the same phase) is compared with the phase- and spatial-averaged field to extract the random fluctuations within each pulsatile

cycle. After completing these two steps, the influence of large pulsation fluctuations (see, Fig. 4.2(a)) on the obtained random fluctuating field is removed, which can be thereafter considered as statistically homogeneous with respect to time at an arbitrary spatial location. The random fluctuating field is calculated as

$$f''(x,y,z,t) = \bar{f}(x,y,z,t) - \left\langle \bar{f} \right\rangle_{sp}(x,y,t) \tag{2.28}$$

Based on the above steps, it is now possible to use time-averaging to determine the RMS values over the total computational time T_f

$$f_{rms} = \sqrt{\frac{1}{T_f}\int_{t_0}^{t_0+T_f} f''^2 dt} \tag{2.29}$$

In the above equations, we used subscripts p and s to denote phase-averaging and spatial-averaging, respectively. In the remainder of this thesis, a pair of angular brackets $\langle\cdot\rangle$ will be used to represent a time-averaged quantity following Eq. 2.24 when we analyze the numerical results. However, without causing any confusion in symbolism, if a homogeneous dimension presents (typically, along the spanwise direction of the domain), this angular bracket operator will also imply an additional spatial-averaging with respect to that particular homogeneous dimension.

Chapter 3

LES of a Pulsatile Newtonian Flow in a Channel with a Both-Sided Constriction

3.1 Introduction

In this chapter, the LES technique is used to investigate the physics of pulsatile flows through a both-sided constricted channel based on two SGS models: the conventional DM of Lilly [2] (§2.4.1 in chapter 2) and DNM of Wang and Bersgtrom [1] (§2.4.2 in chapter 2). Three different grid arrangements were compared in the study and the results obtained from the simulations for bench test cases were validated against experimental and computational results. The physical characteristics of the flow field have been thoroughly studied in terms of the resolved mean velocity, turbulence kinetic energy, viscous wall shear stress, resolved and subgrid-scale turbulent shear stresses, local kinetic energy fluxes between the filtered and subgrid scales, and turbulence energy spectra along the central streamline of the domain. The Reynolds number was also changed from 750 to 1800 in order to quantify its effects on the flow characteristics.

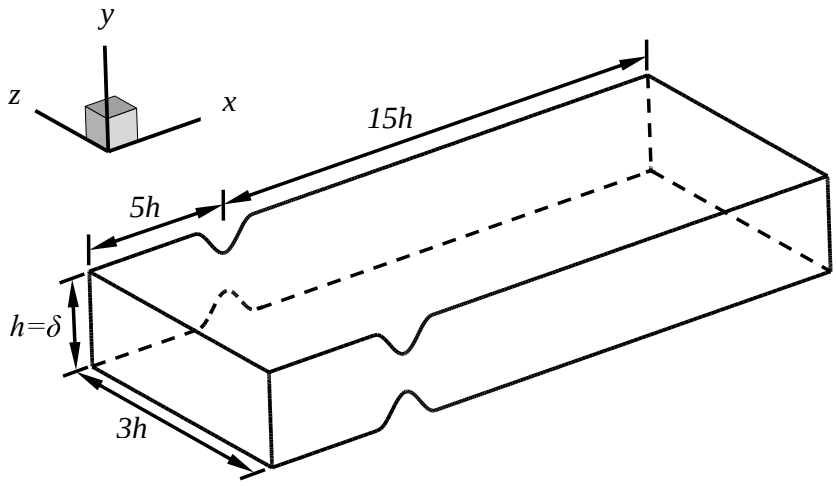

FIGURE 3.1: Schematic of an idealized symmetric stenotic channel and the associated coordinate system.

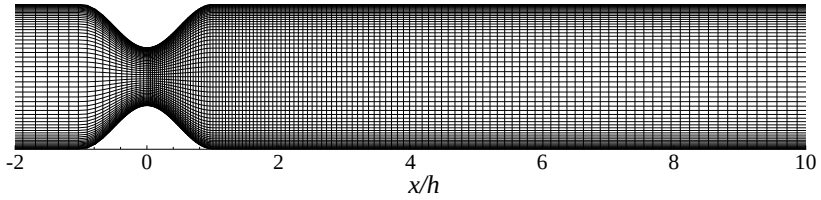

FIGURE 3.2: Mesh configuration displayed in the $x-y$ plane.

3.2 Test Case

The geometry of the computational domain shown in Fig. 3.1 consists of a 3D channel with a both-sided cosine-shaped stenosis on the upper and lower walls centred at $x/h = 0.0$. Here, h is the height of the channel. In the figure, we use x, y and z to represent the streamwise, vertical and spanwise coordinates, respectively. The stenosis is centered $5h$ downstream of the channel inlet and $15h$ away from the channel outlet. The form of the stenosis chosen for this study is

$$\frac{y}{h} = 1 - \frac{f_c}{2}\left(1 + \cos\frac{x\pi}{h}\right), \quad -\frac{h}{2} \leq x \leq \frac{h}{2} \tag{3.1}$$

where f_c is a parameter for controlling the height of the stenosis. In the present study, f_c is fixed to $\frac{2}{5}$, which results in a 60% reduction of the cross-sectional area at the centre of the stenosis.

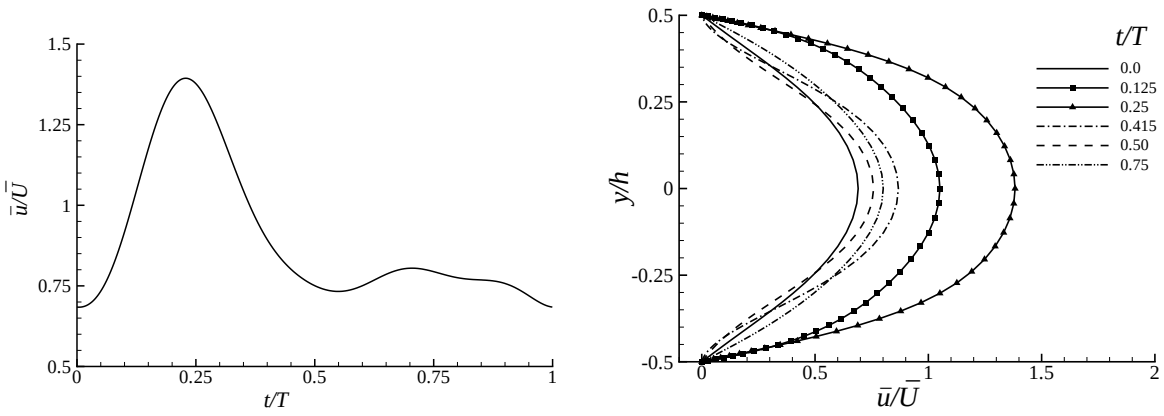

FIGURE 3.3: Instantaneous inlet velocity profile, $\bar{u}/\bar{U}$, for $Re = 1800$ and $\alpha = 10.5$: (a) time history near the wall ($x/h = -5$, $y/h = 0.0057$ and $z/h = 1.5$), and (b) at the different time phases ($x/h = -5$ and $z/h = 1.5$).

In Fig. 3.2, the configuration is displayed in the x-y plane. The no-slip and no-penetration condition is applied on the top and bottom walls of the channel, the meshes are refined in the near-wall regions in order to increase the resolution in the viscous sublayer. The mesh lines are also concentrated at the centre and immediate downstream of the stenosis because these are the regions where energetic vortices and high-level of turbulent fluctuations are generated. Uniform spacing is applied to the spanwise direction.

3.3 Inflow Boundary Condition

The real part of the solution (Eq. B.34) is used as an inlet boundary condition to generate the pulsatile flow. Full solution procedure along with the real part separation is documented systematically in the Appendix B. In the current simulations, the flow Reynolds number is defined as $Re \stackrel{\text{def}}{=} \frac{\bar{U}h}{\nu}$, where $\bar{U}$ is the bulk velocity and ν is the molecular kinematic viscosity. The unsteady Reynolds number is defined as $\alpha^2 \stackrel{\text{def}}{=} h^2 \frac{\rho\omega}{\mu}$, where μ is the molecular dynamic viscosity and α is the Womersley number which reflects the ratio of the pulsatile inertial forces to the viscous forces. If the Womersley number is small (for $\alpha \leq 1$), the frequency of pulsations is low and the

viscous forces dominate flow; and consequently, a cross-sectional parabolic velocity profile develops in response to the instantaneous streamwise pressure gradient (i.e., the Poiseuille flow behaviour) during each pulsation cycle. However, according to Ku [5], if the Womersley number is large (for $\alpha \geq 10$), the frequency of pulsations is high and the pulsatile inertial forces play an important role; and consequently, the phase of the velocity field development lags behind the phase of the instantaneous streamwise pressure gradient (which implies that the flow behaviour deviates from the Poiseuille type). In the present simulation, the Womersley number is fixed to $\alpha = 10.5$, which is a typical number seen in large arteries of humans. For the four different harmonics, the value of M_n is 0.78, 1.32, -0.74 and -0.41 and the value of ϕ_n is 0.0113446, -1.4442599, 0.4625122 and -0.2879793, respectively [60].

The inlet pulsatile velocity profile, derived from Eq. B.34, is demonstrated in Fig. 4.2 for $Re = 1800$. The time history of the velocity field during a full pulsation cycle at a specific near-wall location ($x/h = -5$, $y/h = 0.0057$ and $z/h = 1.5$), is shown in Fig. 4.2(a). The temporal variation of the vertical velocity profile across the center of the inlet plane at different phases over a pulsation cycle is shown in Fig. 4.2(b). It is observed from Fig. 4.2(b) that the velocities are maximum at the systolic phase (at, $t/T = 0.125$ and 0.25).

3.4 Results and Discussions

3.4.1 Validations and Grid Resolution Tests

In order to examine the predictive accuracy of the current numerical algorithm, the LES code has been validated using three similar bench test cases and the numerical results obtained have been compared with the experimental measurement data (on a post-stenotic flow) of Ahmed and Giddens [3], the LES results of Mittal *et al.* [4] and the DNS results of Md. Abul Khair. To be consistent with the experimental conditions of Ahmed and Giddens [3], the flow Reynolds number in the numerical validation is fixed at 1000 (based on the hydraulic diameter $D_h = h$ and bulk velocity

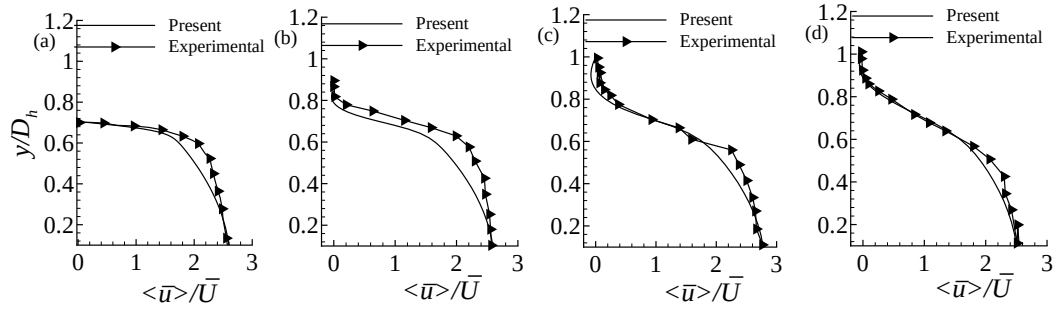

FIGURE 3.4: Comparison of $\langle \bar{u} \rangle / \bar{U}$ with the experimental results of Ahmed and Giddens [3], at (a) $x/D_h = 0$, (b) $x/D_h = 0.5$, (c) $x/D_h = 1$ and (d) $x/D_h = 2$.

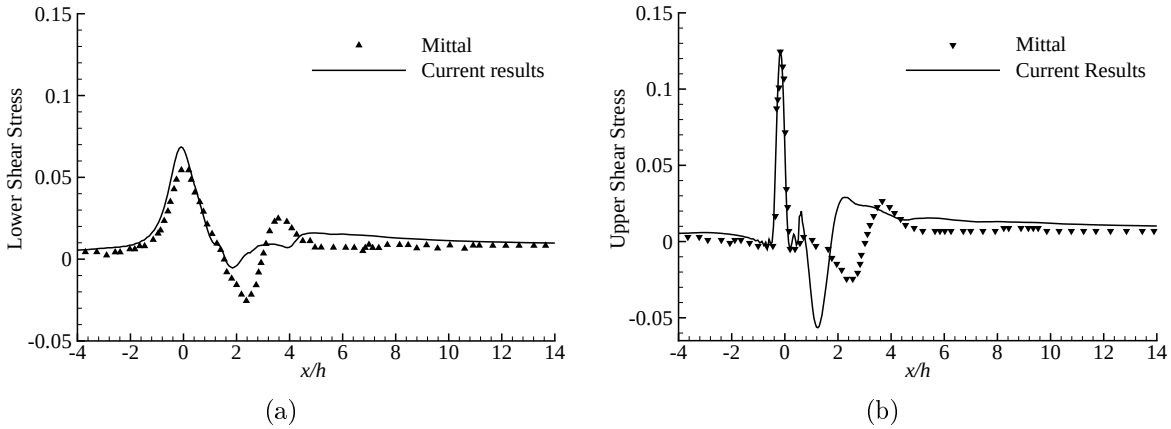

FIGURE 3.5: Comparison of the mean wall shear stresses, $\langle \tau_w \rangle / \frac{1}{2}\rho U_{max}^2$, with the LES results of Mittal *et al.* [4] for $Re = 2000$ when the constriction is semi-circular.

$\bar{U}$) and the boundary condition at the inlet needs to be treated as a fully-developed laminar pipe flow without imposing any pulsations onto the flow field. Also, the lower wall of the model shown in Fig. 3.1 is treated as a symmetrical plane in the current simulations (just for conducting this comparative study in this subsection). Figure 3.4 shows the streamwise velocity at different downstream locations, and it is evident that the present numerical predictions agree well with the experimental results of Ahmed and Giddens [3].

In order to validate the numerical approach against the LES results of Mittal *et al.* [4], we follow their specific test configuration by using a semi-circular instead of a cosine-shaped constriction and a different Reynolds number (based on the maximum or central line velocity U_{max}) defined as $Re_m = Q_{max}/\nu = U_{max}h/\nu$, where Q_{max} is the maximum volume flow rate per unit channel width. In Mittal *et al.* [4], a parabolic

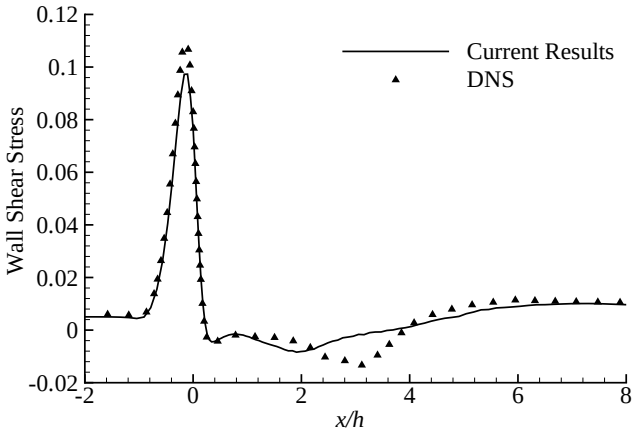

FIGURE 3.6: Comparison of the non-dimensionalized time- and spanwise-averaged profile of the shear stress over both walls, $\langle \tau_w \rangle / \frac{1}{2}\rho \bar{U}^2$, with the DNS result (by courtesy of Md. Abul Khair) for $Re = 2000$.

inflow profile was imposed at the inlet and the flow rate per unit channel width varied in a sinusoidal manner, i.e. $Q(t) = (Q_{max}/2)[1 - \cos 2\pi t/T]$. Following this approach, a parabolic profile $u(y,t) = 2U_{max}(y/h)(1 - y/h) + (U_{max}/4)[1 - \cos 2\pi t/T]$ was enforced at the inlet. One of the key interests of biofluid mechanics is the prediction of the mean wall shear stress $\langle \tau_w \rangle$ as it relates to the vascular rupture (resulting in emergent medical conditions such as internal bleeding and stroke). Figures 3.5(a) and (b) compare the predicted $\langle \tau_w \rangle$ value with the LES result of Mittal *et al.* [4]. The results presented in the figures are non-dimensionalized by $\frac{1}{2}\rho U_{max}^2$ and the simulation was conducted for $Re_m = 2000$ with a grid system of $240 \times 64 \times 40$ (in the x, y and z directions, respectively). Although the predicted patterns in the mean wall shear stress by the current simulation agree in general with the LES results of Mittal *et al.* [4], small discrepancies exist. This may relate to the fact that the physics of flow under simulation is highly unsteady (pulsatile) and it is challenging to calculate statistics as phase-averaging is also involved between different pulsatile cycles. It needs to be indicated that given the complexity of the flow tested here, no further experimental data are available in the current literature for the purpose of comparisons.

Besides the preliminary validation presented above, the LES results were further validated against the DNS data (by courtesy of Md. Abul Khair). This DNS results

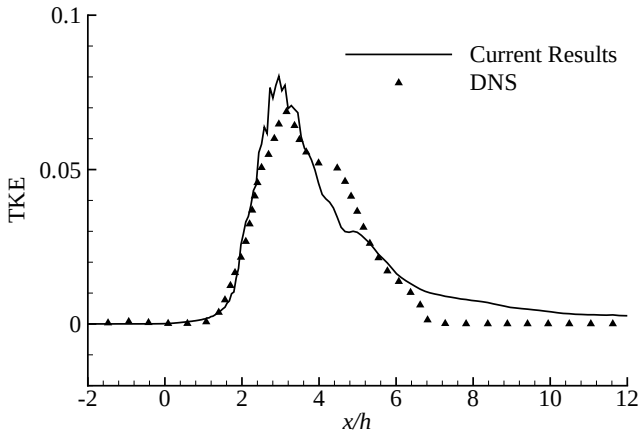

FIGURE 3.7: Comparison of centerline TKE, $k/\bar{U}^2$, with the DNS result (by courtesy of Md. Abul Khair) for $Re = 2000$ with both-sided constriction.

are based on $350 \times 90 \times 90$ control volumes. For this validation, the geometry of the model, boundary conditions, Reynolds number and the Womersley number were kept same for both test cases. The results were compared in terms of the non-dimensional time- and spanwise-averaged wall shear stress, $\langle \tau_w \rangle / \frac{1}{2}\rho\bar{U}^2$ (averaged over both walls), and centerline TKE $k/\bar{U}^2$, for $Re = 2000$. Figures 3.6 and 3.7 show that the LES and DNS results of the mean wall shear stress and TKE agree well with each other except for a small discrepancy in the post-stenotic region.

In order to thoroughly examine the effects of grid resolution on the predicted results, three different grid systems with $150 \times 70 \times 60$ (Case 1), $180 \times 60 \times 50$ (Case 2) and $210 \times 60 \times 50$ (Case 3) control volumes (in the x, y and z directions, respectively) were compared at $Re = 1800$. The three grid systems are body-fitted, reflecting the curvilinear geometry of the computational domain prescribed by Eq. 3.1. Furthermore, from Case 1 to 3, the number of grid points along the streamwise direction (N_x) is increased in order to improve the predictive accuracy of the small-scale turbulent eddy motions within the post-stenotic regime. For Case 1, N_y and N_z were increased. The number of streamwise grid points upstream of the stenosis is always fixed to 30 while the rest of the grid points are distributed within and downstream of the stenosis. The grid is uniform in the spanwise direction and significantly refined in the near-wall region in order to accurately resolve the wall shear stress.

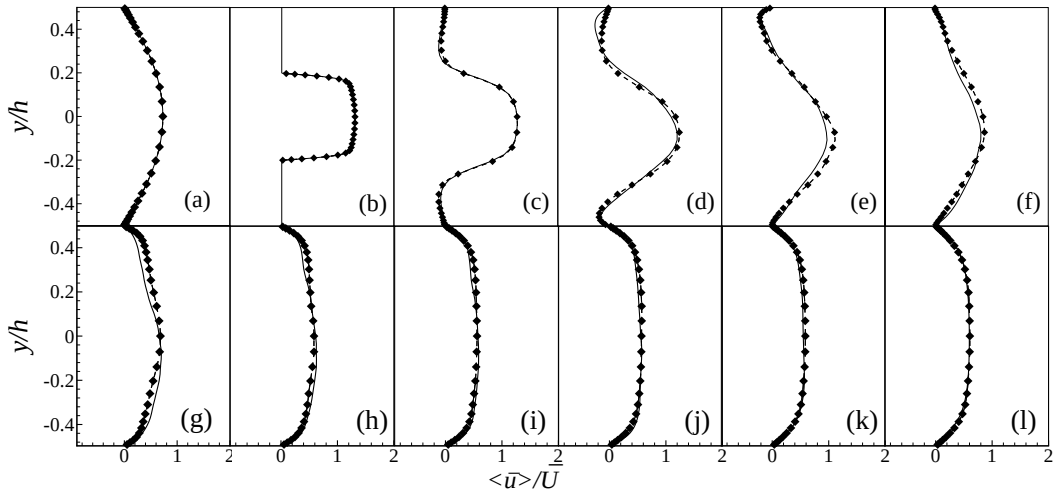

FIGURE 3.8: Grid sensitivity test with respect to the mean streamwise velocity, $\langle\bar{u}\rangle/\bar{U}$, at (a) $x/h = -5$, (b) $x/h = 0$, (c) $x/h = 1$, (d) $x/h = 2$, (e) $x/h = 3$, (f) $x/h = 4$, (g) $x/h = 5$, (h) $x/h = 6$, (i) $x/h = 8$, (j) $x/h = 10$, (k) $x/h = 12$ and (l) $x/h = 15$. Based on three grid systems, Case 1: solid line for $150 \times 70 \times 60$ control volumes, Case 2: dashed line for $180 \times 60 \times 50$ control volumes, and Case 3: solid line with symbols for $210 \times 60 \times 50$ control volumes.

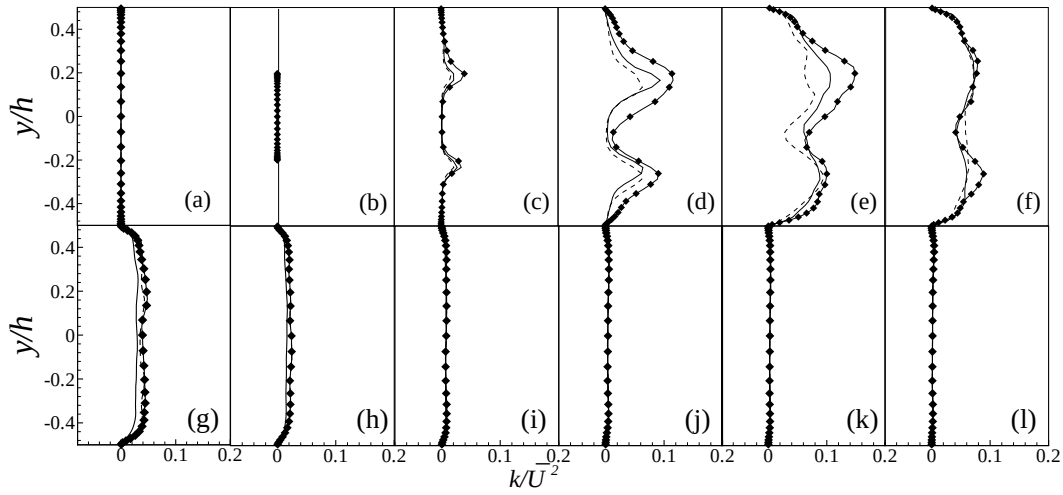

FIGURE 3.9: Grid sensitivity test with respect to the TKE, $k/\bar{U}^2$, at (a) $x/h = -5$, (b) $x/h = 0$, (c) $x/h = 1$, (d) $x/h = 2$, (e) $x/h = 3$, (f) $x/h = 4$, (g) $x/h = 5$, (h) $x/h = 6$, (i) $x/h = 8$, (j) $x/h = 10$, (k) $x/h = 12$ and (l) $x/h = 15$. Based on three grid systems, Case 1: solid line for $150 \times 70 \times 60$ control volumes, Case 2: dashed line for $180 \times 60 \times 50$ control volumes, and Case 3: solid line with symbols for $210 \times 60 \times 50$ control volumes.

The results of Cases 1, 2 and 3 are compared in Figs. 3.8 and 3.9 in terms of the non-dimensionalized time-averaged streamwise velocity (i.e., $\langle\bar{u}\rangle/\bar{U}$) and resolved

TKE (i.e., $k/\bar{U}^2$), respectively, at different locations along the streamwise direction. From Fig. 3.8, it is seen that all three grid configurations used in the present computations (Cases 1, 2 and 3) can predict the mean velocity field correctly and are not sensitive to the grid resolution. However, Fig. 3.9 shows that the results of the non-dimensionalized TKE at the immediate post-stenotic region $1 \leq x/h \leq 6$ (corresponding to Figs. 3.9(c)-(h)), vary slightly with the grid resolution. This may occur because only the velocity fluctuations related to the large resolved scale motions are directly computed at the grid (or, filtered) level in a conventional implicit filtering LES approach.

Given their constitutive relationships which model only the trace-free part of the SGS stress tensor, neither the conventional DM of Lilly [2] nor the DNM of Wang and Bergstrom [1] is capable of determining the modeled component of TKE at the SGS level unless an additional SGS k-equation is solved (which necessarily involves further SGS modelling for closure). However, it has been shown in this study (cf. Fig. 3.8) and in many previous works that the first-order flow statistics (e.g., the filtered velocities) are not sensitive to the grid resolution. Without a special declaration, the numerical results presented in the remainder of this thesis are based on the grid system with $180 \times 60 \times 50$ control volumes (Case 2).

3.4.2 Basic Flow Features

The time-averaged streamlines at the central plane ($z/h = 1.5$) for two different Reynolds numbers $Re = 750$ and 1800 are displayed in Figs. 3.10(a) and (b), respectively. The time-averaged vortical structures of the flow are visualized using the contour of non-dimensionalized mean streamwise velocity $\langle\bar{u}\rangle/\bar{U}$. For all the three Reynolds numbers tested, two recirculation regions (close to the upper and lower walls) appear near the post-lip of the stenosis due to the separation of the shear layer from the nose (or, center location) of the stenosis. At both walls, the location of separation is $(x/h)_{sep} = 0.203$, and the location of reattachment is $(x/h)_{reatt} = 3.39$ for $Re = 1800$. By comparing Figs. 3.10(a) and (b), it is observed that the flow

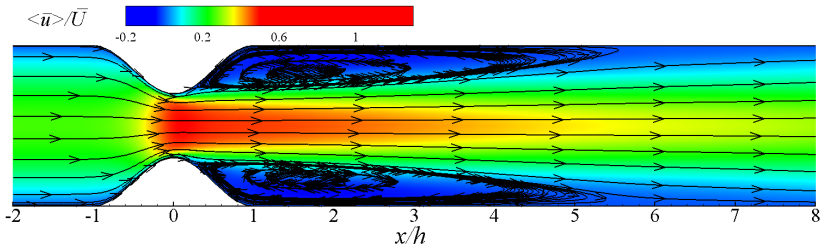

(a)

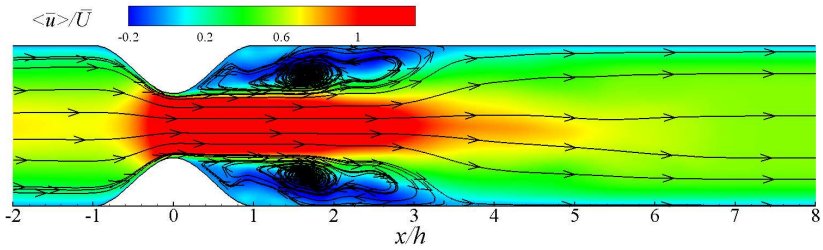

(b)

FIGURE 3.10: Time-averaged streamlines imposed on the contour of non-dimensionalized streamwise mean velocity, $\langle \bar{u} \rangle / \bar{U}$, for (a) $Re = 750$ and (b) $Re = 1800$.

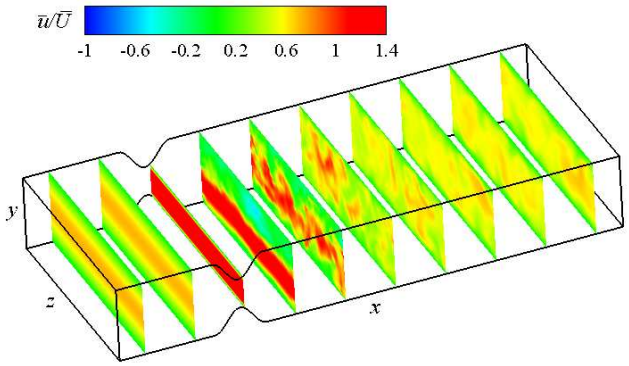

FIGURE 3.11: Slice view of instantaneous streamwise velocity, $\bar{u}/\bar{U}$, for $Re = 1800$ at $t/T = 10.25$.

reattaches earlier at the higher Reynolds number, which agrees qualitatively with the LES result of Mittal *et al.* [31].

Figure 3.11 shows the slice view of the isopleths of the non-dimensionalized instantaneous streamwise velocity field, $\bar{u}/\bar{U}$, at $t/T = 10.25$ for $Re = 1800$. The first two slices show that prior to the stenosis, the flow is laminar and stratified. The third slice shows that the velocity reaches its maximum (primarily due to continuity)

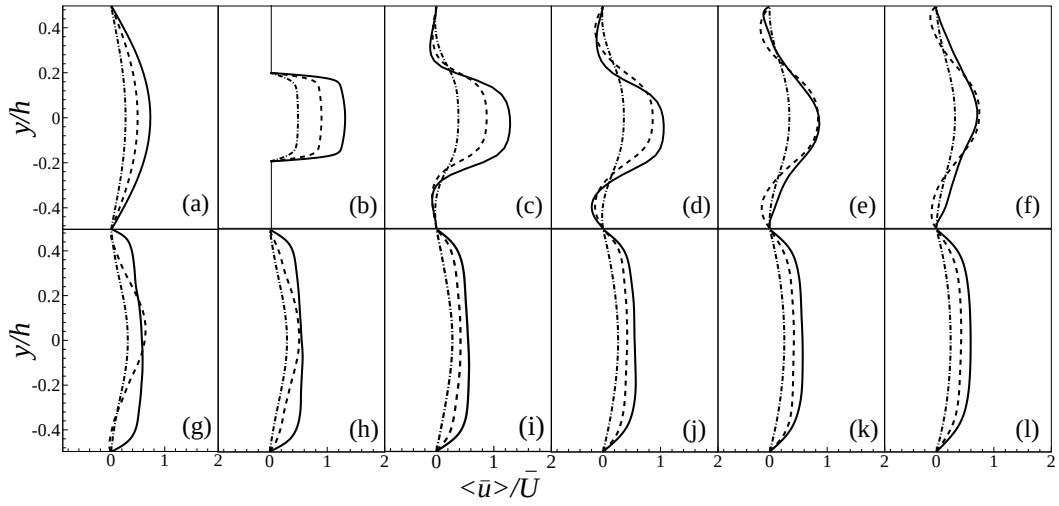

FIGURE 3.12: Time-averaged streamwise velocity, $\langle\bar{u}\rangle/\bar{U}$, at (a) $x/h = -5$, (b) $x/h = 0$, (c) $x/h = 1$, (d) $x/h = 2$, (e) $x/h = 3$, (f) $x/h = 4$, (g) $x/h = 5$, (h) $x/h = 6$, (i) $x/h = 8$, (j) $x/h = 10$, (k) $x/h = 12$ and (l) $x/h = 15$. Case 1: solid line for $Re = 1800$, Case 2: dashed line for $Re = 1200$, and Case 3: dashdot line for $Re = 750$.

at the throat location ($x/h = 0$) of the stenosis. The fourth slice shows a very interesting instantaneous flow pattern: in the immediate post-stenotic region, the velocity is very large (indicated by the red colour) close to the lower wall, however, the velocity is negative (indicated by the blue colour) in the recirculation region close to the upper wall. Turbulence is triggered by the stenosis. However, as indicated by the last two slices, gradually, the flow becomes re-laminarized in the far downstream region.

The mean streamwise velocity profiles for the different Reynolds numbers, Re= 750, 1200 and 1800, are depicted in Fig. 3.12 at the different streamwise positions. Note that the velocity results in the figure have been non-dimensionalized using by the bulk velocity, $\bar{U}$. At the inlet, the mean velocity profiles have a parabolic shape (frame (a)) because the flow before the stenosis is fully developed and laminar. But the separated shear layers from the throat break down this parabolic shape in the post-lip region due to the presence of the adverse streamwise pressure gradient. However, towards the far downstream region, the velocity profiles become non-parabolic to reflect turbulent flow pattern. It is also evident from the figures that the time-averaged

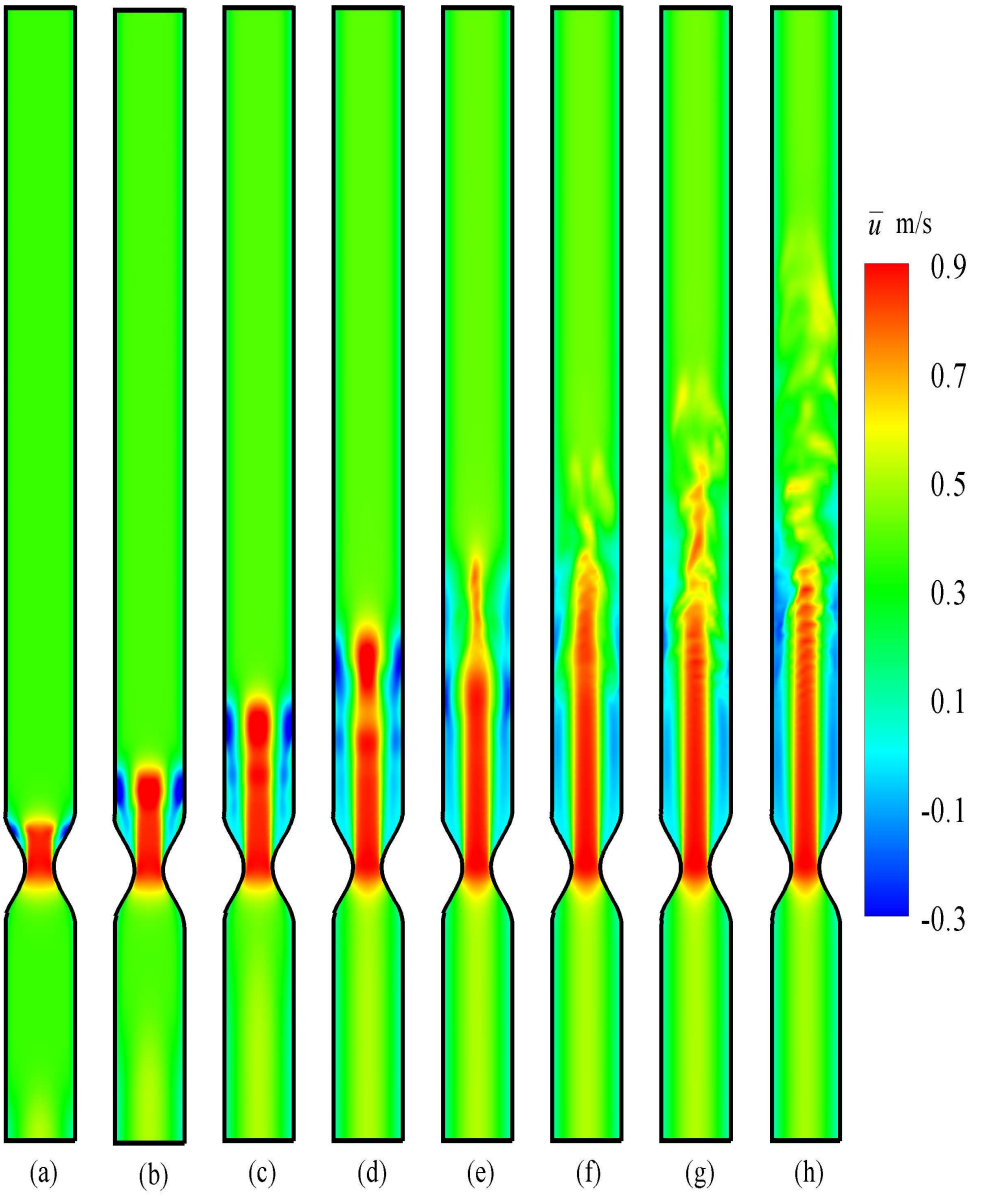

FIGURE 3.13: Streamwise velocity, $\bar{u}$, at: (a) $t/T = 1$, (b) $t/T = 2$, (c) $t/T = 3$, (d) $t/T = 4$, (e) $t/T = 5$, (f) $t/T = 6$, (g) $t/T = 7$ and (h) $t/T = 8$ for $Re = 1800$.

streamwise velocity at all locations is higher for the larger Reynolds numbers.

In Fig. 3.13, the cycle-to-cycle flow development is shown using the contour plots of the streamwise velocity, $\bar{u}$, for $Re = 1800$. In frame (a), it is observed that at the end of the first cycle, two small re-circulation regions near the two walls are created. A primary shear layer which is initially created at the center of the stenosis propagates towards the downstream region at the end of the second cycle (see, frame

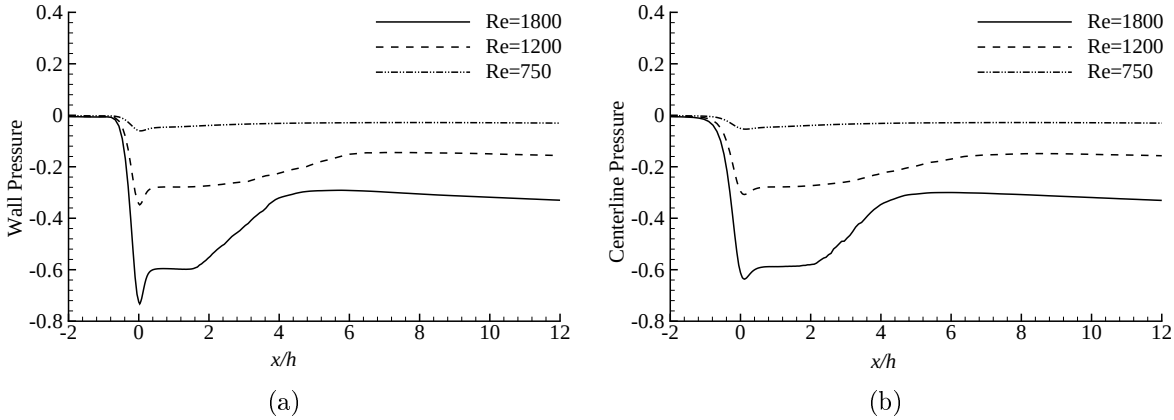

FIGURE 3.14: Time-averaged pressure, $\langle \bar{p} \rangle / \frac{1}{2}\rho \bar{U}^2$, at(a) walls and (b) centerline for different Reynolds number.

(b)). As shown clearly in frames (c)-(h), as the flow field evolves with time, the shear layers elongates and finally breaks down into vortices and triggers the turbulent flow pattern. The simulation has been carried out up to the end of the eleventh cycle, as it has been tested that the solutions eventually reach to a stationary state after the fourth cycle, and the flow statistics accumulated after the fourth cycle (to be presented in the next section) do not vary significantly between the fifth and eleventh cycles.

The nondimensional time-averaged pressure ($\langle \bar{p} \rangle / \frac{1}{2}\rho \bar{U}^2$) distributions at walls and centreline are presented in Fig. 3.14 for the different Reynolds numbers. Owing to the constriction of the channel, right after the stenosis, the pressure drops significantly at walls as well as at the centerline. The maximum pressure drop occurs within the immediate post-stenotic region for $0 < x/h < 3$. Note that the flow also recirculates in this region due to the adverse pressure gradient.

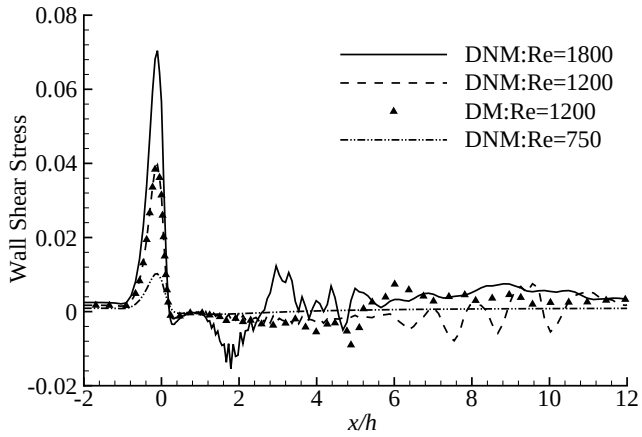

FIGURE 3.15: Instantaneous profile of the wall shear stress, $\langle \tau_w \rangle / (\frac{1}{2}\rho \bar{U}^2)$.

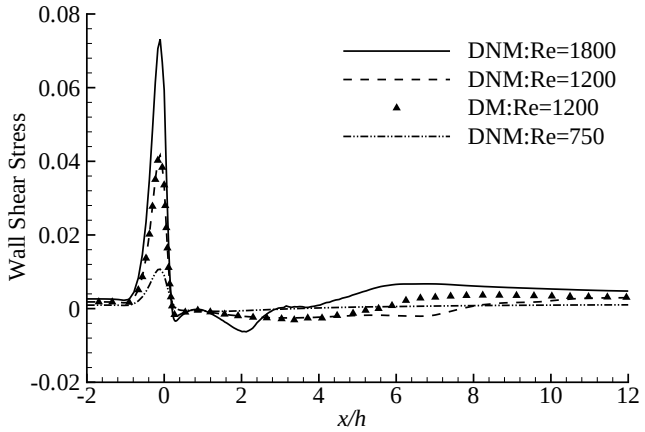

FIGURE 3.16: Time- and spanwise-averaged profile of the wall shear stress, $\langle \tau_w \rangle / (\frac{1}{2}\rho \bar{U}^2)$.

3.4.3 Wall Shear Stresses

Figure 3.15 shows the instantaneous streamwise profile of the wall shear stress, $\langle \tau_w \rangle \stackrel{\text{def}}{=} \mu \frac{\partial \bar{u}}{\partial y}|_w$ (non-dimensionalized using $\frac{1}{2}\rho \bar{U}^2$). The acute wall shear stress rises to its maximum just upstream of the center of the stenosis due to the large vertical gradient of the mean streamwise velocity. Immediately downstream of the stenosis, the wall shear stress becomes negative which is consistent with the flow pattern in the large recirculation zone. Further downstream of the recirculation zone $2 < x/h < 6$, the instantaneous wall shear stress oscillates, albeit with a smaller magnitude. The physical mechanism underlying these oscillations associated with the stenosis are of significant interest in biofluid mechanics, as they may be responsible for the damage of

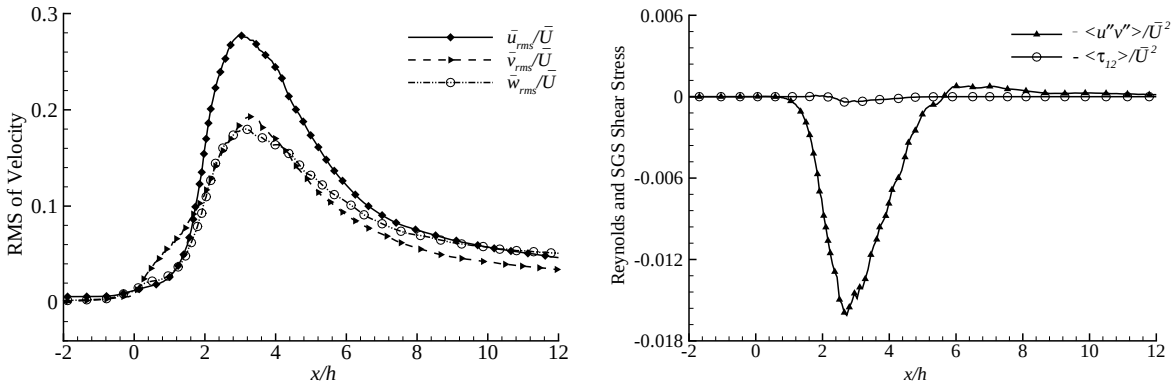

(a) (b)

FIGURE 3.17: Non-dimensionalized profiles for (a) the RMS velocities $\bar{u}_{rms}/\bar{U}$, $\bar{v}_{rms}/\bar{U}$ and $\bar{w}_{rms}/\bar{U}$, and (b) the averaged resolved Reynolds stress $-\langle u''v''\rangle/\bar{U}^2$ and SGS stress $-\langle\tau_{12}\rangle/\bar{U}^2$ at $y/\delta = 0.5$ for $Re = 1800$.

the inner lining of an arterial vessel. Fig. 3.16 shows the time- and spanwise-averaged wall shear stress $\langle\tau_w\rangle\,/(\frac{1}{2}\rho\bar{U}^2)$ over the walls. As shown in Fig. 3.16, following a sharp rise close to the center of the stenosis, the wall shear stress drops rapidly, becomes negative in the region $1 < x/h < 2$, and then maintains a small finite value in the further downstream region. In Figs. 3.15 and 3.16, a comparison is also made between the DM and the DNM at $Re = 1200$ in terms of their prediction of the mean shear stress at the wall. As expected, there is no significant difference between these two SGS stress models here. This is because the mean wall shear stress is determined by the mean velocity field, which is a first-order moment and should not be sensitive to the SGS stress models adopted.

3.4.4 Second Order Moments

Figure 3.17(a) shows non-dimensionalized profiles of the root mean square (RMS) velocities, $\bar{u}_{rms} \stackrel{\text{def}}{=} \langle u''^2\rangle^{1/2}$, $\bar{v}_{rms}$ and $\bar{w}_{rms}$ (defined similarly) along the central streamline of the domain ($y/\delta = 0.5$). As shown in Fig. 3.17(a), the value of $\bar{u}_{rms}/\bar{U}$, $\bar{v}_{rms}/\bar{U}$ and $\bar{w}_{rms}/\bar{U}$ are very close to zero at the inlet reflecting the nature of the laminar pulsatile flow pattern in the upstream region (see Fig. 3.9). However, after the centre of the stenosis, the RMS values of the velocities begin to increase and become

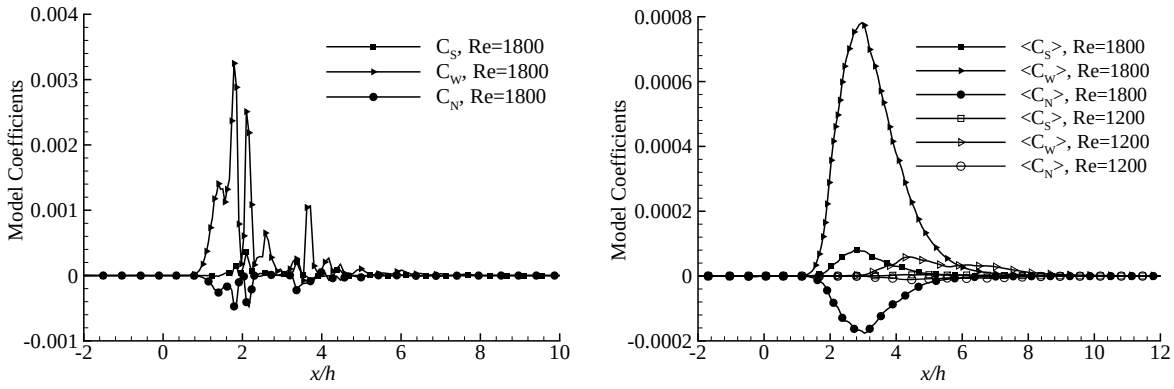

(a) (b)

FIGURE 3.18: Model coefficients for the DNM, (a) instantaneous coefficients C_S, C_W and C_N along the central streamline of the domain ($y/\delta = 0.5$, $z/h = 1.5$), and (b) time- and spanwise-averaged coefficients $\langle C_S \rangle$, $\langle C_W \rangle$ and $\langle C_N \rangle$ at $y/h = 0.5$.

prominent in the immediate post-stenotic region ($0 < x/h < 6$). Far downstream of the stenosis ($x/h > 6$), the flow is still turbulent but the intensity decreases gradually. Based on the above analysis, it is concluded that turbulent fluctuations are triggered by and highly dependent upon the presence of the stenosis.

The distribution of the non-dimensionalized resolved Reynolds shear stress, $-\langle u''v'' \rangle/\bar{U}^2$, and SGS shear stress, $-\langle \tau_{12} \rangle/\bar{U}^2$, along the central streamline of the domain, are shown in Fig. 3.17(b). Because the flow pattern is primarily laminar upstream of the stenosis, the Reynolds stress $-\langle u''v'' \rangle/\bar{U}^2$ and SGS stress $-\langle \tau_{12} \rangle/\bar{U}^2$, are almost zero. The resolved turbulent stress drops within the region $1 < x/h < 6$ where turbulence is triggered by the stenosis. Both the stresses approaches zero at the far downstream region ($x/h > 5.3$) due to re-laminarization.

3.4.5 SGS Model Coefficients and TKE Production

The instantaneous distribution of the DNM coefficients for $Re = 1800$ along the central streamline of the channel (located at $y/\delta = 0.5$ and $z/h = 1.5$) are displayed in Fig. 3.18(a). It is observed that the extreme values of the instantaneous model coefficients occur within the post-stenotic region $1 < x/h < 6$, where the peak values of the averaged coefficients are also observed in Fig. 3.19.

Figure 3.18(b) shows the time- and spanwise-averaged DNM coefficients $\langle C_S \rangle$, $\langle C_W \rangle$ and $\langle C_N \rangle$ along the streamwise direction for $Re = 1200$ and 1800. From the figure, it is clear that from the inlet to the throat of the stenosis (i.e., $-5 < x/h < 0$), the viscous forces are dominant and the flow pattern is primarily laminar. Therefore, the SGS stress model is not activated, and as a consequence, all three DNM coefficients are very close to zero. Downstream of the center of the stenosis, the DNM is fully activated and its coefficients reach their maximum values around $x/h = 3$ and then gradually decrease to zero in the region far downstream of the stenosis to reflect the re-laminarization process (over which the DNM gradually become deactivated). The inherent self-calibration mechanism of the DNM coefficients is very responsive to the varying SGS stress level characteristic of a laminar-turbulent-laminar transitional flow through a modeled stenosis. The distribution of the DNM coefficients are anisotropic in the streamwise direction due to the presence of the stenosis. In the core turbulent region (i.e., $1 < x/h < 6$), the mean value is positive for $\langle C_S \rangle$ and $\langle C_W \rangle$ but negative for $\langle C_N \rangle$. Similar behaviour was reported by Wang and Bergstrom [1] in their study of a fully-developed turbulent channel flow. It is also clear from Fig. 3.18(b) that as the Reynolds number increases from 1200 to 1800, the magnitudes of $\langle C_S \rangle$, $\langle C_W \rangle$ and $\langle C_N \rangle$ all increase.

In order to examine the influence of the grid resolution on the dynamic model coefficients of the DNM, three grid systems are tested. As shown in Fig. 3.19, in general, the magnitude of all three averaged dynamic coefficients increases as the grid resolution reduces. This is an expected modelling feature, because in a conventional implicit filtering LES approach, the SGS effects increases as the grid resolution decreases (owing to the fact the filter size is coupled with the grid size). Furthermore, from Figs. 3.19(a)-(c), we can conclude that the magnitude of $\langle C_W \rangle$ and $\langle C_N \rangle$ is one order of magnitude higher than that of $\langle C_S \rangle$, which indicates that the nonlinear SGS modelling effects as represented by γ_{ij} and η_{ij} (related to C_W and C_N in Eq. 2.18, respectively) are significant for the current complex flow tested.

In LES, the resolved and unresolved SGS motions interact with each other such that the TKE of the flow dynamically transfers between these two scales of flow

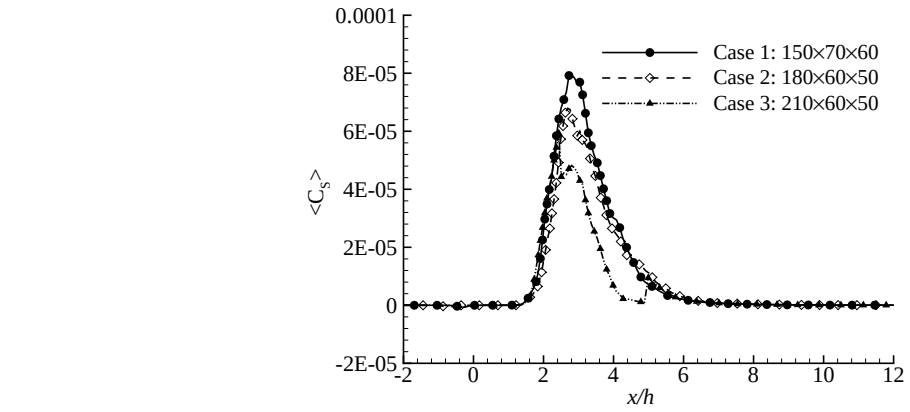

(a)

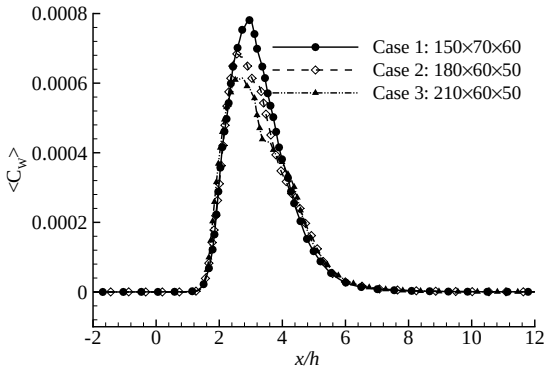

(b)

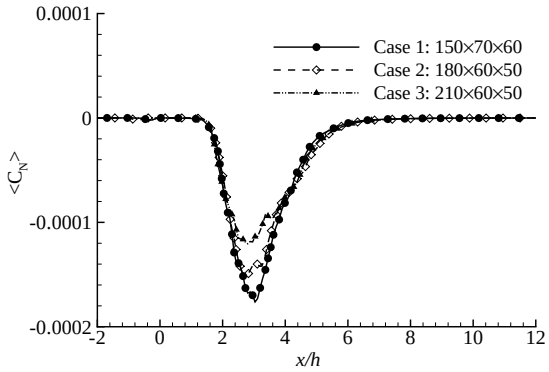

(c)

FIGURE 3.19: Sensitivity of the time- and spanwise-averaged DNM coefficients to the grid resolution for $Re = 1800$ at $y/\delta = 0.5$.

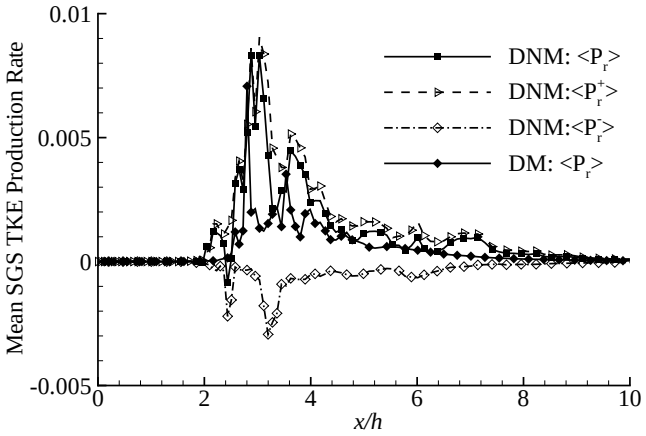

FIGURE 3.20: Time- and spanwise-averaged non-dimensionalized SGS TKE production rate at $y/h = 0.5$ for $Re = 1800$: total, $\langle P_r \rangle / \langle \varepsilon \rangle$; forwardscatter, $\langle P_r{}^+ \rangle / \langle \varepsilon \rangle$; and backscatter, $\langle P_r{}^- \rangle / \langle \varepsilon \rangle$.

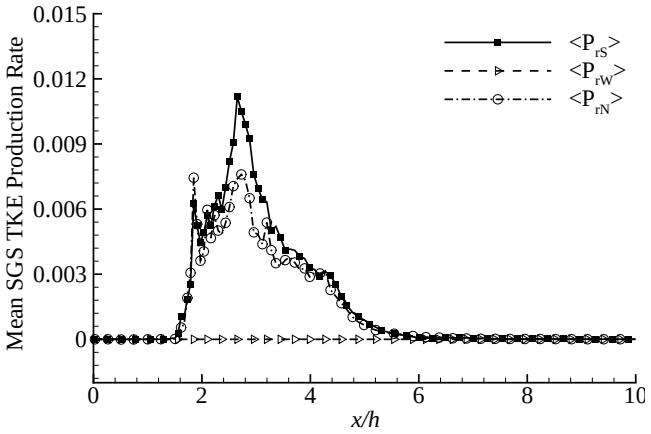

FIGURE 3.21: Time- and spanwise-averaged non-dimensionalized SGS TKE production rate components at $y/h = 0.5$ for $Re = 1800$: $\langle P_{rS}\rangle/\langle\varepsilon\rangle$, $\langle P_{rW}\rangle/\langle\varepsilon\rangle$ and $\langle P_{rN}\rangle/\langle\varepsilon\rangle$.

motions. The averaged SGS TKE production rate is defined as $\langle P_r\rangle \stackrel{\text{def}}{=} \langle -\tau_{ij}^* \bar{S}_{ij}\rangle$, which acts as a sink of TKE for the large-scale (or, filtered) motions but as a source of TKE for the SGS motions. It has been confirmed that the value of the local SGS TKE production rate, P_r, can be either positive or negative, indicating forward or backward scattering of the SGS TKE between the filtered and subgrid scales, respectively [1]. In the context of the DNM, the averaged SGS TKE production term takes the following form

$$\langle P_r\rangle = \langle C_S \beta_{ij} \bar{S}_{ij}\rangle + \langle C_W \gamma_{ij} \bar{S}_{ij}\rangle + \langle C_N \eta_{ij} \bar{S}_{ij}\rangle = \langle P_{rS}\rangle + \langle P_{rW}\rangle + \langle P_{rN}\rangle \qquad (3.2)$$

Similar to other scalar quantities such as the resolved TKE, viscous dissipation rate of TKE and thermal energy, the transport of P_r also involves transient evolution, diffusion and convection. Figure 3.20 compares the total mean SGS TKE production rate $\langle P_r\rangle$ as well as the forward scatter $\langle P_r^+\rangle$ and backscatter $\langle P_r^-\rangle$ (non-dimensionalized using the mean resolved viscous dissipation rate $\langle\epsilon\rangle \stackrel{\text{def}}{=} \langle 2\nu \bar{S}_{ij} \bar{S}_{ij}\rangle$) predicted by the DNM and DM at $Re = 1800$. As shown in the figure, for the prediction of the DNM, there exists both forward and backward scattering of TKE between the filtered and subgrid scales within and immediately after the stenosis. In the region upstream of the post-lip of the stenosis (i.e., $x/h < 1$) and far downstream

of the stenosis (i.e., $x/h > 6$), the level of TKE production rate $\langle P_r \rangle$ is close to zero. This is because the flow is either laminar or the turbulence intensity level is extremely low in these regions. From Fig. 3.20, it is also observed that the forward scatter $\langle P_r^+ \rangle$ is slightly higher than the total SGS TKE production rate $\langle P_r \rangle$. This is because the total SGS TKE production rate must balance to verify $\langle P_r \rangle = \langle P_r^+ \rangle + \langle P_r^- \rangle$.

In comparison with the $\langle P_r \rangle$ expression for the DNM shown in Eq. 3.2, the $\langle P_r \rangle$ term for the DM of Lilly [26] takes the following form

$$\langle P_r \rangle = \left\langle C_S \beta_{ij} \bar{S}_{ij} \right\rangle = \left\langle C_S \bar{\Delta}^2 \left| \bar{S} \right|^3 \right\rangle \tag{3.3}$$

which is seemingly identical to $\langle P_{rS} \rangle$, the first component in Eq. 3.2, in terms of the mathematical format. However, there is a significant difference: in the DM, C_S is the only dynamic model coefficient; in contrast, in the DNM, C_S is one of the three dynamic coefficients. From the previous discussion, it is understood that C_S in the DNM relates to the linear Smagorinsky constituent component and its magnitude is influenced by that of C_W and C_N (which relate to the two nonlinear constituent components). In Fig. 3.20, the total time- and spanwise-averaged $\langle P_r \rangle$ predicted by the DM is demonstrated, however, no mean backscatter is observed (i.e., $\langle P_r^- \rangle$ is zero identically).

Figure 3.21 shows the time- and spanwise-averaged TKE production rates contributed by the three individual constituent terms of the DNM [1] (i.e., $\langle P_{rS} \rangle$, $\langle P_{rW} \rangle$ and $\langle P_{rN} \rangle$) for $Re = 1800$ along the central streamline of the domain ($y/\delta = 0.5$). This figure shows that the SGS TKE production rates associated with first and third terms $\langle P_{rS} \rangle$ and $\langle P_{rN} \rangle$ increase significantly immediately after the center of the stenosis and attain their peak values at approximately $x/h = 2.5 - 2.8$. The SGS TKE production rate associated with the second term $\langle P_{rW} \rangle$ is negligible, which is in conformance with the analysis of Wang and Bergstrom [1] that P_{rW} is strictly zero due to the special tensorial relationship between the strain rate tensor $\bar{S}_{ij}$ and rotation rate tensor $\bar{\Omega}_{ij}$, i.e. $P_{rW} = C_W \gamma_{ij} \bar{S}_{ij} = 4 C_W \bar{\Delta}^2 (\bar{S}_{ik} \bar{\Omega}_{kj} - \bar{\Omega}_{ik} \bar{S}_{kj}) \bar{S}_{ij} \equiv 0$, because $\bar{S}_{ij}$ is a symmetric tensor and $\bar{\Omega}_{ij}$ is an antisymmetric tensor.

The conventional DM of Germano *et al.* [41] and Lilly [2] is well-known for its advantages such as self-calibration and being free from a need for any empirical constants and any *ad hoc* wall damping functions near solid surfaces. The observation that the DM fails to predict properly the backscatter of SGS TKE has been reported extensively in the literature [1,33,62,63], which represents a major difference between the conventional DM and the DNM. This particular drawback of the DM is related to the linear Boussinesq hypothesis implied in its constitutive relationship, which assumes that the principal axes of the negative SGS stress tensor $-\tau_{ij}$ are exactly aligned with those of the resolved strain rate tensor $\bar{S}_{ij}$. This inevitably leads to an inadequate geometrical representation of the SGS stress components [1]. Wang *et al.* [50] studied the tensorial geometrical relationship between the $-\tau_{ij}$ and $\bar{S}_{ij}$ based on the Euler rotation angle and axis (which quantifies the attitude of the eigenframe of $-\tau_{ij}$ with respect to that of $\bar{S}_{ij}$). They proved that because of the Boussinesq hypothesis, the Euler rotation angle is strictly 0^o and the Euler axis is undefined corresponding to a special singular condition. This interesting mathematical property is unique for the linear constitutive relationship between $-\tau_{ij}$ and $\bar{S}_{ij}$ implied in the DM. In contrast, due to nonlinearity, the Euler rotation angle of the DNM necessarily deviates from 0^o. As a consequence of its unphysical linear constitutive relation, the DM has many drawbacks in numerical applications. The model coefficient (i.e., Eq. 2.16) of the DM is not bounded and admits a possible singularity when the denominator ($M_{ij}M_{ij}$) of the formulation becomes vanishingly small. The model can also lead to an over-prediction of the SGS dissipation if the model coefficient is restricted to be positive, while on the other hand, potential numerical instability due to excessive backscatter of the SGS TKE can result if the model coefficient is allowed to be negative [33]. For these reasons, plane averaging is often necessary to maintain numerical stability for flows with 2D homogeneity, which makes any direct local application of the DM difficult. On occasions when 2D homogeneity does not exist, "clipping" is often necessary to restrict the coefficient of the DM in order to stabilize a numerical simulation. Unlike the DM, the DNM self-adjusts the alignment angle between the principal axes of $-\tau_{ij}$ and $\bar{S}_{ij}$, and therefore,

dynamically calibrates the relative rotation between the two eigenframes of $-\tau_{ij}$ and $\bar{S}_{ij}$ [50]. For this reason, the DNM allows for a more realistic geometrical and physical representation of the backscatter effects. Owing to its robustness, the DNM can be applied locally without any local averaging (or, clipping) techniques in calculation of its three coefficients, which is in sharp contrast to the limited performance of the DM. This excellent natural localization performance of the DNM has been analyzed in Wang and Bergstrom [1] and further confirmed by a number of recent tests based on different types of flows [53–56, 64].

3.4.6 Energy Spectra

In Fig. 3.22, the non-dimensionalized energy spectra, $E_{u''u''} = E(f_s)\bar{U}/h$, are plotted with respect to the Strouhal number, $S_r = f_s h/\bar{U}$. Here, $E(f_s)$ is the spectra of the square of streamwise velocity fluctuations, $u''^2/\bar{U}^2$, extracted based on phase-averaging over the last four pulsatile cycles, and f_s is the time frequency of eddy motions at a specific streamwise location. The frequency spectra is computed using a fast Fourier transform (FFT) scheme. In order to demonstrate the changes in the slope of the energy spectrum, two straight lines corresponding to $(S_r)^{-5/3}$ and $(S_r)^{-10/3}$ are included in Fig. 3.22. According to Tennekes and Lumley [65], a frequency spectrum often includes three distinct subranges. The first subrange contains the energy of the injected flow at very small time frequencies (spatially, corresponding to large-scale eddy motions). The second part is the so-called inertial subrange where the energy cascade conserves across each frequency and the spectrum slope is characterized by a constant value, $-5/3$, following the well-known "Kolmogorov's $-5/3$ law" (or, "K41 theory"). Finally, the third part is the viscous dissipation subrange corresponding to high-frequency turbulent motions (spatially, corresponding to small-scale eddy motions).

In Fig. 3.22(a), it is shown that the slope of the spectrum deviates from the value $-5/3$ (characteristics of the inertial subrange). This indicates that the flow is still laminar at the center of the stenosis ($x/h = 0$). The signature of the inertial subrange

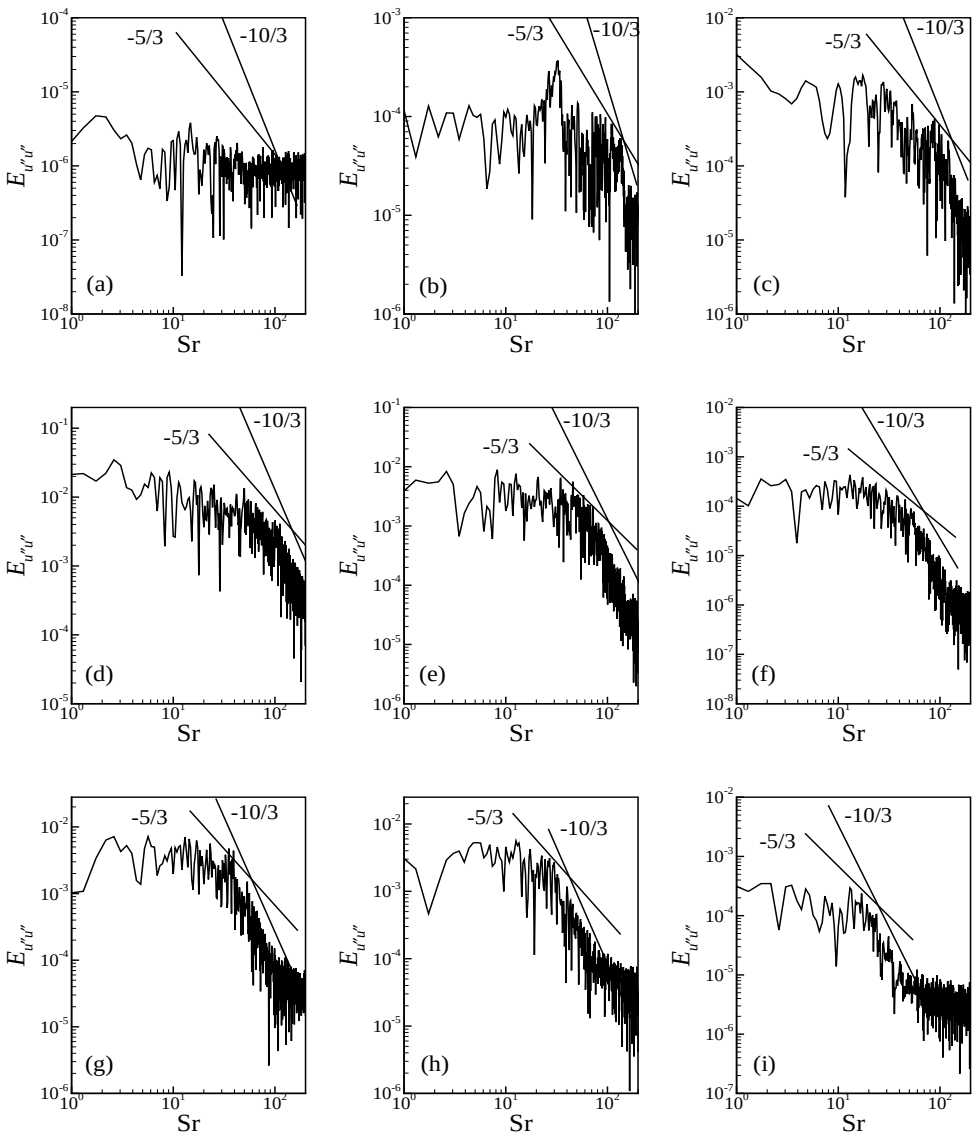

FIGURE 3.22: Non-dimensionalized energy spectrum related to the streamwise fluctuations u'', at the different streamwise locations: (a) $x/h = 0$, (b) $x/h = 1$, (c) $x/h = 2$, (d) $x/h = 3$, (e) $x/h = 4$, (f) $x/h = 5$, (g) $x/h = 6$, (h) $x/h = 8$ and (i) $x/h = 10$.

becomes evident in Figs. 3.22(b)-(f), which correspond to the fully-turbulent state in the immediate post-stenotic region ($1 \leq x/h \leq 5$). As shown in Figs. 3.22(g)-(i), in the far downstream region of the stenosis, the interval of the inertial subrange reduces as the turbulent fluctuations decrease due to the re-laminarization tendency. Furthermore, it is observed that the slope of the spectrum changes from $-5/3$ to $-10/3$ at the higher Strouhal number, which pattern is consistent with the results of

Lu *et al.* [65]. In the viscous dissipation subrange, the TKE eventually converts into thermal energy through the mechanism of molecular dissipation.

3.5 Summary

Large-eddy simulation based on an advanced dynamic nonlinear subgrid-scale model (DNM) has been applied to the study of physiological pulsatile flow through an idealized 3D model of arterial stenosis. In this chapter, attention has also been focused on examining the predictive performance of the DNM in comparison with that of the conventional DM. Owing to the narrowing of the channel, the transition of the pulsatile flow from laminar to turbulent pattern occurs immediately downstream of the stenotic location, and the flow becomes re-laminarized further downstream of this location.

In LES study, the first- and second-order flow statistics of the velocity field have been thoroughly analyzed. At the throat ($x/h = 0$) of the stenosis, the shear stress at the wall increases significantly. In contrast to the behaviour of the viscous wall shear stresses, the largest drop in the Reynolds turbulent shear stress occurs at the post-lip ($x/h = 1.0$) of the stenosis in the recirculation zone. In the immediate post-stenotic region ($1 < x/h < 5$), the flow becomes fully turbulent and the slope of the energy spectrum related to the streamwise turbulent fluctuations is $-5/3$, which is characteristic of the inertial subrange. In the far downstream region of the stenosis, it is observed that the slope of the spectrum changes from $-5/3$ to $-10/3$ at the higher Strouhal number, indicating a relative increase in viscous dissipation and an tendency towards re-laminarization.

Blood flow does not always behave as a Newtonian fluid in arteries. For this reason, any LES study of non-Newtonian flow through a stenosis based on the conventional dynamic SGS stress model of Lilly [2] may not be suitable. The constitutive relationship of the DM is based on the overly simplified linear Boussinesq assumption (Smagorinsky), and correspondingly, the SGS viscosity of the DM is a

linear function of the resolved strain rate tensor. However, the molecular viscosity of a non- Newtonian blood fluid is typically a nonlinear function of the strain rate tensor. In the next chapter, the application of the DNM to LES of non-Newtonian blood flows will be considered, which successfully resolves the current conceptual inconsistency in modelling the molecular and SGS viscosities.

Chapter 4

LES of a Pulsatile Non-Newtonian Flow in a Channel with a Single-Sided Constriction

4.1 Introduction

Pulsatile laminar-turbulent transitional non-Newtonian fluid flow in a 3D constricted channel represents a challenging topic and has many important applications in biofluids engineering. Human blood flow can be treated as a Newtonian fluid in large arteries, however, in smaller arteries and veins, it behaves typically as a non-Newtonian incompressible viscoelastic fluid [44]. According to Berger and Jou [66], if the shear rate is greater than 100 s^{-1}, the blood behaves like a Newtonian fluid and its viscosity approaches an asymptotic value, $\mu_\infty = 3.45 \times 10^{-3}$ Pa $\cdot$ s. However, if the shear rate of a blood flow falls below this threshold, its viscosity increases and non-Newtonian fluid behaviours begin to exhibit.

Furthermore, human blood flow through arteries is inherently unsteady and pulsatile due to the nature of heart pumping cycles, and the flow pattern can be laminar, turbulent or transitional depending upon the location and geometry of the blood vessel. The transition of the flow pattern in a blood vessel is often induced by sudden expansion (aneurysm) and sudden contraction (stenosis) of the cross-sectional area of a vessel, however, this physical mechanism is further complicated by unsteady

pulsations of the flow.

In the current literature, it is popular to perform LES of stenotic flows using the DM of Germano *et al.* [41] and Lilly [2]. This approach is sound for LES of Newtonian flows. However, for LES of non-Newtonian blood flows, this approach is conceptually inconsistent. This is because the constitutive relationship of the DM is based on the Boussinesq assumption, and correspondingly, the SGS viscosity of the DM is a linear function of the resolved strain rate tensor. In contrast, it is widely observed that the molecular viscosity of a non-Newtonian blood fluid is typically a nonlinear function of the strain rate tensor.

In order to conquer this conceptual inconsistency, in this research, the advanced DNM of Wang and Bergstrom [1] is implemented for LES of non-Newtonian flows. For this proposed consistent modelling approach, the Cross model [43] is used to evaluate the non-Newtonian molecular viscosity at the filtered (or, resolved) scale and the DNM is used to reflect the non-Newtonian characteristics of the SGS viscosity at the SGS (or, unresolved) scale. In order to validate the proposed consistent modelling approach, a pulsatile non-Newtonian flow confined within a 3D channel with a stenosis formed eccentrically on the upper wall is simulated. Most of the research findings presented in this chapter have been submitted for peer referred journal publication in the format of a co-authored full-length article [67].

4.2 Test Case

Figure 4.1 shows the geometry of the computational domain and coordinate system of the stenotic channel. The model of the stenosis for this case is formed with the same equation (Eq. 3.1) as used in the chapter 3. The stenosis is formed on the upper wall. In the present study, f_c is fixed to 1/2, which results in a 50% reduction of the cross-sectional area at the center of the stenosis.

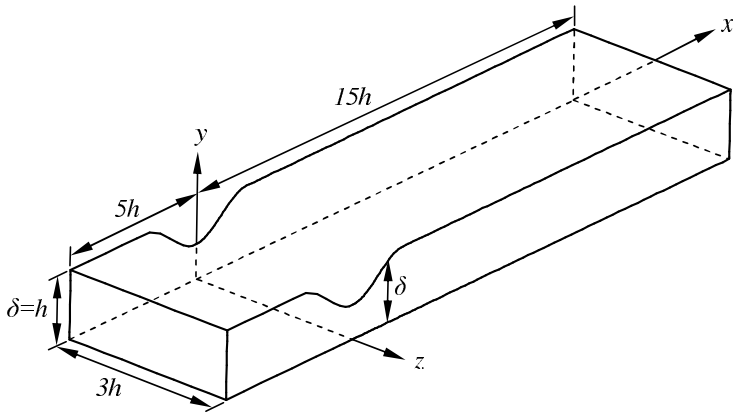

FIGURE 4.1: Computational domain and coordinate system of the stenotic channel.

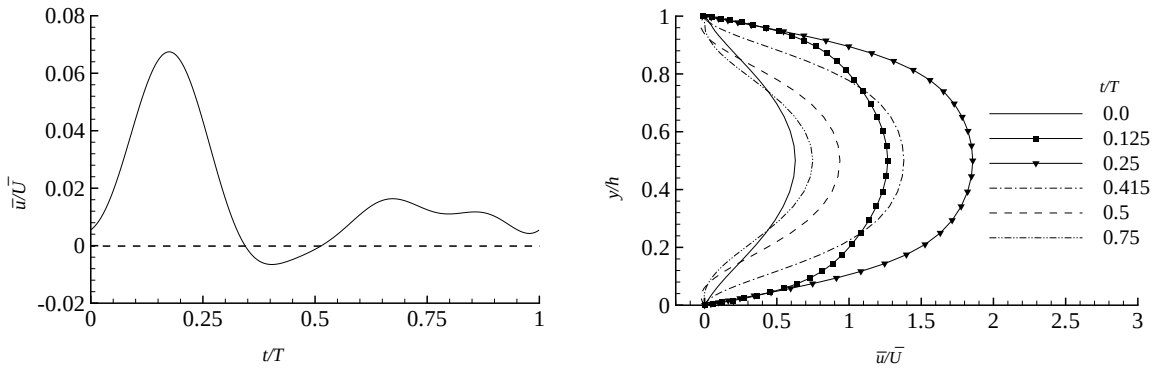

(a) (b)

FIGURE 4.2: Instantaneous inlet velocity profile, $\bar{u}/\bar{U}$, for $Re = 1200$ and $\alpha = 10.5$: (a) time history near the wall ($x/h = -5$, $y/h = 0.0057$ and $z/h = 1.5$), and (b) at the different time phases ($x/h = -5$ and $z/h = 1.5$).

4.3 Inflow Boundary Condition

The real part of the solution (Eq. B.34) is used as an inlet boundary condition to generate the pulsatile flow. Full solution procedure is explained in Appendix B. The inlet pulsatile velocity profile, derived from Eq. B.34, is demonstrated in Fig. 4.2 for $Re = 1200$. The time history of the velocity field during a full pulsation cycle at a specific near-wall location ($x/h = -5$, $y/h = 0.0057$ and $z/h = 1.5$), is shown in Fig.4.2(a). The temporal variation of the vertical profile of the streamwise velocity component across the center of the inlet plane at different phases over a pulsation cycle is shown in Fig. 4.2(b).

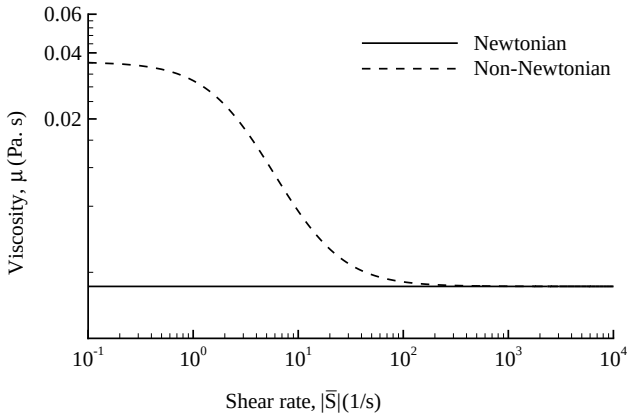

FIGURE 4.3: Relationship between the shear rate and the apparent viscosity for Newtonian and non-Newtonian fluids.

4.4 The Cross Model for the Molecular Viscosity

In Eq. 2.15, $\mu = \mu(|\bar{S}|)$ represents the molecular viscosity for a non-Newtonian fluid. The value of μ is a function of the norm of the resolved strain rate tensor $|\bar{S}|$ (also referred to as the shear rate). In a Newtonian model for the blood viscosity, the value of μ is treated as a constant, usually set to $\mu_\infty = 3.45 \times 10^{-3}$ Pa $\cdot$ s. However, for non-Newtonian fluid behaviour, Cross [43] proposed a shear rate dependent viscosity model (which is often referred to as the Cross model). The Cross model assumes the following functional relationship between the molecular viscosity and the shear rate:

$$\mu = \mu_\infty + (\mu_0 - \mu_\infty)\left[1 + \left(\frac{|\bar{S}|}{\bar{S}_c}\right)^m\right]^{-1} \tag{4.1}$$

where $\mu_0 = 0.0364$ Pa $\cdot$ s is the usual molecular blood viscosity at very low shear rates, $\bar{S}_c = 2.63\text{s}^{-1}$ is the reference shear rate and $m = 1.45$ is the model constant.

Figure 4.3 demonstrates the functional relationship between the shear rate and the apparent blood viscosity of the Cross model. In this research, we use exclusively the Cross model for calculating the molecular viscosity of the non-Newtonian fluid at the resolved scale.

4.5 Dynamic Nonlinear SGS Stress Model (DNM)

In the current literature, LES of non-Newtonian flows has been conducted usually based on a combination of an advanced nonlinear model (e.g., the Cross model) for evaluating the molecular shear stresses at the resolved scale and the DM for modelling the SGS shear stresses (at the unresolved scale). As such, an inconsistence appears: the molecular viscosity associated with the molecular shear stresses is a nonlinear function of $|\bar{S}|$, however, the SGS viscosity associated with the SGS shear stresses is a linear function of $|\bar{S}|$.

In order to avoid this conceptual inconsistency, the DNM is considered in this research. Given its complex constitutive equation (Eq. 2.18), the DNM models the SGS shear stresses as a nonlinear function of the strain rate tensor. The idea of using an explicit nonlinear tensorial polynomial constitutive relation to connect the velocity gradient tensor to the unknown stress tensor to be modeled for a non-Newtonian fluid was originally proposed by Rivlin [68]. Following the pioneering work of Rivlin [68], the theory for developing constitutive relations for modelling turbulent stresses in non-Newtonian fluids has been systematically addressed in Spencer [69]. There are many nonlinear models potentially available for calculating the molecular and SGS shear stresses. In this study, as a first attempt to resolve the current inconsistence in shear stress modelling for LES, we focus our attention on the combination of the Cross model and the DNM only.

4.6 Results and Discussions

The results presented in this section are based on Reynolds number $Re = 1200$. In order to examine the effects of grid resolution on the predicted results, two different grid systems with $150 \times 60 \times 50$ (Case 1) and $240 \times 90 \times 50$ (Case 2) control volumes (in the stream, vertical and spanwise directions, respectively) have been compared in the numerical simulations. Both grid systems are body-fitted reflecting the curvilinear

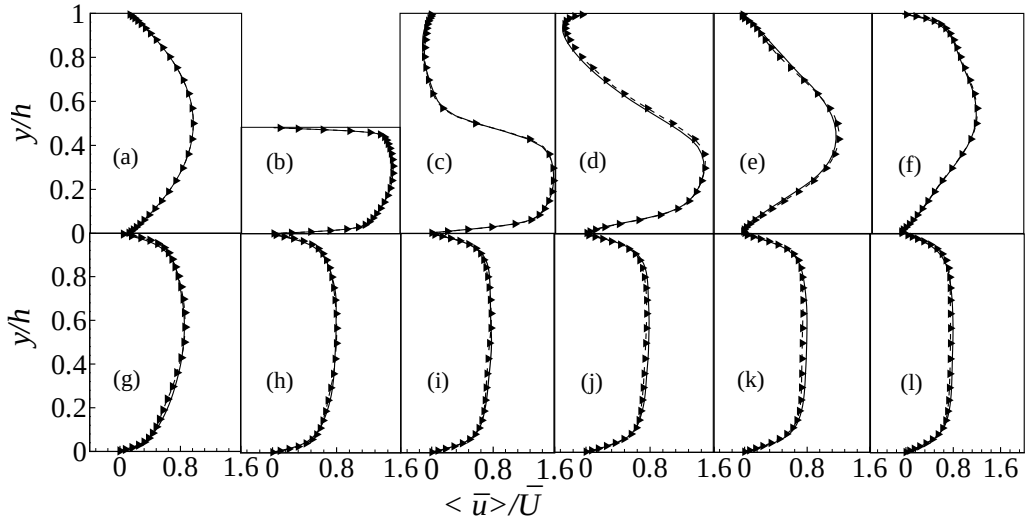

FIGURE 4.4: Grid sensitivity test with respect to the mean streamwise velocity, $\langle \bar{u} \rangle / \bar{U}$, at (a) $x/h = -5$, (b) $x/h = 0$, (c) $x/h = 1$, (d) $x/h = 2$, (e) $x/h = 3$, (f) $x/h = 4$, (g) $x/h = 5$, (h) $x/h = 6$, (i) $x/h = 8$, (j) $x/h = 10$, (k) $x/h = 12$ and (l) $x/h = 15$. Based on two grid systems, Case 1: solid line for $150 \times 60 \times 50$ control volumes, Case 2: dashed line with symbol for $240 \times 90 \times 50$ control volumes.

geometry of the computational domain. Furthermore, from Case 1 to 2, the number of grid points along the streamwise direction (N_x) is significantly increased in order to improve the predictive accuracy of the small-scale turbulent eddy motions within the post-stenotic regime. The number of streamwise grid points upstream of the stenosis is always fixed at 30 while the rest of the grid points are distributed within and downstream of the stenosis. The grid is uniform in the spanwise direction and significantly refined in the near-wall region in order to accurately resolve the wall shear stress. The results of Cases 1 and 2 are compared in Figs. 4.4 and 4.5 in terms of the non-dimensionalized time-averaged streamwise velocity (i.e., $\langle \bar{u} \rangle / \bar{U}$) and resolved TKE (i.e., $k/\bar{U}^2$) respectively, at different locations along the streamwise direction. Here, the resolved TKE is defined as $k = \frac{1}{2}\langle u_j'' u_j'' \rangle$, $u_j'' = \bar{u}_j - \langle \bar{u}_j \rangle_{sp}$ represents the resolved residual velocity component relative to $\bar{u}_j$, and $\langle \bar{u}_j \rangle_{sp}$ is the spanwise- and phase-averaged velocity.

The flow statistics were calculated based on 10 pulsatile cycles, and for each pulsatile cycle, 6284 time steps are computed. As usual, the computational cost and data storage need are very demanding when phase averaging is involved. From

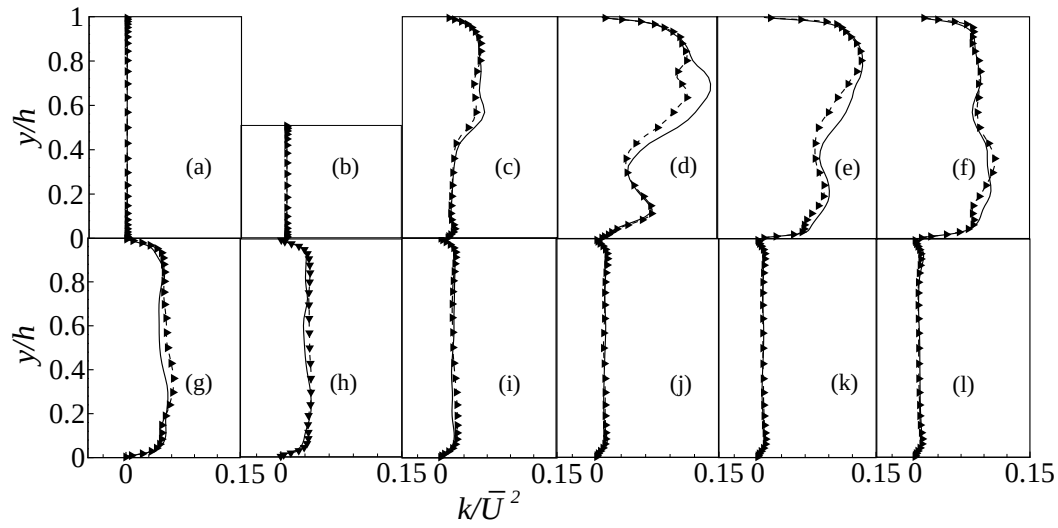

FIGURE 4.5: Grid sensitivity test with respect to TKE, $k/\bar{U}^2$, at (a) $x/h = -5$, (b) $x/h = 0$, (c) $x/h = 1$, (d) $x/h = 2$, (e) $x/h = 3$, (f) $x/h = 4$, (g) $x/h = 5$, (h) $x/h = 6$, (i) $x/h = 8$, (j) $x/h = 10$, (k) $x/h = 12$ and (l) $x/h = 15$. Based on two grid systems, Case 1: solid line for $150 \times 60 \times 50$ control volumes, Case 2: dashed line with symbol for $240 \times 90 \times 50$ control volumes.

Fig. 4.4, it is seen that both grid configurations used in the present computations (Cases 1 and 2) are sufficient to resolve the mean velocity field. However, Fig. 4.5 shows that the results of the non-dimensionalized TKE at the immediate post-stenotic region (Figs. 4.5(c)-(g)), changes slightly with the grid resolution. A total grid independence of the computed turbulent fluctuations is not expected since only the resolved-scale flow motions are directly computed in LES. However, it has been shown in this study (cf. Fig. 4.4) and in many previous works that the first-order flow statistics (e.g., the filtered velocities) are not sensitive to grid resolution. Based on the above observations, without a special declaration, the numerical results presented in the remainder of the chapter are based on $150 \times 60 \times 50$ control volumes (Case 1).

Figures 4.6(a) and (b) shows the streamwise distribution of instantaneous and averaged DNM coefficients, respectively. From both figures, it is clear that from the inlet to the throat of the stenosis (i.e., $-5 < x/h < 0$), the viscous forces are dominant and the flow pattern is primarily laminar. Therefore, all three DNM coefficients are very close to zero. Immediately downstream of the centre of the stenosis, the DNM is fully activated and its coefficients reach their maximum values within $0 < x/h < 1$ and

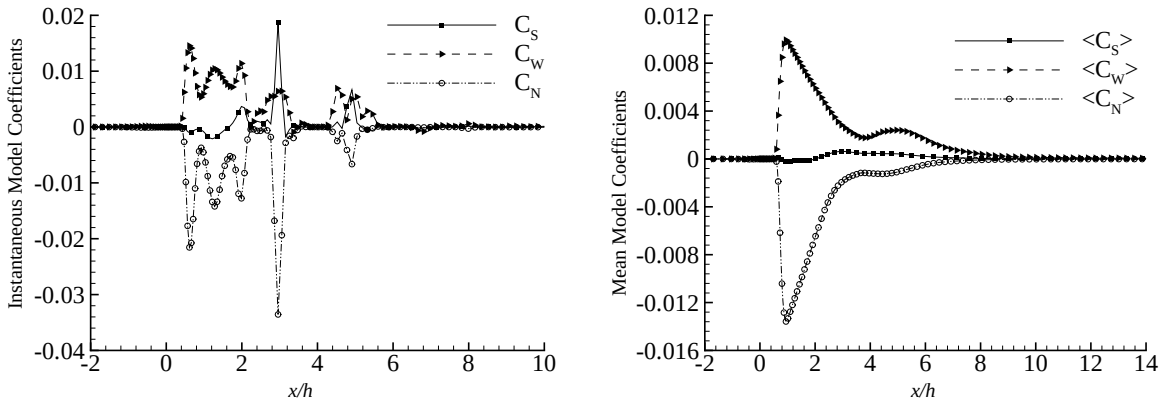

(a) (b)

FIGURE 4.6: Model coefficients for the DNM, (a) instantaneous coefficients C_S, C_W and C_N along the central streamline of the domain ($y/\delta = 0.5$, $z/h = 1.5$), and (b) time- and spanwise-averaged coefficients $\langle C_S \rangle$, $\langle C_W \rangle$ and $\langle C_N \rangle$ at $y/h = 0.5$.

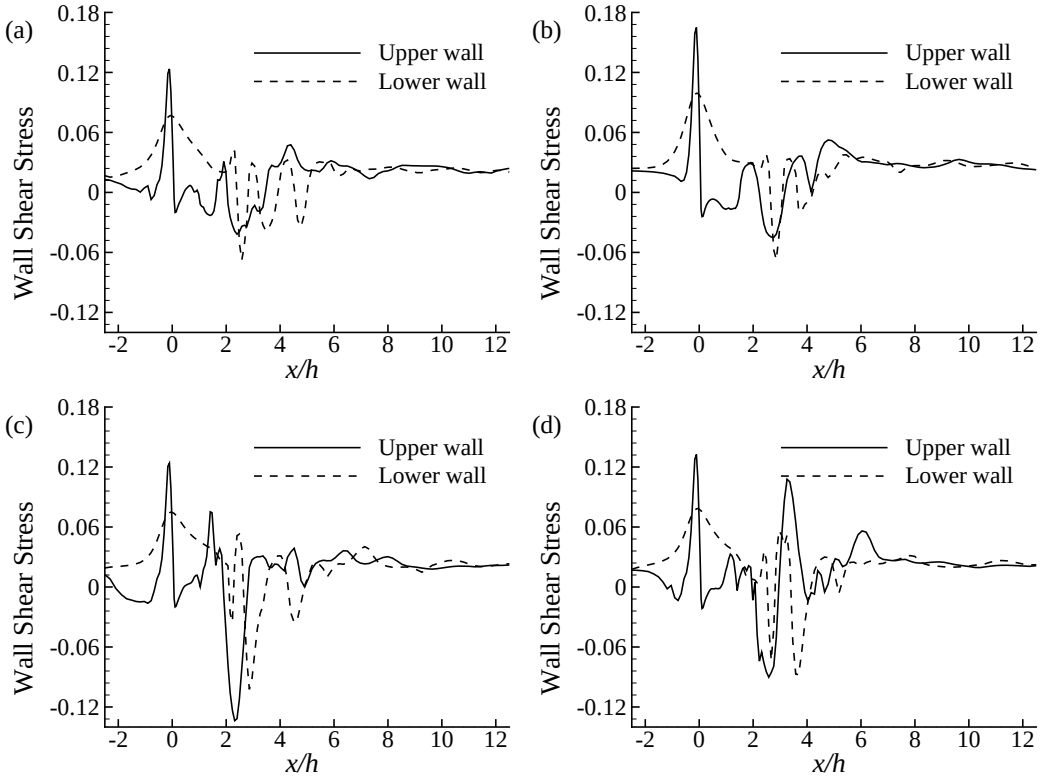

FIGURE 4.7: Non-dimensionalized instantaneous wall shear stress, $\tau_w/\frac{1}{2}\rho\bar{U}^2$, at (a) $t/T = 0$, (b) $t/T = 0.25$, (c) $t/T = 0.5$ and (d) $t/T = 0.75$.

then gradually decrease to zero further downstream of the stenosis. The inherent self-calibration mechanism of the DNM coefficients is very responsive to the varying SGS

stress level characteristic of a laminar-turbulent-laminar transitional flow through a modeled arterial stenosis. The distribution of the DNM coefficients is anisotropic in the streamwise direction due to the presence of the stenosis. In the core turbulent region (i.e., $0.5 < x/h < 7$), the mean value is positive for $\langle C_S \rangle$ and $\langle C_W \rangle$ but negative for $\langle C_N \rangle$. Similar behaviour was reported by Wang and Bergstrom [1] in their study of a fully-developed turbulent channel flow.

In Fig. 4.7, the instantaneous wall shear stress $\tau_w \stackrel{\text{def}}{=} \mu \frac{\partial \bar{u}}{\partial y}|_w$ (non-dimensionalized using $\frac{1}{2}\rho \bar{U}^2$)is presented at four different phases of the 9th pulsation cycle (with a temporal period T). As shown in Fig. 4.7(a), at the initial phase ($t/T = 0$) of the 9th pulsation cycle, the acute shear stress peaks at the upper wall just before the centre of the stenosis and the oscillatory behaviour of the wall shear stress extends to the post-stenotic region. Figure 4.7(b) shows that at $t/T = 0.25$, the instantaneous wall shear stress at the upper wall attains its maximum positive value over the entire pulsation cycle. We should recall that at this phase of the pulsation cycle, the inlet velocity also reaches its maximum value (see Fig. 4.2). Immediately downstream of the stenosis, the shear stress becomes negative which is consistent with the flow pattern in the large recirculation zone. As seen in Fig. 4.7(c), the wall shear stress at the upper wall decreases at $t/T = 0.5$ to attain its minimum (maximum negative) value over the entire pulsation cycle in the post-stenotic region (approximately at $x/h = 2.3$). However, as shown in Fig. 4.7(d), at $t/T = 0.75$, the sharp wall stress drop at $x/h = 2.3$ is recovered and the profile of the wall stress tends to evolve back to the original one corresponding to the initial phase (corresponding to Fig. 4.7(a) for $t/T = 0$) to complete a full pulsation cycle. Through the entire pulsation cycle, the wall shear stress level at the lower wall is generally lower than that at the upper wall where the stenosis is located.

The time- and spanwise-averaged wall pressure is shown in Fig. 4.8(a). Owing to the constriction of the channel, the pressure drops significantly at both the upper and lower walls. Furthermore, the pressure drop is much sharper at the upper wall than at the lower wall owing to the fact that the cosine-shaped stenosis is located at the upper wall. At both the upper and lower walls, the maximum pressure drop

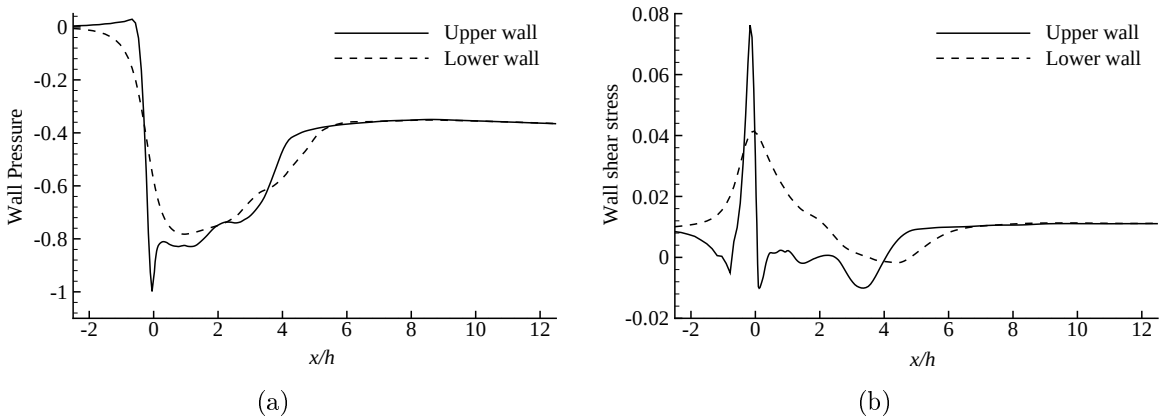

(a) (b)

FIGURE 4.8: Non-dimensionalized time- and spanwise-averaged profile of (a) the wall pressure, $\langle \bar{p} \rangle / \frac{1}{2}\rho \bar{U}^2$, and (b) the wall shear stress, $\langle \tau_w \rangle / \frac{1}{2}\rho \bar{U}^2$.

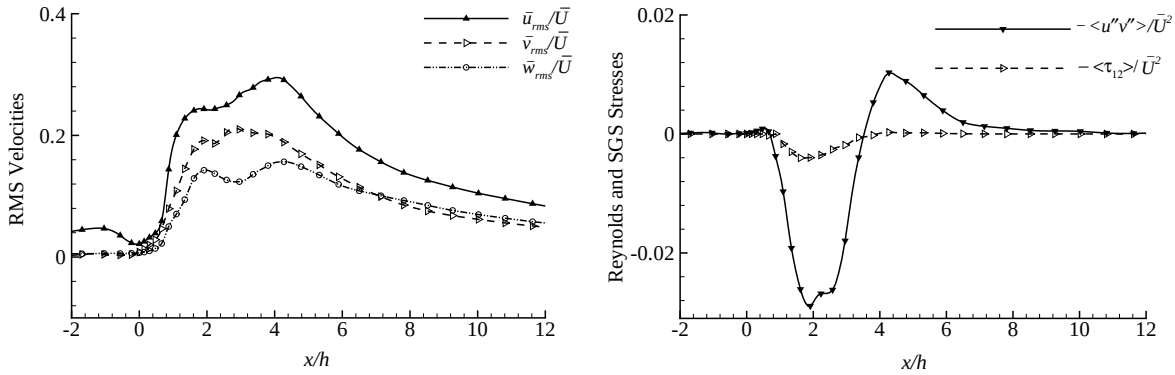

(a) (b)

FIGURE 4.9: Non-dimensionalized profiles for (a) the RMS velocities $\bar{u}_{rms}/\bar{U}$, $\bar{v}_{rms}/\bar{U}$ and $\bar{w}_{rms}/\bar{U}$, and (b) the resolved Reynolds stress $-\langle u''v'' \rangle/\bar{U}^2$ and SGS stress $-\langle \tau_{12} \rangle/\bar{U}^2$ at $y/\delta = 0.5$.

occurs within the immediate post-stenotic region for $0 < x/h < 3$, where an adverse pressure gradient presents due to the existence of the stenosis and flow recirculation. The signature of the flow recirculation pattern is also evident in Figs. 4.4(c)-(e), which show that the mean velocity is negative in upper-wall region immediately after the stenosis. The time- and spanwise-averaged wall shear stress is shown in Fig. 4.8(b). Consistent with the instantaneous streamwise profiles shown in Figs. 4.7(a)-(d), the maximum mean wall shear stress also occurs within the stenosis immediately upstream of its throat location ($x/h = 0$). Figure 4.9(a) shows non-dimensionalized profiles of the root mean square (RMS) velocities, $\bar{u}_{rms} \overset{\text{def}}{=} \langle u''^2 \rangle^{1/2}$, $\bar{v}_{rms}$ and $\bar{w}_{rms}$

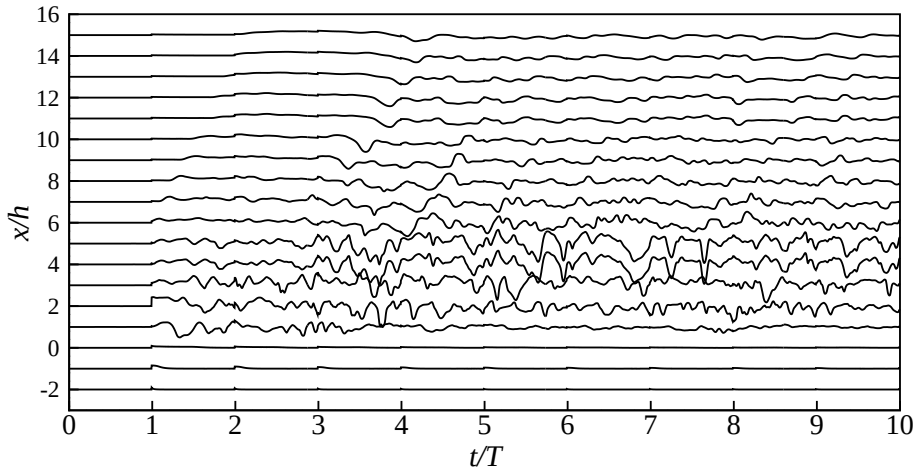

FIGURE 4.10: Time history of the streamwise velocity fluctuations, u''/u''_{max}, based on phase averaging over the last three pulsation cycles, along the central streamline ($y/\delta = 0.5$ and $z/h = 1.5$) for $Re = 1200$.

(defined similarly) along the central streamline of the domain ($y/\delta = 0.5$). As shown in Fig. 4.9(a), the value of $\bar{u}_{rms}/\bar{U}$ is small and the values of $\bar{v}_{rms}/\bar{U}$ and $\bar{w}_{rms}/\bar{U}$ are very close to zero at the inlet reflecting the nature of the laminar pulsatile flow pattern in the upstream region (see Fig. 4.5). However, after the centre of the stenosis, the RMS values of the velocities begin to increase and become prominent in the immediate post-stenotic region ($0 < x/h < 6$). Far downstream of the stenosis ($x/h > 6$), the flow is still turbulent but the intensity decreases gradually. Based on the above analysis, turbulent fluctuations are highly dependent on the presence of the stenosis. The distribution of the non-dimensionalized resolved Reynolds stress, $-\langle u''v''\rangle/\bar{U}^2$ and the SGS stress, $-\langle \tau_{12}\rangle/\bar{U}^2$, along the central streamline of the domain, are shown in Fig. 4.9(b). Because the flow pattern is primarily laminar upstream of the stenosis, the Reynolds stress $-\langle u''v''\rangle/\bar{U}^2$, and the SGS stress $-\langle \tau_{12}\rangle/\bar{U}^2$, are vanishingly small in this region. For both the resolved and SGS stresses, there is a stress drop within the region $0.58 < x/h < 3$. Once $x/h > 3$, the resolved Reynolds stress begin to increase until $x/h = 4.4$ and then eventually approaches to zero due to the relaminarization.

Figure 4.10 displays the time history of the streamwise velocity fluctuations, u''/u''_{max} (non-dimensionalized by its maximum value u''_{max}) obtained using phase-averaging over the last three pulsatile cycles at different streamwise locations along

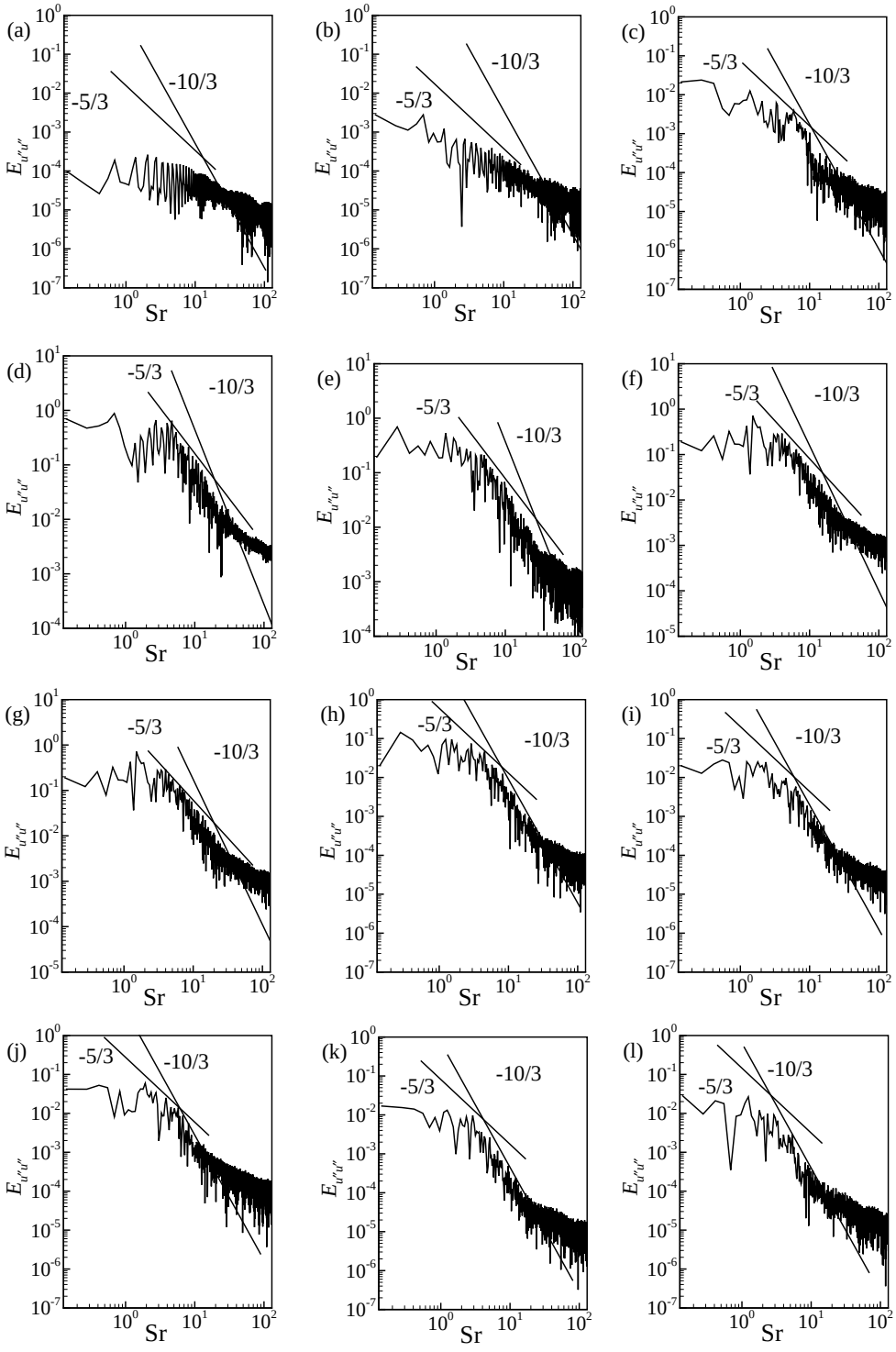

FIGURE 4.11: Non-dimensionalized energy spectrum related to the streamwise fluctuations u'', at the different streamwise locations: (a) $x/h = -2$, (b) $x/h = 0$, (c) $x/h = 1$, (d) $x/h = 2$, (e) $x/h = 3$, (f) $x/h = 4$, (g) $x/h = 5$, (h) $x/h = 6$, (i) $x/h = 8$, (j) $x/h = 10$, (k) $x/h = 12$ and (l) $x/h = 14$.

the central streamline of the domain ($y/\delta = 0.5$ and $z/h = 1.5$) for $Re = 1200$. The flat profile associated with the negligible magnitude of the fluctuating component both at the upstream and center of the stenosis (for $x/h = -2, -1$ and 0) indicates that the flow is laminar prior to the throat of the stenosis. Meanwhile, turbulence is triggered as soon as the flow passes through the stenosis and the flow fluctuations are the strongest in the immediate post-stenotic region $1 \leq x/h \leq 6$. Further downstream of the stenosis (for $x/h > 6$), turbulence gradually vanishes as the magnitude of the velocity fluctuation gradually decreases, indicating a relaminarization process in the flow.

In order to clearly demonstrate the random turbulent fluctuations of the velocity field, it is useful to calculate the non-dimensionalized energy spectra, $E_{u''u''} = E(f_s)\bar{U}/h$ of the square of streamwise velocity fluctuations, $u''^2/\bar{U}^2$. The non-dimensionalized energy spectra is plotted against the Strouhal number, $S_r = f_s h/\bar{U}$ in Fig. 4.11. Figures 4.11(a)-(b) show that the slope of the spectrum deviates from the value $-5/3$ (characteristic of the inertial subrange) both at the pre-stenosis ($x/h = -2$) and the center of the stenosis ($x/h = 0$). This deviation is due to the fact that although the flow is subjected to pulsations, the flow pattern is primarily laminar in the region upstream of the stenosis. This feature of the spectrum slope extends to the center of the slope ($x/h = 0$), where the flow is still laminar and the onset of turbulence is just triggered due to the constriction of the channel. It is also evident from Figs. 13(c)-(g) that the inertial subrange exists in the immediate post-stenotic region ($1 \leq x/h \leq 5$), where the flow is fully turbulent. Figures 4.11(h)-(l) indicate that as the distance from the stenosis increases in the far downstream region ($6 \leq x/h \leq 14$), the inertial subrange becomes shorter and shorter, as the turbulent fluctuations decrease due to the relaminarization tendency. Furthermore, it is observed that the slope of the spectrum changes from $-5/3$ to $-10/3$ at the higher Strouhal number, which pattern is consistent with that of the pulsatile Newtonian flow discussed in chapter 3. In the viscous dissipation subrange, the TKE eventually converts into thermal energy through the mechanisms of molecular dissipation and acoustic fluctuations.

4.7 Summary

In the current literature for LES of non-Newtonian flows (such as blood flows), it is popular to use the conventional DM of Germano *et al.* [41] and Lilly [2] for evaluating the SGS stresses. This approach, however, inevitably results in a conceptual inconsistency in the modelling of molecular and SGS viscosities. In the conventional models for the molecular viscosity of a non-Newtonian fluid (e.g., the Cross model), the molecular viscosity μ is usually modeled as a nonlinear function of the shear rate $|\bar{S}|$; in contrast, the overly simplified constitutive relation of the DM (based on the linear Boussinesq assumption) defines the SGS viscosity as a linear function of $|\bar{S}|$. This research aims at resolving this conceptual inconsistence in the viscosity modelling for LES of non-Newtonian flows. The proposed modelling approach utilizes the Cross model for modelling the molecular viscosity and the DNM of Wang and Bergstrom [1] for modelling the SGS stress tensor, so that both the molecular and SGS shear stresses can be represented as nonlinear functions of the strain rate tensor.

The proposed modelling approach is applied to the simulation of a pulsatile laminar-turbulent-laminar transitional non-Newtonian flow through a channel with a one-sided cosine-shape stenosis at the upper wall. The transition-to-turbulence of the flow is directly triggered by the stenosis, which however, is further complicated by the pulsatile inertial forces and the mean driving inertial forces. Both the pulsatile inertial forces and the mean driving inertial forces tend to enhance turbulence and flow unsteadiness, and the effects of these two types of forces in comparison with the viscous forces (which tend to suppress turbulence) can be quantified using the Womersley number and Reynolds number, respectively. In this research, a high Womersley number ($\alpha = 10.5$) and a low Reynolds numbers ($Re = 1200$) were tested, which are characteristics of blood flows in large arteries of humans and animals.

In the current simulations, it is confirmed that the DNM is a flexible self-calibration model which ensures local stability in the context of a pulsatile laminar-turbulent-laminar transitional flow. The first- and second-order flow statistics of the

velocity field have been thoroughly analyzed. In the region upstream of the stenosis, the viscous forces are dominant and the flow pattern is primarily laminar. Therefore, the resolved Reynolds stress, turbulent intensities, wall shear stress, and SGS shear stresses as well as the three coefficients of DNM are very close to zero. In general, the magnitude of these quantities increases significantly at the throat location of the stenosis and in the immediate post-stenotic region (for $0 < x/h < 3$, where the pressure of the flow drops significantly and flow recirculates due to the presence of an adverse streamwise pressure gradient). In the region far downstream of the stenosis, the flow is relaminarized and the value of these quantities again becomes vanishingly small.

Chapter 5

Conclusions and Future Work

The physics of the physiological pulsatile flows under investigation are dominated by four major factors, the pulsatile inertial forces (as a consequence of the pulsatile inlet boundary condition), mean driving inertial forces (associated with the mean pressure gradient in the streamwise direction), viscous forces of the fluid, and the geometry of the stenosis. Owing to the narrowing of the channel, the transition of the pulsatile flow from laminar to turbulent pattern occurs immediately downstream of the stenosis, and the flow becomes relaminarized in the far downstream region of the stenosis. The transition-to-turbulence of the flow is directly triggered by the stenosis, which however, is further complicated by the pulsatile inertial forces and the mean driving inertial forces. Both the pulsatile inertial forces and the mean driving inertial forces tend to enhance turbulence and flow unsteadiness, and the effects of these two types of forces in comparison with the viscous forces (which tend to suppress turbulence) can be quantified using the Womersley number and Reynolds number, respectively. For the Newtonian fluids, a high Womersley number ($\alpha = 10.5$) and three low Reynolds numbers ($Re = 750$, 1200 and 1800) were tested; and for the non-Newtonian fluids, the Womersley number remained unchanged, however, the Reynolds number was fixed to 1200. All these values are characteristics of blood flows in large arteries of humans and animals.

In chapter 3, we have examined the predictive performance of the DNM in comparison with that of the conventional DM in the context of Newtonian fluids in a double-sided constrained channel. It is confirmed that the DNM is a good

performance model in terms of self-calibration, as it ensures local stability (without using any local spatial averaging or any clipping technique to restrict the magnitude of the three dynamic coefficients) in the current simulation of a physiological pulsatile laminar-turbulent-laminar stenotic flow. In contrast, when the DM was applied to the simulation, a clipping technique was needed to restrict the model coefficient in order to maintain numerical stability. This advanced DNM allows for physical representation of both forward and backward scattering of local TKE between the filtered and subgrid scales. In contrast, owing to its overly simplified constitutive relationship (Boussinesq), the DM assumes that the principal directions (eigenvectors) of the negative of the SGS stress tensor $-\tau_{ij}$ be strictly aligned with those of the resolved strain rate tensor $\bar{S}_{ij}$. In consequence, the DM fails to predict backscatter of the mean SGS KE production rate (which quantity is determined uniquely by the tensorial geometrical relationship between the $-\tau_{ij}$ and $\bar{S}_{ij}$ [56]).

In chapter 4, a consistent modelling approach has been proposed to perform LES of non-Newtonian flow by implementing the DNM of Wang and Bergstrom [1] into the simulations. The proposed modelling approach resolves the previous conceptual inconsistency in modelling the molecular and SGS shear stresses, as it warrants that both the molecular and SGS viscosities are nonlinear functions of the resolved strain rate tensor. It was also confirmed that the DNM is a good-performance self-calibration model which ensures local stability in the physiological pulsatile laminar-turbulent-laminar flow studied. This advanced dynamic nonlinear SGS model allows for physical representation of both forward and backward scattering of local turbulent energy fluxes between the filtered and subgrid scales of motions. Although the preliminary results based on the proposed consistent modelling approach for molecular and SGS shear stresses are encouraging, additional studies are necessary in the future to further prove that it is an effective numerical tool for LES of non-Newtonian flows.

In practice, there are many challenges involved in numerical modelling of blood flows. The geometry of a stenosis in a blood vessel can be highly irregular and the boundary material can be nonlinear and elastic, complex physiological conditions can be involved, and the behaviour of the blood fluid itself can be Newtonian in large

arteries and non-Newtonian in small arteries. Furthermore, even the deterministic mechanical research methodology represented by this study and those of Clark [7], Ghalichi *et al.* [17], Lee *et al.* [18, 19], Mittal *et al.* [4, 31] and Varghese *et al.* [27, 28] has certain limitations. For these reasons, the conclusions obtained from this research cannot be directly used for any clinical purposes. However, it is believed that the current flows under study can serve cleaner bench test cases for profound understanding of the basic underlying physics of these types of pulsatile stenotic transition flows, which are of fundamental interest to both the mechanical and biological communities.

It is confirmed through this research that the LES is a useful tool for numerical investigation of transitional Newtonian and non-Newtonian flows in stenotic channel. As the first step, a rectangular cross-section has been used in the simulations. In the future, more realistic biological vessels (with different cross-sectional shapes) need to be considered.

References

[1] B.-C. Wang and D. J. Bergstrom, "A dynamic nonlinear subgrid-scale stress model," *Phys. Fluids*, vol. 17 (3), pp. 1–15, 2005.

[2] D. K. Lilly, "A proposed modification of the Germano subgrid-scale closure method," *Phys. Fluids A*, vol. 4, pp. 633–635, 1992.

[3] S. A. Ahmed and D. P. Giddens, "Velocity measurements in steady flow through axisymmetric stenoses at moderate Reynolds numbers," *J. Biomech.*, vol. 16 (7), pp. 505–516, 1983.

[4] R. Mittal, S. P. Simmons, and H. S. Udaykumar, "Application of large-eddy simulation to the study of pulsatile flow in a modeled arterial stenosis," *ASME J. Biomech. Eng.*, vol. 123, pp. 325–331, 2001.

[5] D. N. Ku, "Blood flows in arteries," *Annu. Rev. Fluid Mech.*, vol. 29, pp. 399–434, 1997.

[6] M. S. Bloor, "The transition to turbulence in the wake of a circular cylinder," *J. Fluid Mech.*, vol. 19, pp. 290–304, 1964.

[7] C. Clark, "The fluid mechanics of aortic stenosis - I. Theory and steady flow experiments," *J. Biomech.*, vol. 9 (8), pp. 521–528, 1976.

[8] C. Clark, "The fluid mechanics of aortic stenosis - II. Unsteady flow experiments," *J. Biomech.*, vol. 9 (6), pp. 569–573, 1976.

[9] R. A. Cassanova and D. P. Giddens, "Disorder distal to modeled stenoses in steady and pulsatile flow," *J. Biomech.*, vol. 11 (10-12), pp. 441–453, 1978.

[10] D. F. Young and F. Y. Tsai, "Flow characteristics in models of arterial stenoses - I. Steady flow," *J. Biomech.*, vol. 6 (4), pp. 403–410, 1973.

[11] D. F. Young and F. Y. Tsai, "Flow characteristics in models of arterial stenoses - II. Unsteady flow," *J. Biomech.*, vol. 6 (5), pp. 547–559, 1973.

[12] W. Yongchareon and D. F. Young, "Initiation of turbulence in models of arterial stenoses," *J. Biomech.*, vol. 12 (3), pp. 185–196, 1979.

[13] S. A. Ahmed and D. P. Giddens, "Flow disturbance measurements through a constricted tube at moderate Reynolds numbers," *J. Biomech.*, vol. 16 (12), pp. 955–963, 1983.

[14] S. A. Ahmed and D. P. Giddens, "Pulsatile poststenotic flow studies with laser Doppler anemometry," *J. Biomech.*, vol. 17 (5), pp. 695–705, 1984.

[15] S. A. Ahmed, "An experimental investigation of pulsatile flow through a smooth constriction," *Exp. Therm. Fluid Sci.*, vol. 17 (4), pp. 309–318, 1998.

[16] F. P. Tan, G. Soloperto, N. B. Wood, S. Thom, and X. Y. Xu, "Analysis of flow disturbance in a stenosed carotid artery bifurcation using two-equation transitional and turbulence models," *ASME J. Biomech. Eng.*, vol. 130 (6), pp. 1–12, 2008.

[17] F. Ghalichi, X. Deng, A. D. Champlain, Y. Douville, M. King, and R. Guidoin, "Low Reynolds number turbulence modeling of blood flow in arterial stenosis," *Biorheology*, vol. 35 (4-5), pp. 281–294, 1998.

[18] T. S. Lee, W. Liao, and H. T. Low, "Numerical simulation of turbulent flow through series stenoses," *Int. J. Numer. Meth. Fluids*, vol. 42 (7), pp. 717–740, 2003.

[19] T. S. Lee, W. Liao, and H. T. Low, "Numerical study of physiological turbulent flows through series arterial stenosis," *Int. J. Numer. Meth. Fluids*, vol. 46 (3), pp. 315–344, 2004.

[20] J. Ryval, A. G. Straatman, and D. A. Steinman, "Two-equation turbulence modeling of pulsatile flow in a stenosed tube," *ASME J. Biomech. Eng.*, vol. 126 (5), pp. 625–635, 2004.

[21] M. C. Paul and A. Larman, "Investigation of spiral blood flow in a model of arterial stenosis," *Med. Eng. Phys.*, vol. 31 (9), pp. 1195–1203, 2009.

[22] P. G. Suffiman and D. C. Wilcox, "Turbulence-model predictions for turbulent boundary layers," *AIAA J.*, vol. 12, pp. 541–546, 1974.

[23] D. C. Wilcox, Turbulence modeling for CFD. DCW Industries, 1998.

[24] A. Scotti and U. Piomelli, "Turbulence models in pulsatile flow," *AIAA J.*, vol. 40 (3), pp. 537–544, 2002.

[25] S. J. Sherwin and H. M. Blackburn, "Three-dimensional instabilities and transition of steady and pulsatile axisymmetric stenotic flows," *J. Fluid Mech.*, vol. 533, pp. 297–327, 2005.

[26] H. M. Blackburn and S. J. Sherwin, "Instability modes and transition of pulsatile stenotic flow: pulse-period dependence," *J. Fluid Mech.*, vol. 573, pp. 57–88, 2007.

[27] S. S. Varghese, S. H. Frankel, and P. F. Fisher, "Direct numerical simulation of stenotic flows: Part 1. Steady flow," *J. Fluid Mech.*, vol. 582, pp. 253–280, 2007.

[28] S. S. Varghese, S. H. Frankel, and P. F. Fisher, "Direct numerical simulation of stenotic flows: Part 2. Pulsatile flow," *J. Fluid Mech.*, vol. 582, pp. 281–318, 2007.

[29] S. S. Varghese, Frankel, S. H., and P. F. Fisher, "Modeling transition to turbulence in eccentric stenotic flows," *ASME J. Biomech. Eng.*, vol. 130 (1), p. 014503, 2008.

[30] K. Bhaganagar, "Direct numerical simulation of flow in stenotic channel to understand the effect of stenotic morphology on turbulence," *J. Turbul.*, vol. 10, pp. 1–16, 2009.

[31] R. Mittal, S. P. Simmons, and F. Najjar, "Numerical study of pulsatile flow in a constricted channel," *J. Fluid Mech.*, vol. 485, pp. 337–378, 2003.

[32] M. C. Paul, M. M. Molla, and G. Roditi, "Large-Eddy simulation of pulsatile blood flow," *Med. Eng. Phys.*, vol. 31 (1), pp. 153–159, 2009.

[33] U. Piomelli and J. Liu, "Large-eddy simulation of rotating channel flows using a localized dynamic model," *Phys. Fluids*, vol. 7 (4), pp. 839–848, 1995.

[34] M. M. Molla, M. C. Paul, and G. Roditi, "LES of additive and non-additive pulsatile flows in a model arterial stenosis," *Comput. Meth. Biomech. Biomed. Eng.*, vol. 13 (1), pp. 105–120, 2010.

[35] M. M. Molla, M. C. Paul, and G. Roditi, "Physiological flow in a model of arterial stenosis," *J. Biomech.*, vol. 41 (S1), p. 243, 2008.

[36] T. J. Barber and A. Simmons, "Large-eddy simulation of a stenosed artery," *Australian and New Zealand Industrial and Applied Mathematics Journal*, vol. 51, pp. 186–200, 2010.

[37] R. Gardhagen, J. Lantz, F. Carlsson, and W. Karlsson, "Quantifying turbulent wall shear stress in a stenosed pipe using large eddy simulation," *ASME J. Biomech. Eng.*, vol. 132 (6), pp. 1–7, 2010.

[38] F. P. Tan, N. B. Wood, G. Tabor, and X. Y. Xu, "Comparison of LES of steady transitional flow in an idealized stenosed axisymmetric artery model with a RANS transitional model," *ASME J. Biomech. Eng.*, vol. 133 (5), pp. 1–12, 2011.

[39] R. S. Rogallo and P. Moin, "Numerical simulation of turbulent flows," *Annu. Rev. Fluid Mech.*, vol. 16, pp. 99–137, 1984.

[40] J. Smagorinsky, "General circulation experiments with the primitive equations, i. the basic experiment," *Mon. Weath. Rev.*, vol. 91, pp. 99–164, 1963.

[41] M. Germano, U. Piomelli, P. Moin, and W. H. Cabot, "A dynamic subgrid-scale eddy viscosity model," *Phys. Fluids A*, vol. 3 (7), pp. 1760–1765, 1991.

[42] M. V. Salvetti and S. Banerjee, "A priori tests of a new dynamic subgrid-scale model for finite-difference large-eddy simulations," *Phys. Fluids*, vol. 7 (11), pp. 2831–2847, 1995.

[43] M. M. Cross, "Rheology of non-Newtonian fluids: A new flow equation for pseudoplastic systems," *J. Coll. Sci.*, vol. 20 (5), pp. 417–437, 1965.

[44] Y. C. Fung, Biomechanics: Circulation. *2nd edition*, Springer, 1997.

[45] A. Leonard, "Energy cascade in large-eddy simulations of turbulent fluid flows," *Adv. Geophys.*, vol. 18, pp. 237–248, 1974.

[46] S. Ghosal and P. Moin, "The basic equations for the large-eddy simulation of turbulent flows in complex geometry," *J. Comp. Phys.*, vol. 118, pp. 24–37, 1995.

[47] P. Moin, K. Squires, W. Cabot, and s. Lee, "A dynamic subgrid-scale model for compressible turbulence and scalar transport," *Phys. Fluids A*, vol. 3, pp. 2746–2757, 1991.

[48] Y. Zang, R. L. Street, and J. R. Koseff, "A dynamic mixed subgrid-scale model and its application to turbulent recirculating flows," *Phys. Fluids A*, vol. 5 (12), pp. 3186–3196, 1993.

[49] U. Piomelli, "High Reynolds number calculations using the dynamic subgrid-scale stress model," *Phys. Fluids A*, vol. 5 (6), pp. 1484–1490, 1993.

[50] B.-C. Wang, E. Yee, and D. J. Bergstrom, "Geometrical description f the subgrid-scale stress tensor based on Euler axis/angle," *AIAA J.*, vol. 44 (5), pp. 1106–1110, 2006.

[51] C. G. Speziale, "On nonlinear k-l and k-ϵ models of turbulence," *J. Fluid Mech.*, vol. 178, pp. 459–475, 1987.

[52] T. B. Gatski and C. G. Speziale, "On explicit algebraic stress models for complex turbulent flows," *J. Fluid Mech.*, vol. 254, pp. 59–78, 1993.

[53] B.-C. Wang, E. Yee, D. J. Bergstrom, and O. Iida, "New dynamic subgrid-scale heat flux models for large-eddy simulation of thermal convection based on the general gradient diffusion hyposthesis," *J. Fluid Mech.*, vol. 604, pp. 125–163, 2008.

[54] B.-C. Wang, J. Yin, E. Yee, and D. J. Bergstrom, "A complete and irreducible dynamic SGS heat-flux modelling based on the strain rate tensor for large-eddy simulation of thermal convection," *Int. J. Heat Fluid Flow*, vol. 28 (6), pp. 1227–1243, 2007.

[55] Q.-Q. Xun, B.-C. Wang, and E. Yee, "Large-eddy simulation of turbulent heat convection in a spanwise rotating channel flow," *Int. J. Heat Mass Trans.*, vol. 54, pp. 698–716, 2011.

[56] B.-C. Wang, D. J. Bergstrom, J. Yin, and E. Yee, "Turbulence topologies predicted using large eddy simulations," *J. Turbul.*, vol. 7 (34), pp. 1–28, 2006.

[57] Y. Morinishi, T. S. Lund, O. V. Vasilyev, and P. Moin, "Fully conservative higher order finite difference schemes for incompressible flow," *J. Comp. Phys.*, vol. 143 (1), pp. 90–124, 1998.

[58] D. S. Kershaw, "The incomplete Cholesky-Conjugate gradient method for the iterative solution of systems," *J. Comp. Phys.*, vol. 26 (1), pp. 43–65, 1978.

[59] C. M. Rhie and W. L. Chow, "Numerical study of the turbulent flow past an airfoil with trailing edge separation," *AIAA J.*, vol. 21 (11), pp. 1525–1532, 1983.

[60] J. R. Womersley, "Method for the calculation of velocity, rate of flow and viscous drag in arteries when the pressure gradient is known," *J. Physiol.*, vol. 155, pp. 553–563, 1955.

[61] A. K. M. F. Hussain and W. C. Reynolds, "The mechanics of an organized wave in turbulent shear flow," *J. Fluid Mech.*, vol. 41 (2), pp. 241–258, 1970.

[62] S. Ghosal, T. S. Lund, P. Moin, and K. Akselvoll, "A dynamic localization model

for large-eddy simulation of turbulent flows," *J. Fluid Mech.*, vol. 286, pp. 229–255, 1995.

[63] D. Carati, S. Ghosal, and P. Moin, "On the representation of backscatter in dynamic localization models," *Phys. Fluids*, vol. 7 (3), pp. 606–616, 1995.

[64] J. Yin, B.-C. Wang, and D. J. Bergstrom, "Large-eddy simulation of combined forced and natural convection in a vertical plane channel," *Int. J. Heat Mass Trans.*, vol. 50 (19-20), pp. 3848–3861, 2007.

[65] P. C. Lu, D. R. Gross, and H. C. Hwang, "Intravascular pressure and velocity fluctuations in pulmonic arterial stenosis," *J. Biomech.*, vol. 13 (3), pp. 291–300, 1980.

[66] S. A. Berger and L. D. Jou, "Flows in stenotic vessels," *Annu. Rev. Fluid Mech.*, vol. 32, pp. 347–382, 2000.

[67] M. M. Molla, A. Hossain, B.-C. Wang, and D. C. S. Kuhn, "Large-eddy simulation of pulsatile non-Newtonian flow in a constricted channel," *Prog. in Comput Fluid Dyn.*, vol. 12 (4), pp. 231–242, 2012.

[68] R. S. Rivlin, "The relation between the flow of non-Newtonian fluids and turbulent newtonian fluids," *Quart. Appl. Math.*, vol. 15, pp. 212–215, 1957.

[69] A. J. M. Spencer, Part III: Theory of invariants. in *Continuum Physics, Volume I—Mathematics*, edited by A. C. Eringen, New York: Academic, 1971.

[70] J. F. Thomson, F. C. Thames, and C. W. Mastin, "Automatic numerical generation of body-fitted curvilinear coordinates system for field containing any number of arbitrary two dimensional bodies," *J. Comp. Phys.*, vol. 15 (3), pp. 299–319, 1974.

[71] S. V. Patankar, Numerical Heat Transfer and Fluid Flow. Hemisphere Publishing Corporation, 1980.

[72] C. Loudon and A. Tordesillas, "The use of the dimensionless Womersley number to characterize the unsteady nature of internal flow," *J. Theor. Biol.*, vol. 191 (1), pp. 63–78, 1998.

Appendix A

Numerical Procedure

The 3D LES code employed for conducting current simulations uses a finite volume approach where the filtered governing equations are integrated over control volumes and solved using computational methods. The numerical algorithm is described briefly in this Appendix.

A.1 Coordinate Transformation

Thompson *et al.* [70] introduced an approach where the partial differential equations are formulated in a transformed curvilinear coordinate system that coincides with the boundaries of the flow domain. In this approach, the flow domain in physical space is mapped onto a rectangular domain in computational space, as shown in Fig. A.1, where a two-dimensional case is represented for simplicity. For mapping $x_j \longrightarrow \xi_j$, if J_{ij} represents the elements of the Jacobian matrix, $\mathbf{J}$, of the transformation then

$$J_{ij} = \frac{\partial x_i}{\partial \xi_j} \tag{A.1}$$

The determinant of the Jacobian matrix, $\mathbf{J}$, is denoted by $|\mathbf{J}|$ and given by

$$|\mathbf{J}| = \frac{\partial x_i}{\partial \xi_j} A_{ij} \tag{A.2}$$

where A_{ij} are the elements of the cofactor matrix, $\mathbf{A}$, of the Jacobian, defined as

$$|\mathbf{A}| = |\mathbf{J}|\mathbf{J}^{-1} \tag{A.3}$$

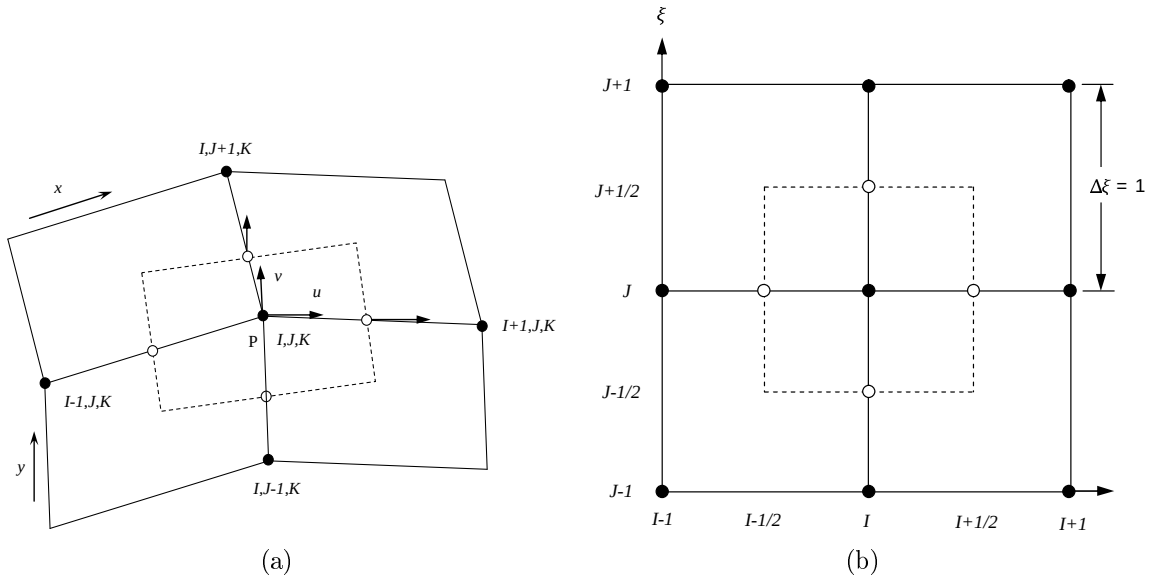

(a) (b)

FIGURE A.1: Grid arrangement and notation in two-dimensional case in both physical space (left) and computational space (right); solid lines for the grid lines and dashed lines for the faces of the control volume.

By applying the chain rule, the derivatives can now be expressed in the transformed space in the following way

$$\frac{\partial \phi}{\partial x_i} = \frac{\partial \phi}{\partial \xi_j}\frac{\partial \xi_j}{\partial x_i} = \frac{A_{ij}}{|\mathbf{J}|}\frac{\partial \phi}{\partial \xi_j} \tag{A.4}$$

where ϕ is a generic variable. The filtered governing Eqs. 2.14 and 2.15 in general curvilinear coordinates can be written as

$$\frac{\partial}{\partial \xi_k}\left(\frac{A_{kj}}{|\mathbf{J}|}\bar{u}_j\right) = 0 \tag{A.5}$$

$$\frac{\partial(\rho\bar{u}_i)}{\partial t} + \frac{\partial}{\partial \xi_k}\left(\frac{A_{kj}}{|\mathbf{J}|}\rho\bar{u}_i\bar{u}_j\right) = -\frac{A_{kj}}{|\mathbf{J}|}\frac{\partial \bar{p}}{\partial \xi_k} + \frac{\partial}{\partial \xi_k}\left[\frac{A_{kj}}{|\mathbf{J}|}\left(\mu_e\frac{A_{lj}}{|\mathbf{J}|}\frac{\partial \bar{u}_i}{\partial \xi_l} + \mu_e\frac{A_{li}}{|\mathbf{J}|}\frac{\partial \bar{u}_j}{\partial \xi_l}\right)\right] \tag{A.6}$$

where the effective viscosity, μ_e, is the sum of the molecular and SGS viscosity defined as

$$\mu_e = \mu + \mu_{sgs} \tag{A.7}$$

The finite volume method uses the integral form of the transport equations as the starting point. Integrating the transformed equations over a single control volume, ΔV, gives, the continuity:

$$\int_{\Delta S} G_k n_k ds = 0 \tag{A.8}$$

and momentum balance:

$$\begin{aligned}\int_{\Delta V} \frac{\partial(\rho \bar{u}_i)}{\partial t} |\mathbf{J}| dV + \int_{\Delta S} G_k \bar{u}_i n_k dS = &- \int_{\Delta V} A_{kj} \frac{\partial \bar{p}}{\partial \xi_k} dV \\ &+ \int_{\Delta S} \left[\mu_e \left(\frac{A_{lj} A_{kj}}{|\mathbf{J}|} \frac{\partial \bar{u}_i}{\partial \xi_l} + \frac{A_{li} A_{kj}}{|\mathbf{J}|} \frac{\partial \bar{u}_j}{\partial \xi_l} \right) \right] n_k dS\end{aligned} \tag{A.9}$$

where $G_k = A_{ij} \rho \bar{u}_j$, is the mass flux in the ξ_k coordinate direction, n_k is the unit normal pointing outward of the cell surface ΔS and the cell volume ΔV.

A.2 Discretisation Scheme

The grid arrangement is shown in Fig. A.1, where the mesh spacing in the transformed space is uniform, i.e., $\Delta \xi = 1$. The control volume (CV) faces lie midway between nodes. According to the collocated arrangement, all the variables, e.g. velocity and pressure stored at the CV centres are assumed to be uniform over the CV. A linear variation of variable values between grid nodes is assumed in such a way that the value of the variables at the cell faces are obtained as averages of the values at the appropriate adjacent nodes. In order to illustrate the discretisation scheme adopted, let us consider the u-momentum equation. The convective term is approximated by

$$\begin{aligned}\int_{\Delta S} G_k \bar{u} n_k ds \approx &[G_1 \bar{u}]_{I+\frac{1}{2},J,K} - [G_1 \bar{u}]_{I-\frac{1}{2},J,K} + [G_2 \bar{u}]_{I,J+\frac{1}{2},K} \\ &- [G_2 \bar{u}]_{I,J-\frac{1}{2},K} + [G_3 \bar{u}]_{I,J,K+\frac{1}{2}} - [G_3 \bar{u}]_{I,J,K-\frac{1}{2}}\end{aligned} \tag{A.10}$$

To demonstrate, let us use the first term of the Eq. A.10. $[G_1 \bar{u}]_{I+\frac{1}{2},J,K}$ is approximated as follows

$$[G_1 \bar{u}]_{I+\frac{1}{2},J,K} = \frac{1}{2} [G_1]_{I+\frac{1}{2},J,K} ([\bar{u}]_{I,J,K} + [\bar{u}]_{I+1,J,K}) \tag{A.11}$$

The variation of variables between nodal points is assumed to be linear. The

mass fluxes are then expressed as

$$[G_1]_{I+\frac{1}{2},J,K} = \rho \times \left([A_{11}\bar{u}]_{I+\frac{1}{2},J,K} + [A_{12}\bar{v}]_{I+\frac{1}{2},J,K} + [A_{13}\bar{w}]_{I+\frac{1}{2},J,K} \right) \tag{A.12}$$

where terms like $[A_{11}\bar{u}]_{I+\frac{1}{2},J,K}$ can be discretised as

$$\begin{aligned}[A_{11}\bar{u}]_{I+\frac{1}{2},J,K} = \frac{1}{2}([\bar{u}]_{I,J,K} + [\bar{u}]_{I+1,J,K})\times \\ \left(\left[\frac{\partial y}{\partial \eta}\right]_{I+\frac{1}{2},J,K} \cdot \left[\frac{\partial z}{\partial \zeta}\right]_{I+\frac{1}{2},J,K} - \left[\frac{\partial y}{\partial \zeta}\right]_{I+\frac{1}{2},J,K} \cdot \left[\frac{\partial w}{\partial \eta}\right]_{I+\frac{1}{2},J,K} \right)\end{aligned} \tag{A.13}$$

with

$$\left[\frac{\partial y}{\partial \eta}\right]_{I+\frac{1}{2},J,K} = \frac{1}{2}\left(\frac{[y]_{I,J+1,K} - [y]_{I,J-1,K}}{2} + \frac{[y]_{I+1,J+1,K} - [y]_{I+1,J-1,K}}{2} \right) \tag{A.14}$$

The diffusive terms are approximated in a similar manner. The cross derivative terms arising from the non-orthogonality of the transformed coordinate system are treated explicitly. Time derivatives are discretised using a three point backward difference scheme with a constant time step of δt, which is represented by

$$\frac{\partial \bar{u}}{\partial t} \approx \frac{3}{2}\left(\frac{\bar{u}^{n+1} - \bar{u}^{n}}{\delta t} \right) - \frac{1}{2}\left(\frac{\bar{u}^{n} - \bar{u}^{n-1}}{\delta t} \right) \tag{A.15}$$

where n is the number of time step. The discretisation scheme described above leads to a quasi-linear system of equations for the velocity, $\bar{u}$, which can be written as

$$a_{I,J,K}\bar{u}^{n+1}_{I,J,K} = \sum_{neighbours} a_\alpha \bar{u}^{n+1}_{\alpha} + S_{I,J,K} \tag{A.16}$$

where $S_{I,J,K}$ represents a source term containing all terms that can not be expressed as face fluxes but can be dependent on $\bar{u}$; and a_α represents the coefficients for both the convective and diffusive terms. The summation being taken over the immediate neighbours of I, J, K (i.e., $I \pm 1, J \pm 1, K \pm 1$).

A.3 Velocity and Pressure Calculation

Once the governing equations are discretised, the pressure and velocity fields are obtained by employing a pressure correction method which is similar to the SIMPLE algorithm of Patankar [71]. This method can be illustrated as follows. The governing equations, for instance, the u-momentum equation to within a second-order accuracy can be written in the following quasi-matrix form assuming a constant time step

$$\mathbf{u}^{n+1} - \mathbf{u}^{n} + \frac{2}{3}\delta t \mathbf{T}^{n+1}\mathbf{u}^{n+1} = -\frac{2}{3}\delta t \mathbf{D}\mathbf{p}^{n+1} + \mathbf{S} \tag{A.17}$$

where $\mathbf{u}$ is the vector of the unknown nodal values, $\mathbf{T}^{n+1}$ represents the coefficient matrix for the convection and diffusion terms at time level $n+1$, $\mathbf{D}$ arises from the discretisation of the pressure term, and the source term $\mathbf{S}$ contains all the terms resulting from the time discretisation. The derivative of diffusion terms are given explicit treatment in order to reduce the computational cost. Evaluating these derivatives at time level n and adding them to $\mathbf{S}$ introduces an error of $O(\delta t^2)$ into Eq. A.17. Therefore, Eq. A.17 can be written as

$$\mathbf{u}^{n+1} + \frac{2}{3}\delta t \mathbf{T}^{n}\mathbf{u}^{n+1} = -\frac{2}{3}\delta t \mathbf{D}\mathbf{p}^{n+1} + \mathbf{S} + O(\delta t^2) \tag{A.18}$$

where $\mathbf{S}$ now contains additionally those cross-derivative terms which are not included in $\mathbf{T}^{n}$ and treated explicitly. The bar in velocity is disregarded in order to simplify the notation.

The solution to Eq. A.18 obtained by neglecting the error term $O(\delta t^2)$ is a second order accurate approximation to $\mathbf{u}^{n+1}$. In order to achieve second order accuracy, Eq. A.17 is solved in two stages. In the first stage, a solution to Eq. A.18 is sought. Denoting this solution as $\mathbf{u}^{m}$, having a corresponding pressure field $\mathbf{p}^{m}$, and introducing a pressure increment, $\Delta\mathbf{p}^{m} = \mathbf{p}^{m} - \mathbf{p}^{n}$, Eq. A.18 becomes

$$\mathbf{u}^{m} + \frac{2}{3}\delta t \mathbf{T}^{n}\mathbf{u}^{m} + \frac{2}{3}\delta t \mathbf{D}\delta\mathbf{p}^{m} = -\delta t \mathbf{D}\mathbf{p}^{n} + \mathbf{S} \tag{A.19}$$

where m represents an intermediate time level between $n+1$, at which the solution is sought, and n, the most recent update. Applying an approximate factorisation,

Eq. A.19 can be recast as

$$\left(\mathbf{I}+\frac{2}{3}\delta t\mathbf{T}^n\right)\underbrace{\left(\mathbf{u}^m+\frac{2}{3}\delta t\mathbf{D}\Delta\mathbf{p}^m\right)}_{u^*}=-\frac{2}{3}\delta t\mathbf{D}\mathbf{p}^n+\mathbf{S} \tag{A.20}$$

A Taylor series analysis gives, $\mathbf{D}\Delta\mathbf{p}^m \approx O(\delta t)$. So, the error introduced by the approximate factorisation is $(\delta t)^2\mathbf{T}^n\mathbf{D}\Delta\mathbf{p}^m \approx O(\delta t)^3$ and can be neglected. Equation A.20 is then solved in two steps:

$$u^*=\left(\mathbf{I}+\frac{2}{3}\delta t\mathbf{T}^n\right)^{-1}\left(-\frac{2}{3}\delta t\mathbf{D}\mathbf{p}^n+\mathbf{S}\right) \tag{A.21}$$

$$u^m=u^*-\frac{2}{3}\delta t\mathbf{D}\delta\mathbf{p}^m \tag{A.22}$$

The vectors of unknown v and w nodal values, $\mathbf{v}$ and $\mathbf{w}$, are obtained in the similar way. However, none of these velocity fields at time level m can be obtained since Δp^m is still not known. In order to obtain the pressure increment, Δp^m, the velocity fields $\mathbf{u}^m$, $\mathbf{v}^m$ and $\mathbf{w}^m$ are substituted into the continuity equation, which gives a Poisson-type equation for the pressure increment, and this will be discussed in the following subsection. Since $\mathbf{u}^m$ is a second-order accurate approximation to $\mathbf{u}^{n+1}$, in the second stage, a second order accurate solution at time level $n+1$ is obtained by rewriting Eq. A.19 for the time level $n+1$, with the coefficient matrix evaluated using values from the intermediate time level m

$$\mathbf{u}^{n+1}+\frac{2}{3}\delta t\mathbf{T}^m\mathbf{u}^{n+1}+\frac{2}{3}\delta t\mathbf{D}\Delta\mathbf{p}^{n+1}=-\frac{2}{3}\delta t\mathbf{D}\mathbf{p}^m+\mathbf{S} \tag{A.23}$$

where the pressure increment, $\Delta\mathbf{p}^{n+1}=\mathbf{p}^{n+1}-\mathbf{p}^m$, is introduced. Using the approximate factorisation, Eq. A.23 can be written as

$$\left(\mathbf{I}+\frac{2}{3}\delta t\mathbf{T}^m\right)\underbrace{\left(\mathbf{u}^{n+1}+\frac{2}{3}\delta t\mathbf{D}\Delta\mathbf{p}^{n+1}\right)}_{u^{**}}=-\frac{2}{3}\delta t\mathbf{D}\mathbf{p}^m+\mathbf{S} \tag{A.24}$$

$$u^{**}=\left(\mathbf{I}+\frac{2}{3}\delta t\mathbf{T}^m\right)^{-1}\left(-\frac{2}{3}\delta t\mathbf{D}\mathbf{p}^m+\mathbf{S}\right) \tag{A.25}$$

$$u^{n+1}=u^{**}-\frac{2}{3}\delta t\mathbf{D}\Delta\mathbf{p}^{n+1} \tag{A.26}$$

The pressure increment is again computed from the Poisson-type equation which will be discussed in the next section.

A.4 Pressure Smoothing

The Poisson-type equation for the pressure increment can be defined as $\Delta p^m = p^m - p^{m-1}$, where m and $m-1$ indicate the values at the intermediate and most recent time levels, respectively. These values can be obtained by substituting Eq. A.21 into the continuity equation. For the illustration purpose, considering only the flux component arisen from the integration over the cell faces in the ξ direction, this substitution gives

$$\begin{aligned} &\frac{2\delta t}{3}\left[\frac{A_{1j}A_{kj}}{|\mathbf{J}|}\frac{\partial \Delta p^m}{\partial \xi_k}\right]_{I+\frac{1}{2},J,K} - \frac{2\delta t}{3}\left[\frac{A_{1j}A_{kj}}{|\mathbf{J}|}\frac{\partial \Delta p^m}{\partial \xi_k}\right]_{I-\frac{1}{2},J,K} \\ &\quad = [\rho A_{1j} u_j^{m-1}]_{I+\frac{1}{2},J,K} - [\rho A_{1j} u_j^{m-1}]_{I-\frac{1}{2},J,K} \end{aligned} \tag{A.27}$$

where u_j^{m-1} is the velocity field corresponding to pressure field p^{m-1}. Using the central difference interpolation between cell faces, for instance, the pressure increment gradient at $I+\frac{1}{2}, J, K$ is approximated by

$$\left[\frac{A_{kj}}{|\mathbf{J}|}\frac{\partial \Delta p^m}{\partial \xi_k}\right]_{I+\frac{1}{2},J,K} = \frac{1}{2}\left[\frac{A_{kj}}{|\mathbf{J}|}\right]_{I+\frac{1}{2},J,K}\left(\left[\frac{\partial \Delta p^m}{\partial \xi_k}\right]_{I+1,J,K} + \left[\frac{\partial \Delta p^m}{\partial \xi_k}\right]_{I,J,K}\right) \tag{A.28}$$

where

$$\begin{aligned} \left[\frac{A_{kj}}{|\mathbf{J}|}\right]_{I+\frac{1}{2},J,K}\left[\frac{\partial \Delta p^m}{\partial \xi_k}\right]_{I,J,K} &= \left[\frac{A_{1j}}{|\mathbf{J}|}\right]_{I+\frac{1}{2},J,K}\left(\frac{\Delta p^m_{I+1,J,K} - \Delta p^m_{I-1,J,K}}{2}\right) \\ &+ \left[\frac{A_{2j}}{|\mathbf{J}|}\right]_{I+\frac{1}{2},J,K}\left(\frac{\Delta p^m_{I,J+1,K} - \Delta p^m_{I,J-1,K}}{2}\right) \\ &+ \left[\frac{A_{3j}}{|\mathbf{J}|}\right]_{I+\frac{1}{2},J,K}\left(\frac{\Delta p^m_{I,J,K+1} - \Delta p^m_{I,J,K-1}}{2}\right) \end{aligned} \tag{A.29}$$

The above interpolations lead to an oscillatory pressure field which is decoupled from the velocity field at even and odd grid nodes. As a solution of this problem, the finite difference operators are redefined so that pressure increment derivatives normal to the cell faces are evaluated using values at nodes adjacent to the cell faces, and the cross derivatives are interpolated from gradients calculated at adjacent nodes. Hence,

$$\begin{aligned}\left[\frac{A_{kj}}{|\mathbf{J}|}\frac{\partial\Delta p^m}{\partial\xi_k}\right]_{I+\frac{1}{2},J,K,1\Delta} &= \left[\frac{A_{1j}}{|\mathbf{J}|}\right]_{I+\frac{1}{2},J,K}\left(\Delta p^m_{I+1,J,K}-\Delta p^m_{I,J,K}\right)\\ &+\left[\frac{A_{2j}}{|\mathbf{J}|}\right]_{I+\frac{1}{2},J,K}\left(\frac{\Delta p^m_{I+1,J+1,K}-\Delta p^m_{I-1,J-1,K}+\Delta p^m_{I,J+1,K}-\Delta p^m_{I,J-1,K}}{4}\right)\\ &+\left[\frac{A_{3j}}{|\mathbf{J}|}\right]_{I+\frac{1}{2},J,K}\left(\frac{\Delta p^m_{I+1,J,K+1}-\Delta p^m_{I-1,J,K-1}+\Delta p^m_{I,J,K+1}-\Delta p^m_{I,J,K-1}}{4}\right)\end{aligned} \tag{A.30}$$

where the subscript 1Δ denotes the compact stencil. It can be demonstrated that this approach is equivalent to adding a smoothing term, $\sigma(\Delta p^m)$, to the right hand side of Eq. A.27, of the form

$$\begin{aligned}\sigma(\Delta p^m) = &\frac{2\delta t}{3}\left[\frac{A_{1j}A_{kj}}{|\mathbf{J}|}\frac{\partial\Delta p^m}{\partial\xi_k}\right]_{I+\frac{1}{2},J,K,1\Delta}-\frac{2\delta t}{3}\left[\frac{A_{1j}A_{kj}}{|\mathbf{J}|}\frac{\partial\Delta p^m}{\partial\xi_k}\right]_{I+\frac{1}{2},J,K,1\Delta}\\ &+\frac{2\delta t}{3}\left[\frac{A_{1j}A_{kj}}{|\mathbf{J}|}\frac{\partial\Delta p^m}{\partial\xi_k}\right]_{I-\frac{1}{2},J,K,1\Delta}-\frac{2\delta t}{3}\left[\frac{A_{1j}A_{kj}}{|\mathbf{J}|}\frac{\partial\Delta p^m}{\partial\xi_k}\right]_{I-\frac{1}{2},J,K,1\Delta}\end{aligned} \tag{A.31}$$

This smoothing term involves known and unknown components, and can be written as

$$\sigma(\Delta p^m) = \sigma(p^m) - \sigma(p^{m-1}) \tag{A.32}$$

The Rhie and Chow [59] approach allows to add the unknown term, $\sigma(p^m)$, to the right hand side of the Eq. A.27. Adding this unknown term, the pressure increment equation becomes

$$\begin{aligned}&\frac{2\delta t}{3}\left[\frac{A_{1j}A_{kj}}{|\mathbf{J}|}\frac{\partial\Delta p^m}{\partial\xi_k}\right]_{I+\frac{1}{2},J,K,1\Delta}-\frac{2\delta t}{3}\left[\frac{A_{1j}A_{kj}}{|\mathbf{J}|}\frac{\partial\Delta p^m}{\partial\xi_k}\right]_{I-\frac{1}{2},J,K,1\Delta}\\ &\quad=\left[\rho A_{1j}u_j^{m-1}\right]_{I+\frac{1}{2},J,K}-\left[\rho A_{1j}u_j^{m-1}\right]_{I-\frac{1}{2},J,K}\\ &\quad+\frac{2\delta t}{3}\left[\frac{A_{1j}A_{kj}}{|\mathbf{J}|}\frac{\partial p^m}{\partial\xi_k}\right]_{I+\frac{1}{2},J,K}-\frac{2\delta t}{3}\left[\frac{A_{1j}A_{kj}}{|\mathbf{J}|}\frac{\partial p^m}{\partial\xi_k}\right]_{I+\frac{1}{2},J,K,1\Delta}\\ &\quad+\frac{2\delta t}{3}\left[\frac{A_{1j}A_{kj}}{|\mathbf{J}|}\frac{\partial p^m}{\partial\xi_k}\right]_{I-\frac{1}{2},J,K}-\frac{2\delta t}{3}\left[\frac{A_{1j}A_{kj}}{|\mathbf{J}|}\frac{\partial p^m}{\partial\xi_k}\right]_{I-\frac{1}{2},J,K,1\Delta}\end{aligned} \tag{A.33}$$

The mass flux, for instance, at $I+\frac{1}{2}, J, K$, is then updated from

$$[\rho A_{1j} u_j^m]_{I+\frac{1}{2},J,K} = [\rho A_{1j} u_j^{m-1}]_{I+\frac{1}{2},J,K} + \frac{2\delta t}{3}\left[\frac{A_{1j}A_{kj}}{|\mathbf{J}|}\frac{\partial p^{m-1}}{\partial \xi_k}\right]_{I+\frac{1}{2},J,K} - \frac{2\delta t}{3}\left[\frac{A_{1j}A_{kj}}{|\mathbf{J}|}\frac{\partial p^{m-1}}{\partial \xi_k}\right]_{I+\frac{1}{2},J,K,1\Delta} + \frac{2\delta t}{3}\left[\frac{A_{1j}A_{kj}}{|\mathbf{J}|}\frac{\partial \Delta p^{m}}{\partial \xi_k}\right]_{I-\frac{1}{2},J,K,1\Delta} \tag{A.34}$$

and the velocity field stored at the cell centres is updated from the original discrete approximation, such that

$$[u_j^m]_{I,J,K} = [u_j^{m-1}]_{I,J,K} - \frac{2\delta t}{3}\left[\frac{A_{kj}}{|\mathbf{J}|}\frac{\partial \Delta p^{m}}{\partial \xi_k}\right]_{I,J,K,} \tag{A.35}$$

A.5 Solution Algorithm and Convergent Condition

The system of algebraic equations resulting from the above discretisation are solved according to the following algorithm:

- Compute $\mathbf{u}^*$, $\mathbf{v}^*$ and $\mathbf{w}^*$ from Eq. A.21 using most recently updated $\mathbf{G}^n$ and $\mathbf{p}^n$.
  - Solve for $\Delta\mathbf{p}^m$ from Eq. A.33 with the nonlinear momentum interpolation method of Rhie and Chow [59].
  - Update mass fluxes and velocities using Eqs. A.34 and A.35, respectively, to obtain $\mathbf{G}^m$, $\mathbf{u}^m$, $\mathbf{v}^m$ and $\mathbf{w}^m$.
- Compute $\mathbf{u}^{**}$, $\mathbf{u}^{**}$ and $\mathbf{u}^{**}$ from Eq. A.25 using the updated $\mathbf{G}^m$ and $\mathbf{p}^m$.
  - Solve for Δp^{n+1} from Eq. A.33 with the nonlinear momentum interpolation method of Rhie and Chow [59].
  - Update mass fluxes and velocities using Eqs. A.34 and A.35, respectively, to obtain $\mathbf{G}^{n+1}$, $\mathbf{u}^{n+1}$, $\mathbf{v}^{n+1}$ and $\mathbf{w}^{n+1}$.

The maximum residuals, representing the errors associated with the entire solution procedure, are calculated within the solvers as a part of the solution

procedure. For velocity, the normalised residual is

$$||\mathbf{u}^{n+1}||^{\#} = \frac{t^{\#}(R^{u}_{ijk})_{max}}{[max(\rho^2 u^2_{ijk} + \rho^2 v^2_{ijk} + \rho^2 w^2_{ijk})]^{1/2}} \tag{A.36}$$

where the time scale $t^{\#}$ depends on the flow under investigation and is defined using a length and a velocity scale representative of conditions at the inlet; ijk represents the location in the computational domain. The normalised residual for the pressure increment is

$$||\Delta\mathbf{p}^{n+1}||^{\#} = \frac{t^{\#}(R^{p}_{ijk})_{max}}{\left(\frac{1}{N_{grid}} \sum_{N_{grid}} \rho^2\right)^{1/2}} \tag{A.37}$$

where N_{grid} is the total number of grid points. Here R^{u}_{ijk} and R^{p}_{ijk} are the dimensional residuals for the velocity and pressure respectively. The momentum equations are iterated until $||\mathbf{u}^{n+1}||^{\#} < 10^{-7}$. The tolerance for the pressure increment equation is reduced so that the iterative procedure does not terminate until $||\Delta\mathbf{p}^{n+1}||^{\#} < 10^{-8}$.

Appendix B

Generation of A Physiological Flow

The physiological pulsatile velocity profile is obtained from the solution of a one-dimensional Navier-Stokes equation where the pressure gradient is the Fourier series of time. Womersley [60] first calculated the physiological velocity profile for a tube by using the pressure gradient. A similar approach has been applied by Loudon and Tordesillas [72] to calculate the physiological pulsatile velocity profiles between the two parallel flat plates. This appendix documents the mathematical approach used for deriving the physiological pulsatile velocity profile at the inlet of the channel.

B.1 Steady Part of the Solution

Let us consider a one-dimensional fluid flow with density ρ and dynamic viscosity μ between two surfaces separated by a distance h. The governing equation of motion of the fluid is given by the following form of Navier-Stokes equation

$$\frac{\partial^2 \bar{u}}{\partial y^2} - \frac{\rho}{\mu}\frac{\partial \bar{u}}{\partial t} = \frac{1}{\mu}\frac{\partial \bar{p}}{\partial x}, \quad -\frac{h}{2} \leq y \leq \frac{h}{2} \tag{B.1}$$

where

$$\frac{\partial \bar{p}}{\partial x} = \frac{2}{3}A_0 \tag{B.2}$$

Here A_0 is the constant corresponding to the steady pressure gradient.

If the flow is in steady state,

$$\frac{\partial \bar{u}}{\partial t} = 0 \tag{B.3}$$

Now from Eq. B.1,

$$\frac{\partial^2 \bar{u}}{\partial y^2} = \frac{1}{\mu}\frac{\partial \bar{p}}{\partial x} \tag{B.4}$$

By integrating Eq. B.4, we obtain

$$\frac{\partial \bar{u}}{\partial y} = \frac{1}{\mu}\frac{\partial \bar{p}}{\partial x} y + C_1 \tag{B.5}$$

At y=0 , $\frac{\partial \bar{u}}{\partial y} = 0$, and therefore, $C_1 = 0$. This results in

$$\frac{\partial \bar{u}}{\partial y} = \frac{1}{\mu}\frac{\partial \bar{p}}{\partial x} y \tag{B.6}$$

By integrating Eq. B.6, we obtain

$$\bar{u} = \frac{1}{\mu}\frac{\partial \bar{p}}{\partial x}\frac{y^2}{2} + C_2 \tag{B.7}$$

At $\frac{h}{2} = 0, \bar{u} = 0$. Therefore, $C_2 = -\frac{1}{8\mu}\frac{\partial \bar{p}}{\partial x} h^2$,

$$\bar{u} = \frac{1}{\mu}\frac{\partial \bar{p}}{\partial x}\frac{y^2}{2} - \frac{1}{8\mu}\frac{\partial \bar{p}}{\partial x} h^2 = \frac{1}{\mu}\frac{2}{3} A_0 - \frac{1}{8\mu}\frac{\partial \bar{p}}{\partial x} h^2 \tag{B.8}$$

Now, the volume flow rate per unit length, Q/l is expressed as

$$\begin{aligned}
\frac{Q}{l} &= \frac{1}{2\mu}\frac{\partial \bar{p}}{\partial x}\int_{h/2}^{-h/2} (y^2 - h^2/4)\partial y \\
&= \frac{1}{2\mu}\frac{\partial \bar{p}}{\partial x}[\frac{y^3}{3} - \frac{y^2}{4} y]_{-h/2}^{h/2} \\
&= \frac{1}{2\mu}\frac{\partial \bar{p}}{\partial x}(\frac{h^3}{24} - \frac{h^3}{8} + \frac{h^3}{24} - \frac{h^3}{8}) \\
&= -\frac{1}{12\mu}\frac{\partial \bar{p}}{\partial x} h^3
\end{aligned} \tag{B.9}$$

The bulk velocity $\bar{U}$ is expressed as

$$\bar{u} = \frac{Q}{A} = \frac{-\frac{1}{12\mu}\frac{\partial \bar{p}}{\partial x} h^3 l}{hl} = -\frac{1}{12\mu}\frac{\partial \bar{p}}{\partial x} h^2 \tag{B.10}$$

From Eq. B.10, we obtain

$$\frac{\partial \bar{p}}{\partial x} = \frac{-12\mu \bar{U}}{h^2} \tag{B.11}$$

From Eqs. B.2, B.8 and B.11, the solution of the velocity field is obtained as

$$\bar{u}(y,t) = \bar{U}[1 - 4\frac{y^2}{h^2}] \tag{B.12}$$

B.2 Oscillatory Part of the Solution

For the oscillatory part,

$$\frac{\partial \bar{p}}{\partial x} = -Ae^{i(n\omega t + \phi_n)} \tag{B.13}$$

where A is the constant corresponding to the oscillatory pressure gradient. Let us assume that the solution of Eq. B.1 is

$$\bar{u} = v(y)e^{i(n\omega t + \phi_n)} \tag{B.14}$$

From Eqs. B.1 and B.14,

$$v'' - \frac{\rho}{\mu} in\omega v = 0 \tag{B.15}$$

For complementary function, let us assume

$$v'' - \frac{\rho}{\mu} in\omega v = 0 \tag{B.16}$$

Solving the auxiliary equation corresponding to Eq. B.16, $m = \pm\sqrt{\frac{\rho}{\mu} in\omega}$, the complementary function can be written as

$$v(y) = A_1 \cosh(\sqrt{\frac{\rho}{\mu} in\omega}.y) + iB_1 \sinh(\sqrt{\frac{\rho}{\mu} in\omega}.y) \tag{B.17}$$

For the particular integral, the corresponding equation can be written as

$$\begin{aligned}(D^2 - \frac{\rho}{\mu} in\omega)v(y)e^{i(n\omega t+\phi_n)} &= -\frac{1}{\mu}Ae^{i(n\omega t+\phi_n)} \\ \Longrightarrow v &= -\frac{A}{\mu}.\frac{1}{D^2 - \frac{\rho}{\mu}in\omega} \\ &= \frac{A}{\mu}(1 - \frac{D^2}{\frac{\rho}{\mu}in\omega})^{-1} \\ &= \frac{A}{\rho in\omega} \end{aligned} \tag{B.18}$$

Now combining the auxiliary equation and complementary function

$$v(y) = A_1 \cosh(\sqrt{\frac{\rho}{\mu}in\omega}.y) + iB_1 \sinh(\sqrt{\frac{\rho}{\mu}in\omega}.y) + \frac{A}{\rho in\omega} \tag{B.19}$$

The corresponding boundary conditions are: $\frac{\partial v}{\partial y} = 0$ at $y = 0$ and $v = 0$ at $y = \frac{h}{2}$. Applying these two boundary conditions into Eq. B.19, we get $B_1 = 0$ and $A_1 = -\frac{A}{in\omega \cosh(\sqrt{\frac{\rho}{\mu}in\omega}\frac{h}{2})}$. Based on these, the solution takes the following form

$$v(y) = \frac{A}{in\omega}[1 - \frac{\cosh(\sqrt{\frac{\rho}{\mu}in\omega}y)}{\cosh(\sqrt{\frac{\rho}{\mu}in\omega}\frac{h}{2})}] \tag{B.20}$$

Using the definition of Womersley number, $\alpha = h\sqrt{\frac{\omega\rho}{\mu}}$, we can write the final solution as

$$u(y,t) = \frac{Ah^2}{in\mu\alpha^2}[1 - \frac{\cosh(\sqrt{in}\alpha\frac{y}{h})}{\cosh(\sqrt{in}\alpha\frac{1}{2})}]e^{i(n\omega t+\phi_n)} \tag{B.21}$$

The real part of this solution is used to generate physiological velocity profile at the inlet of the channel.

B.3 Real Part of the Solution

In order to separate the real part of the solution from Eq. B.21, the De Moivres theorem of complex numbers is needed together with some trigonometric formulas. The De Moivres theorem gives

$$(\cos\theta + i\sin\theta)^m = [\cos(m\theta) + i\sin(m\theta)], \tag{B.22}$$

If $z = x + iy$, then

$$\cosh z = \cosh x \cos y + i \sinh x \sin y \tag{B.23}$$

Using the De Moivres theorem, we obtain

$$\begin{aligned} \sqrt{i} &= [\cos(\frac{\pi}{2}) + i \sin(\frac{\pi}{2})]^{\frac{1}{2}} \\ &= \frac{1}{\sqrt{2}}(1+i) \end{aligned} \tag{B.24}$$

$$\begin{aligned} \cosh(\sqrt{in}\alpha\frac{y}{h}) &= \cosh[\alpha\sqrt{n}\frac{1}{\sqrt{2}}(1+i)\frac{y}{h}] \\ &= \cosh(\alpha\sqrt{\frac{n}{2}}\frac{y}{h})\cos(\alpha\sqrt{\frac{n}{2}}\frac{y}{h}) \\ &+ i\sinh(\alpha\sqrt{\frac{n}{2}}\frac{y}{h})\sin(\alpha\sqrt{\frac{n}{2}}\frac{y}{h}) \\ &= \cosh\phi_1\cos\phi_1 + i\sinh\phi_1\sin\phi_1 \end{aligned} \tag{B.25}$$

$$\begin{aligned} \cosh(\sqrt{in}\alpha\frac{1}{2}) &= \cosh[\alpha\sqrt{n}\frac{1}{\sqrt{2}}(1+i)\frac{1}{2}] \\ &= \cosh(\sqrt{\frac{n}{2}}\frac{\alpha}{2})\cos(\sqrt{\frac{n}{2}}\frac{\alpha}{2}) \\ &+ i\sinh(\sqrt{\frac{n}{2}}\frac{\alpha}{2})\sin(\sqrt{\frac{n}{2}}\frac{\alpha}{2}) \\ &= \cosh\phi_2\cos\phi_2 + i\sinh\phi_2\sin\phi_2 \end{aligned} \tag{B.26}$$

and

$$e^{i(n\omega t+\phi_n)} = e^{iP} = \cos P + i \sin P \tag{B.27}$$

From Eqs. B.21, B.25 and B.26, we obtain

$$
\begin{aligned}
u(y,t) &= \frac{Ah^2}{in\mu\alpha^2}\left[1-\frac{\cosh(\sqrt{in}\alpha\frac{y}{h})}{\cosh(\sqrt{in}\alpha\frac{1}{2})}\right]e^{i(n\omega t+\phi_n)} \\
&= i\frac{Ah^2}{n\mu\alpha^2}\left[\frac{\cosh(\sqrt{in}\alpha\frac{y}{h})}{\cosh(\sqrt{in}\alpha\frac{1}{2})}-1\right](\cos P+i\sin P) \\
&= i\frac{Ah^2}{n\mu\alpha^2}\left[\frac{\cosh\phi_1\cos\phi_1+i\sinh\phi_1\sin\phi_1}{\cosh\phi_2\cos\phi_2+i\sinh\phi_2\sin\phi_2}-1\right](\cos P+i\sin P) \\
&= i\frac{Ah^2}{n\mu\alpha^2}\left[\frac{(\cosh\phi_1\cos\phi_1+i\sinh\phi_1\sin\phi_1)(\cosh\phi_2\cos\phi_2-i\sinh\phi_2\sin\phi_2)}{\cosh^2\phi_2\cos^2\phi_2+\sinh^2\phi_2\sin^2\phi_2}-1\right] \\
&(\cos P+i\sin P) \\
&= i\frac{Ah^2}{n\mu\alpha^2}[\frac{1}{D_r}(\cosh\phi_1\cos\phi_1\cosh\phi_2\cos\phi_2-i\cosh\phi_1\cos\phi_1\sinh\phi_2\sin\phi_2 \\
&+i\sinh\phi_1\sin\phi_1\cosh\phi_2\cos\phi_2+\sinh\phi_1\sin\phi_1\sinh\phi_2\sin\phi_2)-1](\cos P+i\sin P) \\
&= \frac{Ah^2}{n\mu\alpha^2 D_r}[(i\cosh\phi_1\cos\phi_1\cosh\phi_2\cos\phi_2+\cosh\phi_1\cos\phi_1\sinh\phi_2\sin\phi_2 \\
&-\sinh\phi_1\sin\phi_1\cosh\phi_2\cos\phi_2+i\sinh\phi_1\sin\phi_1\sinh\phi_2\sin\phi_2)-iD_r](\cos P+i\sin P) \\
&= \frac{Ah^2}{n\mu\alpha^2 D_r}[i\cosh\phi_1\cos\phi_1\cosh\phi_2\cos\phi_2\cos P+\cosh\phi_1\cos\phi_1\sinh\phi_2\sin\phi_2\cos P \\
&-\sinh\phi_1\sin\phi_1\cosh\phi_2\cos\phi_2\cos P+i\sinh\phi_1\sin\phi_1\sinh\phi_2\sin\phi_2\cos P-iD_r\cos P \\
&-\cosh\phi_1\cos\phi_1\cosh\phi_2\cos\phi_2\sin P+i\cosh\phi_1\cos\phi_1\sinh\phi_2\sin\phi_2\sin P \\
&-i\sinh\phi_1\sin\phi_1\cosh\phi_2\cos\phi_2\sin P \\
&-\sinh\phi_1\sin\phi_1\sinh\phi_2\sin\phi_2\sin P+D_r\sin P]
\end{aligned}
\tag{B.28}
$$

Now separating the real part from Eq. B.28, to obtain

$$
\begin{aligned}
u(y,t) &= \frac{Ah^2}{n\mu\alpha^2 D_r}[\cosh\phi_1\cos\phi_1\sinh\phi_2\sin\phi_2\cos P \\
&- \sinh\phi_1\sin\phi_1\cosh\phi_2\cos\phi_2\cos P \\
&- \cosh\phi_1\cos\phi_1\cosh\phi_2\cos\phi_2\sin P \\
&- \sinh\phi_1\sin\phi_1\sinh\phi_2\sin\phi_2\sin P+D_r\sin P]
\end{aligned}
\tag{B.29}
$$

where

$$\phi_1 = \alpha\sqrt{\frac{n}{2}}\frac{y}{h} \tag{B.30}$$

$$\phi_2 = \frac{\alpha}{2}\sqrt{\frac{n}{2}} \tag{B.31}$$

$$P = n\omega t + \phi_n \tag{B.32}$$

$$D_r = \cosh^2\phi_2\cos^2\phi_2 + \sinh^2\phi_2\sin^2\phi_2 \tag{B.33}$$

Thus, the full solution including the steady and oscillatory part for N harmoincs can be written as:

$$u(y,t) = \bar{U}[1 - 4\frac{y^2}{h^2}] + \sum_{n=1}^{N}\frac{M_n A h^2}{in\mu\alpha^2}[1 - \frac{\cosh(\sqrt{in}\alpha\frac{y}{h})}{\cosh(\sqrt{in}\alpha\frac{1}{2})}]e^{i(n\omega t+\phi_n)} \tag{B.34}$$